Metal Binding to Nsp1, a SARS-CoV-2 protein

Thesis by

Maryann Morales

In Partial Fulfillment of the Requirements for

the Degree of

Doctor of Philosophy

CALIFORNIA INSTITUTE OF TECHNOLOGY

Pasadena, California

2025

(Defended May 8, 2025)

Maryann Morales
ORCID: 0000-0002-1778-8901

ACKNOWLEDGEMENTS

To my family

"We are the sum of those who have supported us." -Unknown

My graduate studies would not have been possible without the unwavering support, guidance, and encouragement of many individuals. The following words cannot fully capture the depth of my gratitude, but they aim to reflect the immense appreciation I hold for everyone who helped me reach this milestone.

I would like to express my deepest gratitude to my family for their unwavering support throughout my journey. To my mom, Ana Beatriz Rios, and dad, Virgilio Morales Melendez, thank you for always emphasizing the importance of education and encouraging me to pursue my passions. I also want to thank my brother, Anthony Morales, for his continual support. My extended family has been a source of strength and encouragement during this time, and I am forever grateful for their love. Although my grandpa, Tito, is no longer with us, I know he would have been incredibly proud to see this moment.

I owe a special debt of gratitude to Professor Harry B. Gray for taking a chance on me. Being his "last student" has been an honor beyond words. His mentorship, sharp memory, even surpassing my own at times, and our afternoon conversations over whiskey will always remain cherished memories.

I attribute a lot of my growth as a scientist these past five years to Dr. Jay R. Winkler. Through him I developed invaluable critical thinking skills. He is an exceptional mentor and a fountain of knowledge like no other. His door was always open, whether for research advice or life guidance, and I am truly appreciative of him.

My path in science began with Ms. Lily Min, whose passion for chemistry during my high school years sparked my curiosity and set me on this course. Her dedication to her students left a lasting impact that I will always carry with me.

I am profoundly thankful to Professor Valentine I. Vullev for reshaping my career trajectory during my time at UC Riverside. His mentorship transformed a summer research opportunity into a defining moment that led me to pursue a PhD in Chemistry. I am equally grateful to

Katarzyna Rybicka-Jasińska, Eli Espinoza, James Derr, and John Clark for their mentorship and friendship, and support that extended far beyond my undergraduate years.

The collaborative work with Professor William A. Goddard III and his team played a pivotal role in the latter half of my PhD studies. I am especially thankful to Moon Young Yang for his contributions to computational modeling, as well as Joo-Youn Lee and Soo-Kyung Kim for their collaboration and support on computational projects.

Within the Gray group, I had the privilege of working alongside many talented individuals. I extend heartfelt thanks to Raheleh Ravanfar and Yuling Sheng for sharing their expertise in microbiology, and to Jill Clinton for her unwavering support—both in research and through the many memorable moments we shared outside the lab. I'll always cherish our evening sushi dinners, Knob Creek runs, and Del Taco adventures. Although my overlap with Alexandra Barth was brief, her mentorship helped me navigate my PhD journey. Alexandra Barth provided guidance that helped me navigate key phases of my PhD, and I am grateful to Jieun Shin, Javier Fajarado, and Ariane Helou for their encouragement and assistance.

I am also grateful for the visiting students who made my time at Caltech an enjoyable and enriching experience: Katarzyna Rybicka-Jasińska, Joanna Turkowska, Sejin Park, Jihwan Kim, YeongJun Son, and Yeongjun Yu.

Special thanks are due to Paul Oyala for his guidance with electron paramagnetic resonance experiments, David Vandervelde for his assistance with Cobalt-59 NMR, and Mona Shahgholi for her expertise in mass spectrometry.

I am appreciative of my committee members: Prof. Ryan Hadt, Prof. Doug Rees, Prof. Mitchio Okumura, and Dr. Scott Virgil, for their insights and contributions to my development as a scientist.

I would like to extend my gratitude to all the staff members at Caltech who make everything run smoothly behind the scenes. Thank you to Armando Villasenor and Gregory Rolette for always delivering my packages and for all our wonderful conversations. Thank you to Alfonso Godines, for keeping the sub-basement labs tidy. Thank you to Lucy Hammond and Jose Alcaraz at Broad

and Red Door, for always preparing my coffee or sandwich with a smile. Lastly, a heartfelt thanks to Patricia Estrada for keeping my office clean, ensuring my plants thrived even when I was a negligent plant mom, and for all the "chisme" and "platicas" we shared.

This accomplishment stands as a reflection of the collective support, mentorship, and generosity of everyone mentioned and many more.

ABSTRACT

The COVID-19 pandemic, caused by the severe acute respiratory syndrome coronavirus 2 (SARS-CoV-2), has led to unprecedented global health and socioeconomic challenges since its emergence in late 2019. Widespread vaccination efforts have lessened the severity of infections, however, the continuous evolution of the virus highlights the need for novel antiviral treatments. A critical aspect of SARS-CoV-2 pathogenesis is its ability to suppress host immune responses, allowing efficient viral replication and persistence. Among the 16 nonstructural proteins encoded by the viral ORF1ab polyprotein, nonstructural protein 1 (Nsp1) plays a pivotal role in immune evasion by inhibiting type I interferon (IFN-I) responses and shutting down host protein translation. Nsp1 achieves this by promoting host mRNA degradation, blocking nuclear export of transcripts, and binding to the 40S ribosomal subunit, where its intrinsically disordered C-terminal region adopts a helix–turn–helix structure that blocks the mRNA entry tunnel. Even at low micromolar concentrations, Nsp1 effectively halts host translation, making it a key virulence factor and an attractive antiviral drug target.

However, the lack of a stable folded structure within the C-terminal domain presents a significant challenge for conventional structure-based drug discovery. This work investigates an alternative strategy by leveraging the coordination chemistry of transition metals to target the disordered regions of Nsp1. Specifically, copper(II) and cobalt(III) complexes were explored for their ability to bind to histidine residues, particularly H165, which is essential for Nsp1's interaction with the ribosome.

A combination of biophysical techniques, including fluorescence spectroscopy, electron paramagnetic resonance (EPR), and ^{59}Co nuclear magnetic resonance (NMR), alongside computational modeling, was employed to characterize metal coordination to Nsp1-derived peptides and the full-length protein. Cu(II) was found to coordinate through both histidine side chains and backbone amide nitrogens within the disordered C-terminal region, exhibiting pH-dependent binding modes. Co(II) complexes, upon controlled oxidation to Co(III), formed substitution-inert complexes, effectively "locking" the metal ion in place and stabilizing interactions with Nsp1. These studies revealed multi-site binding behavior and provided insights into the kinetics of metal-protein interactions with Nsp1.

Additionally, *in vitro* translation assays demonstrated that while certain metal complexes could modulate translation processes, their ability to selectively inhibit Nsp1 function remains complex, highlighting both the potential and challenges of metal-based therapeutic approaches. This research establishes a foundation for targeting intrinsically disordered viral proteins using coordination chemistry, offering a novel perspective for antiviral drug development beyond traditional small molecule inhibitors. The insights gained from this work contribute to a deeper understanding of Nsp1's biochemical properties and open new avenues for combating SARS-CoV-2.

PUBLISHED CONTENT AND CONTRIBUTIONS

Contents of Chapter 3 include work from:

Morales, M.; Ravanfar, R.; Oyala, P. H.; Gray, H. B.; Winkler, J. R. Copper(II) Binding to the Intrinsically Disordered C-Terminal Peptide of SARS-CoV-2 Virulence Factor Nsp1. *Inorg Chem* **2022**, 61 (24), 8992–8996. https://doi.org/10.1021/acs.inorgchem.2c01329.

M.M. performed research, contributed new reagents/analytic tools, analyzed data, and co-wrote the paper.

Morales, M.; Yang, M. Y.; Goddard, W. A.; Gray, H. B.; Winkler, J. R. Copper(II) Coordination to the Intrinsically Disordered Region of SARS-CoV-2 Nsp1. *Proc Natl Acad Sci U.S.A.* **2024**, 121 (20), e2402653121. https://doi.org/10.1073/pnas.2402653121.

M.M. performed research, contributed new reagents/analytic tools, analyzed data, and co-wrote the paper.

TABLE OF CONTENTS

LIST OF FIGURES

LIST OF TABLES

Chapter 1

INTRODUCTION

COVID-19 Pandemic: A Global Challenge and Scientific Response

As of March 2025, COVID-19 has resulted in approximately 676 million cases and 6.8 million deaths worldwide.[1] The disease is caused by severe acute respiratory syndrome coronavirus 2 (SARS-CoV-2). While the peak of the pandemic has passed, the virus continues to circulate due to ongoing transmission and the emergence of mutations that enhance its ability to spread.[2] Although vaccines have been developed to prevent infection, understanding the virus remains essential for advancing therapeutic strategies and better preparing us for future pandemics.

In December 2019, several cases of pneumonia of unknown origin were reported in Wuhan, Hubei province, China. Most of these patients were linked to the Huanan Seafood Wholesale Market. SARS-CoV-2 was later identified as the causative agent of these pneumonia cases.[3,4] Phylogenetic analysis revealed a distinct lineage with Bat-SARS, confirming a zoonotic origin.[5,6] Bats are the second most numerous mammals after rodents and have been known as sources of coronaviruses and other zoonotic viruses.[7]

Initially, scientists believed the disease was transmitted solely from animals to humans and only between symptomatic individuals. However, cases in Germany revealed that human transmission could also occur from asymptomatic carriers.[8,9] By April 2020, the disease had spread to over 200 countries, with 1.4 million confirmed cases and more than 100,000 deaths. The pandemic prompted global authorities to impose travel restrictions, limit large gatherings, and advise people to stay home unless absolutely necessary.

Worldwide leadership began to institute control measures to try and keep the pandemic from spreading. Travel advisories and flight bans to and from infected countries were put into place. Quarantine measures were established and traveler screenings were added as part of travel measures. Healthcare specialist emphasized the importance of social distancing, hand washing and wearing face masks.[10]

From the onset of the COVID-19 pandemic, the world turned to scientists for solutions, and vaccination quickly emerged as the most effective and safe strategy to control the virus's spread.[11] To accelerate vaccine development, researchers leveraged preclinical data from SARS-CoV and MERS-CoV vaccine studies. [12–15] As a result, seven different types of COVID-19 vaccines were

developed. Inactivated vaccines involve culturing the virus *in vitro* and inactivating it with chemical agents, allowing the entire virus to act as an immunogen that induces a broad antibody response.[16,17] Live attenuated vaccines use a weakened form of the virus, obtained through reverse genetics or adaptation, which retains key amino acid sequences to generate a strong immune response, including mucosal immunity that protects the upper respiratory tract.[11] Viral vector vaccines utilize engineered, replication-attenuated viruses that carry genetic material of viral proteins, inducing a robust Th1 cell response, as seen in the Johnson & Johnson vaccine.[18,19] Protein subunit vaccines rely on cell expression systems to produce viral proteins or peptides that stimulate a targeted Th1 response.[20] DNA vaccines encode viral antigens within recombinant plasmids, triggering the production of neutralizing antibodies.[17] mRNA vaccines, such as the Pfizer-BioNTech and Moderna vaccines, encapsulate mRNA to instruct cells to produce viral proteins or peptides, stimulating a strong Th1 and B-cell response while promoting long-lived plasma and memory cells. [21,22] Finally, virus-like particle (VLP) vaccines are composed of non-infectious particles that contain viral structural proteins and polypeptides, which facilitate antigen loading and induce neutralizing antibodies against immune epitopes.[17]

In the United States, the FDA granted emergency use authorization for the Pfizer-BioNTech and Moderna mRNA vaccines in December 2020, followed by the Janssen/Johnson & Johnson viral vector vaccine in 2021. It was not until 2022 that the Moderna and Pfizer-BioNTech vaccines received full FDA approval. Widespread vaccination and other public health measures caused COVID-19 cases to decline, hospitalizations to decrease, and the world slowly began adjusting to a new normal, one reminiscent of life before the pandemic, yet undeniably changed.

The COVID-19 pandemic has had a profound impact on global health and daily life. The peak of the crisis has passed, however, the virus continues to evolve requiring continuous monitoring and research. The rapid development of vaccines played a crucial role in mitigating the severity of the disease and preventing further loss of life. However, the emergence of new variants highlights the importance of research into viral transmission, immunity, and treatments. As the world adapts to a post-pandemic reality, research and public health efforts remain essential to controlling outbreaks and preparing for future pandemics. The lessons learned from COVID-19 will serve as a foundation for more effective responses to emerging infectious diseases.

SARS-CoV-2 Taxonomy

Coronaviruses are a large group of viruses classified under the order *Nidovirales*, suborder *Cornidovirineae*, and family *Coronaviridae*. The *Coronaviridae* family is divided into two subfamilies: *Letovirinae* and *Orthocoronavirinae*. The latter is further categorized into four genera: *Alphacoronavirus, Betacoronavirus, Gammacoronavirus*, and *Deltacoronavirus*. The coronavirus responsible for the COVID-19 pandemic belongs to the *Betacoronavirus* genus and the *Sarbecovirus* subgenus. A taxonomy diagram illustrating these classifications is shown in Figure 1.

The name "coronavirus" is derived from the Latin word *corona*, meaning "crown," referring to the virus's crown-like appearance under an electron microscope due to spike proteins protruding from its envelope. Additionally, the term *Nido*, meaning "nest" in Latin, this refers to the virus's ability to generate a nested set of subgenomic mRNAs.[23–25]

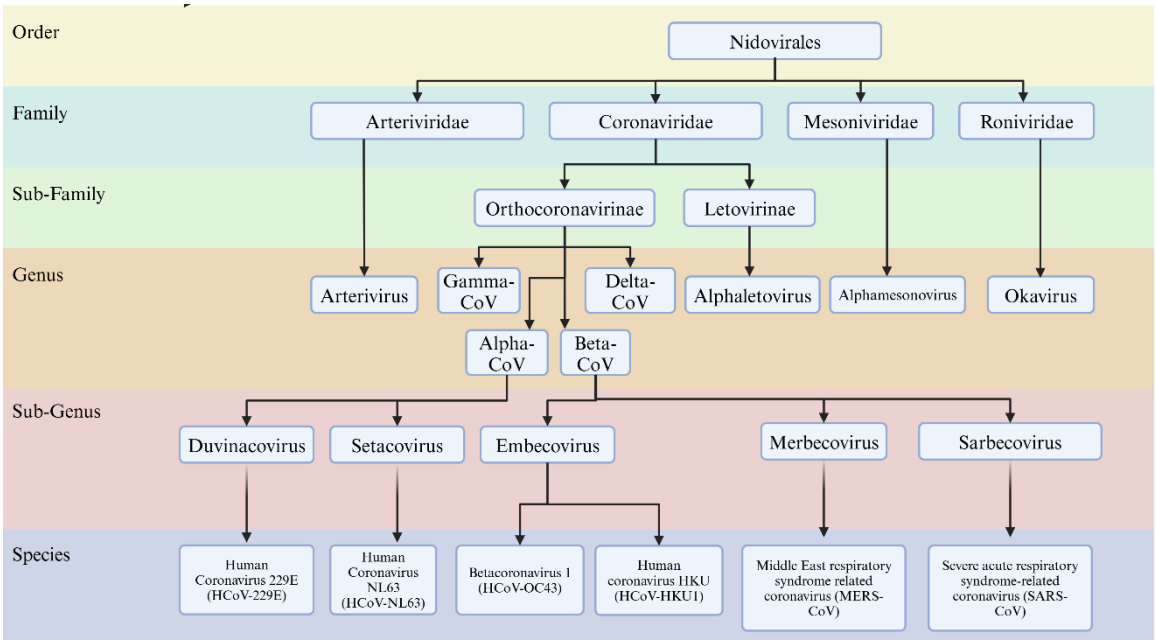

Figure 1.2 Classification of *Coronaviridae* according to the International Committee of Taxonomy of Viruses. This figure was created with BioRender.com.

History of Coronaviruses

Coronaviruses have been evolving for over a thousand years.[26] The first coronaviruses were isolated from chickens in 1937 with the discovery of infectious bronchitis virus (IBV) and from mice in 1949 with murine hepatitis virus (MHV).[27,28] Human coronaviruses were first characterized in the 1960s from respiratory tract infections.[29]

As its name suggests, SARS-CoV-2 is the second identified strain of SARS-CoV. The first strain, SARS-CoV, caused the 2002–2004 SARS outbreak, which originated in Guangdong Province, China. The virus spread to 29 countries, resulting in 8,422 reported cases and 916 deaths.[30] The disease presented as atypical pneumonia with symptoms including fever, headache, and respiratory distress, which in severe cases led to respiratory failure.[31] Genome sequencing linked SARS-CoV to a virus found in Himalayan palm civets, suggesting they served as an intermediate host, with bats as the natural reservoir.[32,33]

Another significant coronavirus within this family is Middle East respiratory syndrome coronavirus (MERS-CoV), which caused the 2012 MERS outbreak. Symptoms ranged from mild upper respiratory illness to severe pneumonia and multi-organ failure.[34] Both the SARS and MERS outbreaks led to severe human diseases.[35] Most of these cases were reported in Saudi Arabia.[36] The genome sequence for MERS-CoV closely resembles bat coronaviruses HKU4 and HKU5.[37]

In addition to these highly pathogenic coronaviruses, there are four other known human coronaviruses: HCoV-229E, HCoV-NL63, HCoV-OC43, and HCoV-HKU1. These typically cause milder symptoms resembling the common cold. These strains are also depicted in Figure 1.1. [38]

SARS-CoV-2 Biology

SARS-CoV-2 shares approximately 82% sequence identity with SARS-CoV based on whole genome alignment.[6,9] These alignments revealed 380 amino acid substitutions between the two viruses. Of these, 348 occur in nonstructural proteins (including *ORF1ab, 3a, 3b, 7a, 7b, 9b*, and *ORF14*), 27 are found in the spike protein, and 5 in the nucleocapsid protein.[39]

SARS-CoV-2 has a ~30 kb genome, which is one of the largest known RNA genomes.[39] the genome contains 14 open reading frames (ORFs), preceded by transcriptional regulatory sequences. The two main transcriptional subunits are ORF1a and ORF1b, these two encode polyprotein 1a (PP1a) and polyprotein 1ab (PP1ab). PP1ab makes Nsp1-16 which are responsible for making the complex replicase machinery.[40,41] At the 3' end the viral genome encodes four structural proteins: the spike protein (S), the envelope protein (E), and the nucleocapsid protein (N).[4,40,42] Throughout the structural genes, there are also nine ORFs for accessory factors. [43] The genome can be seen depicted in Figure 1.2.

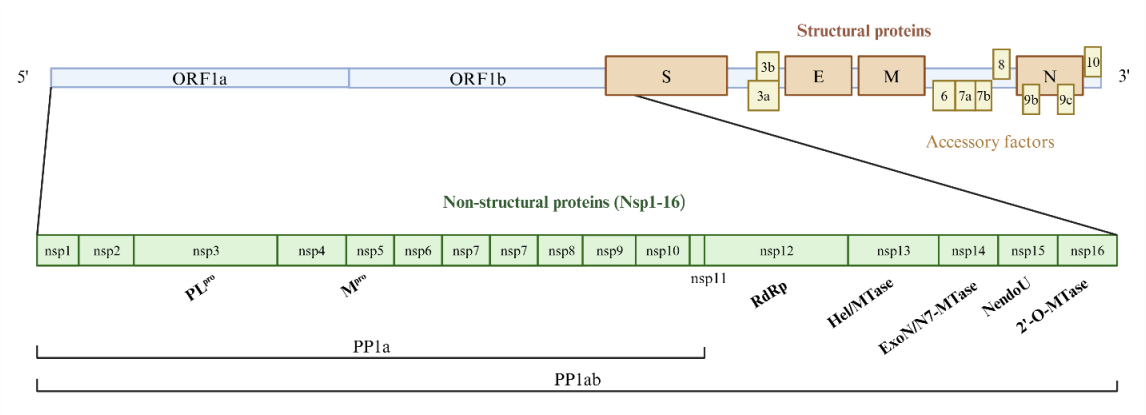

Figure 1.2 The genome of SARS-CoV-2 can be seen as organized by individual ORFS. This figure was created with BioRender.com.

Viral entry, attachment to the host cell membrane, and fusion are mediated by the spike (S) glycoprotein. The S protein assembles as a homotrimer and is inserted into the viral membrane, giving the virus its characteristic crown-like appearance. Upon entry into the host cell, the S protein is cleaved by proprotein convertases.[44,45] It is then further cleaved in the Golgi apparatus by furin into the S1 and S2 subunits. The S1 subunit binds to angiotensin-converting enzyme 2 (ACE2), while the S2 subunit anchors the S protein to the membrane, facilitating membrane fusion.[44]

In normal physiology, ACE2 is responsible for converting angiotensin I to angiotensin II. However, when SARS-CoV-2 binds to ACE2, this receptor is downregulated, contributing to disease severity by disrupting the renin-angiotensin-aldosterone system. This disruption plays a critical role in the development of lethal lung failure.[46]

After viral entry through membrane proteins, the virion is internalized via endocytosis, and fusion occurs following spike cleavage. This process leads to the release of the genomic RNA (gRNA).[44,47] The capped and polyadenylated gRNA is used for translation of ORF1a and ORF1b, resulting in the synthesis of two large polyproteins, pp1a and pp1b. These polyproteins are proteolytically cleaved into 16 nonstructural proteins (nsps) by the papain-like protease (PL^{pro}) in nsp3 and the main protease (M^{pro}) in nsp5.[48,49] Nsp1 is rapidly released into the cytoplasm, where it interferes with host translation and the innate immune response. [50–52] Nsp2 through nsp16 establish the viral replication and transcription complexes.

Coronaviruses induce extensive reorganization of host intracellular membranes to create replication organelles.[53] The endoplasmic reticulum (ER) is remodeled into a network of double-membrane vesicles (DMVs) attached to the ER via thin double-membrane connectors derived from collapsed ER tubules.[54] Nsp3, nsp4, and nsp6 contain multiple transmembrane domains that contribute to the formation of the replication organelles.[55,56] Coexpression of nsp3 on the outer membrane and nsp4 on the inner membrane facilitates the formation of double-membrane vesicles.[56,57] Nsp6 plays a key role in establishing connections between the double-membrane vesicles and the ER, serving as a spatial organizer for these vesicle clusters.[55]

With the exception of nsp1, the nonstructural proteins assemble into a replication and transcription complex that facilitates viral RNA synthesis.[58] The holoenzyme responsible for RNA synthesis consists of nsp12, the nsp7-nsp8 heterodimer, and an additional nsp8. Nsp12 contains the RNA-dependent RNA polymerase (RdRp) domain, while nsp7 and nsp8 act as co-factors to stabilize the RdRp.[59,60] Nsp8 also serves as a scaffold for viral proteins, aiding in RNA unwinding and proofreading, and is involved in RNA capping.[58] Nsp13, the viral helicase, is responsible for unwinding the highly structured viral genome.[61,62]

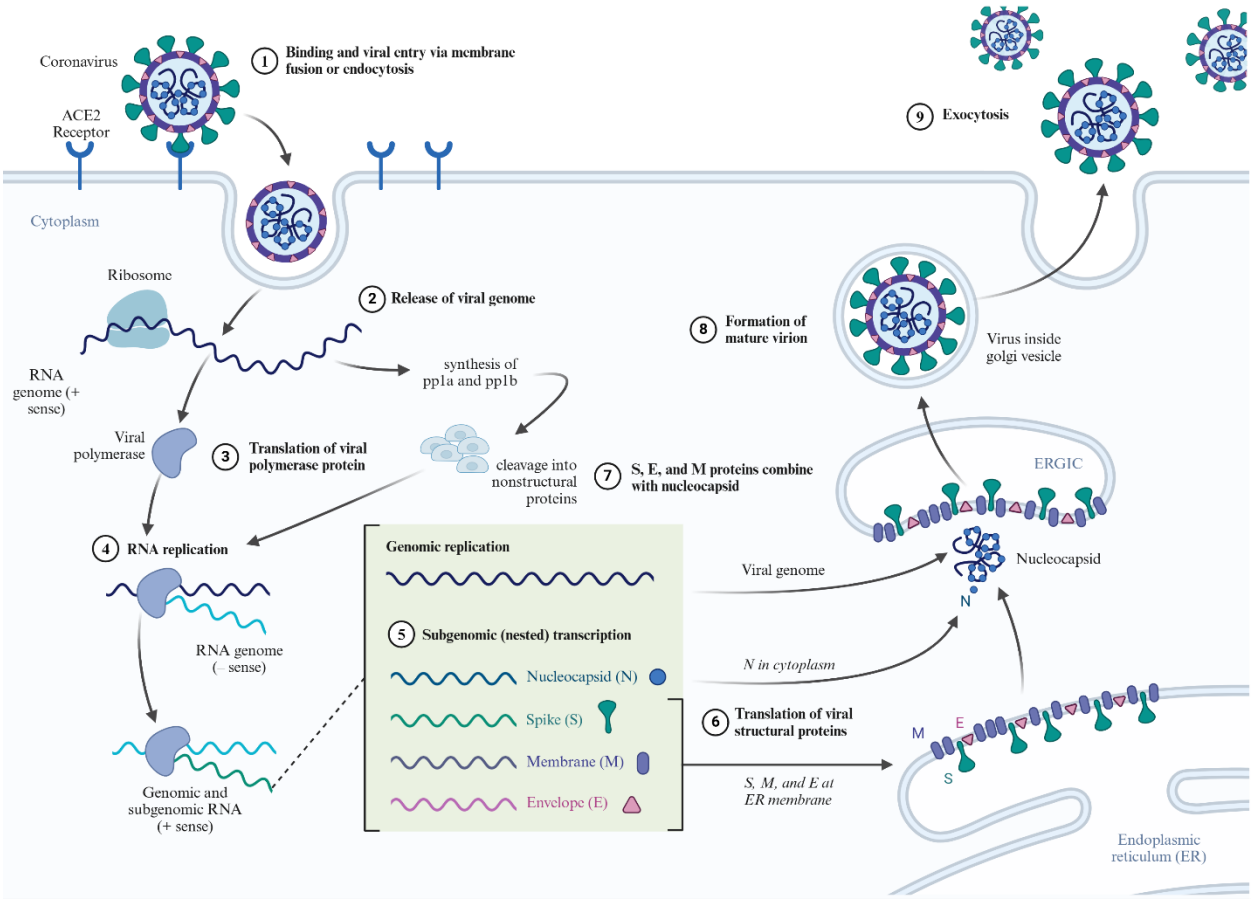

Figure 1.3 The viral biology and process of replication in SARS-CoV-2. This figure was created with BioRender.com.

The RNA-dependent RNA polymerase (RdRp) in SARS-CoV-2 is one of the fastest viral RdRps, however, this speed comes at the cost of low accuracy, which may benefit the virus by allowing it to better adapt to selective pressures.[63] Due to this low fidelity, the virus employs proofreading mechanisms to enhance replication and maintain genomic stability.[64] Proofreading is carried out by the N-terminal 3' to 5' exoribonuclease (ExoN) domain within nsp14. Nsp14 binds to nsp10, forming the RNA proofreading machinery that removes misincorporated nucleotides.[65,66]

After the replication and transcription complex (RTC) is assembled, the viral gRNA serves as a template for both replication and transcription. The RTC synthesizes a full negative-sense copy of the viral genome, which then acts as a template for the positive-sense gRNA. The newly synthesized genomes are used to generate additional nonstructural proteins (nsps) and RTCs, or

they become part of new virions. [67] Viral translation occurs through a discontinuous process, producing a set of nested 3' and 5' co-terminal subgenomic RNAs (sgRNAs).[68] During negative-strand RNA synthesis, the RTC interrupts transcription upon encountering transcription regulatory sequences (TRS). Upon reaching a TRS, transcription stops and is reinitiated at the TRS next to the leader sequence. When reinitiation occurs, a negative-strand copy of the leader sequence is added to the developing RNA, completing the synthesis of the sgRNA.[40,69,70] These sgRNA are used as templates to transcribe the positive sensed sgRNAs that are then used for the translation of structural and accessory proteins.[71]

Virion packaging begins with the assembly of the N protein, synthesized in the cytosol, and the viral gRNA into ribonucleoproteins (RNPs). The N protein selectively binds the viral gRNA, excluding sgRNA and cellular RNA, to form the ribonucleoprotein complex. This complex then interacts with the M protein, which ensures proper packaging into the virus particle. Meanwhile, the M, E, and S proteins are synthesized in the endoplasmic reticulum (ER).[72] The RNP must locate the M/S/E protein clusters for packaging into new virions. The N protein binds to the cytoplasmic tail of the M protein, this promotes the packaging of viral RNPs and potentially stimulating M oligomerization, which aids in particle formation.[73] This process occurs in the ER-Golgi intermediate compartment (ERGIC), where N, S, and M proteins accumulate.[74] Newly formed single-membrane vesicles bud off from the ERGIC.[72,75] The precise mechanism by which SARS-CoV-2 and other coronaviruses bud remains unclear, as it does not follow typical viral budding pathways. It is suggested that the E protein may play a role, as it is highly conserved and is responsible for budding in other viruses.[76–78] Studies have reported that the E protein induces asymmetry between the two leaflets of the lipid bilayer, which favors vesicle formation.[79] However, the full mechanism of budding is still under investigation.

The egress of SARS-CoV-2 follows a lysosome-dependent pathway.[80] The exact mechanism by which SARS-CoV-2 particles reach the lysosomes remains unclear, however, it is known that the viral particles are transported to the lysosomes after their formation in the ERGIC.[81] ORF3a plays a role in promoting the movement of lysosomes towards the periphery of the cytoplasm, where they are eventually released.[82,83]

SARS-CoV-2 Immune Evasion Mechanisms

A key factor contributing to the persistence of SARS-CoV-2 is its ability to evade and suppress the host immune response through a range of strategies. These include shielding viral replication intermediates, mimicking host molecular structures, disrupting antiviral signaling pathways, and suppressing interferon responses.[54,84–95] These mechanisms allow the virus to establish infection, replicate efficiently, and delay immune detection, contributing to disease severity.

Host Immune Response

Upon viral entry, SARS-CoV-2 is detected by host pattern recognition receptors (PRRs), including Toll-like receptors (TLRs) and RIG-I-like receptors (RLRs), which sense viral RNA and initiate innate immune signaling. [96,97] TLR2, TLR3, TLR7, TLR8, and cytosolic sensors such as MDA5 and LGP2 play pivotal roles in recognizing viral components, leading to the production of pro-inflammatory cytokines (such as TNF, IL-6, IFN-γ) and type I/III interferons (IFN-I, IFN-III).[98–100] MDA5, in particular, serves as the primary sensor of SARS-CoV-2 RNA, detecting long double-stranded RNA intermediates generated during replication.[100,101]

Activation of these pathways triggers downstream signaling via mitochondrial antiviral signaling proteins (MAVS), promoting phosphorylation and nuclear translocation of IRF3 and IRF7, which induce interferon expression.[102,103] Secreted interferons engage JAK/STAT pathways, via IFNAR or IFNLR receptors, culminating in the formation of the ISGF3 complex and activation of interferon-stimulated genes (ISGs).[104,105] These ISGs coordinate a broad antiviral response by inhibiting viral entry, replication, transcription, and assembly, forming a critical defense against SARS-CoV-2.

In parallel, SARS-CoV-2 activates additional host defenses such as the cGAS-STING pathway through mitochondrial damage, and the NLRP3 inflammasome via viral RNA and nucleocapsid protein recognition, contributing to inflammatory responses and, in severe cases, cytokine storms.[106–113]

To overcome these defenses, SARS-CoV-2 employs a comprehensive immune evasion strategy. Viral proteins, including nonstructural proteins (NSP1, NSP3, NSP5, NSP12–15), structural proteins (M, N), and accessory proteins (ORF3a, ORF6, ORF7a/b, ORF8, ORF9b) target

nearly every stage of innate immune signaling.[90,91,94,95,114] These proteins inhibit PRR signaling by blocking IRF3 phosphorylation, degrading MAVS and TBK1, and disrupting nuclear transport through interactions with importins and nucleoporins.[115–118] Additionally, SARS-CoV-2 impairs downstream IFN signaling by degrading IFN receptors (such as Nsp14-mediated IFNAR1 degradation), preventing STAT1/STAT2 phosphorylation, and inhibiting ISGF3 nuclear translocation. Accessory proteins like ORF6, ORF7a, and N further interfere with JAK/STAT signaling and ISG expression.[88,94,114]

This multilayered suppression of antiviral responses enables SARS-CoV-2 to establish infection before the immune response can be activated. This then contributes to viral persistence, immune dysregulation, and disease severity. The redundancy of these evasion mechanisms underscores the virus's evolutionary adaptation to circumvent innate immunity and highlights the challenges in developing therapeutics that can restore or enhance host antiviral defenses.

Avoiding Host Detection

Viruses manage to survive and evolve by avoiding detection, similarly SARS-CoV-2 has done the same. Typically, virus derived RNA can be detected via its missing modifications, inclusion of virus-distinguishing elements, or the presence of extensive secondary structures.[119] Virus-DNA can be identified by its location in the cell or by aspects of its sequence that might not be present within the host.[120] These unique characteristics are what is called pathogen-associated molecular patterns (PAMPs). The detection of PAMPs in cells is either a direct process or aided by autophagy.[121] This is why avoiding viral detection is crucial is crucial for the virus' survival.

To avoid host detection the viral genomic RNA conforms to the rules of host translation. Coronaviruses modify the 5'-triphosphate(ppA) of their genomic RNA and sgRNA via capping and methylation which not only allows for ribosomal loading but also for evading host detection. The capping process occurs as four sequential steps. The first is the removal of γ-phosphate from pppA to form the 5'diphosphate (ppA). Then, guanylyltransferase creates the cap core structure by transferring guanine monophosphate to the ppA. This is followed by the formation of the core structure by methylation of the guanine at position N7 by N7-methyltransferase. As the last part of this process, 2'-*O*-methyltransferase methylates the ribose at the 2'-*O* position of the first transcribed nucleotide, making the final capped structure.[122]

The result of this masking mechanism in the viruses results in a late detection by the host immune response. As viral RNA synthesis continues dsRNA intermediates trigger host immune response. This is because both genomic RNA and sgRNA need to proceed through negative strand intermediates. Therefore, the virus has evolved mechanism that decrease the early detection of dsRNA by minimizing its accumulation and hiding it from the host. Nsp15 is responsible for minimizing the negative-stranded RNA and dsRNA through its endonuclease activity, which targets the negative-sense transcripts. [123,124] At the same time, the virus induces the assembly of double-membrane vesicles (DMVs) that compartmentalize the viral replication away from cellular sensors.[125,126] These replication organelles (ROs) diminish the host capacity to recognize the presence of a viral infection by exploiting autophagy biology.[127,128] The assembly of RO is mediated by Nsp3 and Nsp4 with Nsp6 forming a tether to the ER that allows for the flow of lipids.[55] The time it takes to build the levels of Nsp3, Nsp4, Nsp6 and Nsp15 is slow enough that at even at low multiplicity the optimal infection has already been achieved.

SARS-CoV-2 employs a multifaceted immune evasion strategy, combining molecular mimicry, RNA shielding, and active suppression of host antiviral pathways. These mechanisms allow the virus to delay immune detection, suppress interferon responses, and manipulate host cellular machinery, which all contribute to its high infectivity and pathogenicity. Among the numerous viral proteins involved, Nsp1 plays a particularly critical role as a key immune evasion factor. By shutting down host protein synthesis and interfering with innate immune signaling, Nsp1 serves as a central player in the virus's ability to suppress host defenses. Given its pivotal function and conserved nature, Nsp1 has emerged as a compelling target for therapeutic intervention.

Nsp1

An important part of viral strategy is what is called "host shut off, " this is the process in which the virus impairs the translation of mRNA. In doing so it helps redirect translation resources and it blocks the ability of infected cell to respond to the virus.[129] SARS-CoV-2 leads to shut off of host protein synthesis and Nsp1 is one of the central factors in coronaviruses that inhibit host cellular mRNA translation.[52]

Upon SARS-CoV-2 infection, the overlapping reading frames ORF1ab are translated from the positive-sense genomic RNA to form a polypeptide that is then autoproteolyzed into 16 non structural proteins (nsps).[130] The first of these proteins is Nsp1.

Nsp1 uses a multipronged strategy to shut down host protein synthesis.[131] Nsp1 binds to the 40S ribosomal subunit, in doing so its C-terminal domain blocks the mRNA entry channel by adopting a helix turn helix shape, this then leads to reduction in translation.[50,51,132,133] Through this process, it promotes cellular mRNA degradation. Nsp1 also interacts with export factor NXF1 to inhibit the nuclear export of cellular transcripts.[134]

The interaction of binding to the 40S ribosomal subunit is crucial for translation inhibition. The first C-terminal helix (residues 153-160) interact with ribosomal proteins uS5 and uS3, through a few of the hydrophobic side chains including Y154, F157 and W161. The two helices that form the helix-turn-helix shape that disrupt the mRNA entry channel are connected by a short loop that contains K164 and H165. K164 and H165 establish stacking interactions with the helix of h18 of the 18S rRNA through U607 and U630 as well as backbone binding. K164 and H165 are important to the virus as without them it can no longer promote mRNA degradation, it no longer inhibits translation, and it stops inducing type 1 IFN expression.[135] The second helix (residues 166-178) interact with the phosphate backbone of h18 through the conserved arginines R171 and R175 and also with ribosomal protein eS30. Nsp1 also sterically occludes the entrance of the 43S pre-initation complex and the non-translating 80S ribosomes. This indicates that Nsp1 interacts with multiple different ribosomal states. [51]

The process of inhibiting nuclear mRNA export through NXF1 is done through the N-terminal of Nsp1 (residues 1-129) and is independent of the C-terminal domain that blocks the ribosome. By directly binding to NXF1 it disrupts the interactions with mRNA export adaptors and the nuclear pore complex. Nsp1 is visible in the cytoplasm and near the nuclear pore complexes, which indicate that it could shuttling between the nucleus and the cytoplasm.[134]

It is clear that the C-terminal region of Nsp1 is an important player for controlling cellular response to viral infections. It would make an excellent target for combatting the virus as it plays a crucial role in shutting down the host immune response. Drug design for Nsp1 would need to

prevent binding to the ribosome to allow cellular defense systems the ability to respond to the virus.

Intrinsically Disordered Proteins

The C-terminal of Nsp1 that is responsible for binding to the 40S ribosome is considered an intrinsically disordered protein region (IDPR). Therefore, the following section will give insights into and characterize what it means for a protein to be disordered or have intrinsically disordered regions.

There are two paradigms regarding the structure and function of proteins. The first is the well-known 'structure-function paradigm,' this paradigm states that the native structure of a protein under physiological conditions is what is needed for the protein to function. The second is the 'disorder-function paradigm,' this paradigm is based on proteins that perform cellular functions without attaining a stable structure under physiological conditions.[136]

Intrinsically disordered proteins (IDPs) fall into the 'disorder-function paradigm,' they are proteins that cannot attain a single stable three-dimensional structure under physiological conditions, instead they are constantly changing and are in various conformational states. These types of proteins are highly abundant in the proteome.

Intrinsically disordered proteins are characterized by their biased amino acid composition, low sequence complexity, low proportion of bulky hydrophobic residues and high proportions of hydrophilic amino acids. These proteins do not fold spontaneously into stable, defined three dimensional structures. They are dynamically disordered and fluctuate between a range of conformations.[137,138]

The propensity of a protein to fold or not fold is contained within the amino acid sequence of the protein. The number, charge, and relative positioning of charged residues is an important determinant of the properties of IDRs. A large reason for the unfolded structures of IDPs is their strong electrostatic repulsion due to a higher net charge and a lack of driving force due to low average hydrophobicity.[139] Residues such as alanine, arginine, glycine, glutamic acid, glutamine, lysine, proline and serine occur more often in IDPs/IDPRs. [140–142] Aromatic residues allow for intramolecular interactions driven by their side chain π-π interactions, cation-π

interactions, and methyl-π interactions.[143–145] Aliphatic residues drive intramolecular interactions through the hydrophobic effect and desolvation.

Upon the interaction of IDPs/IDPRs with their specific binding partner, the protein/region will adopt a disorder to order conformational transition known as 'induced folding.' [137,138,141,146] These disordered proteins can also bind to multiple partners and take on different conformations. [147,148] The process in which these disordered proteins fold upon binding with their targets is a process called coupled folding and binding.[149,150] There are studies that suggest that there are pre-formed secondary structural elements in the conformational ensemble that favor the binding process.[151] Not all intrinsically disordered proteins undergo folding to perform their biological function, some remain disordered even after binding to their targets, forming 'fuzzy' complexes.[152–155]

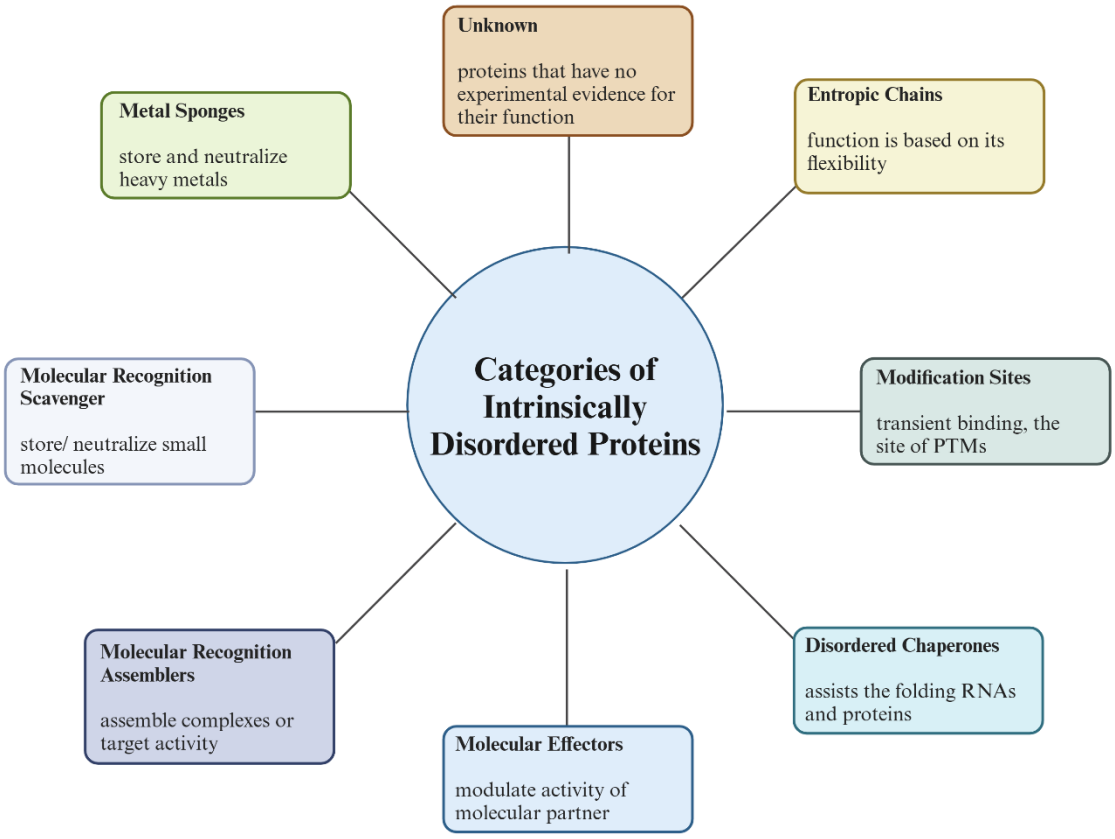

Figure 1.4 The 8 main categories of intrinsically disorder proteins.
Figure was created with BioRender.com.

IDPs and IDPRs have been classified into 8 different categories based on their biological function: entropic chains, modifications sites, disordered chaperones, molecular effectors, molecular recognition assemblers, molecular recognition scavengers, metal sponges and those of unknown class (Figure 1.4).[156] Entropic chains never adopt a structural function while they perform their biological function, this would include things like flexible linkers and spacers.[157,158] Modification sites refer to IDPs/IDPRs that facilitate the electrostatic interactions with the lipid head groups in the membranes, which allow for fine tuning of the signaling pathways. These tend to have transient binding and are the sites of post translational modifications. [159] Disordered chaperones are proteins that help RNA and other proteins attain their functional folded state.[160–162] Molecular recognition effectors bind permanently to other proteins and modify their actions.[163] Molecular assemblers interact with multiple binding partners in order to form higher-order protein complexes.[155] Molecular effectors store and neutralize small ligands. Metal sponges are IDPs/IDPRs that can store and neutralize heavy metals. The unknown category refers to IDPs/IDPRs who do not have an established functional role.[156] Understanding these functional classifications is essential, as they highlight how intrinsic disorder equips proteins with unique capabilities absent in structured proteins. The flexibility inherent to IDPs allows them to engage in transient, promiscuous, or highly specific interactions, often acting as central hubs in cellular signaling pathways. This dynamic nature enables rapid responses to environmental changes, regulation through post-translational modifications, and the ability to bind multiple partners via conformational adaptability.

Viruses exploit intrinsically disordered regions to enhance pathogenicity. Many viral proteins leverage disorder to modulate host processes, evade immune surveillance, and hijack cellular machinery. The disordered regions often mimic host motifs, facilitating interactions with key regulatory proteins while remaining elusive to immune detection.[164]

Despite their biological importance, targeting IDPs poses significant challenges due to their lack of stable structure. The intrinsically disordered nature of Nsp1's C-terminal region presents both a challenge and an opportunity for therapeutic development. While its lack of a stable structure under physiological conditions complicates traditional structure-based drug design, the conformational plasticity of this region allows for dynamic and potentially selective interactions with small molecules, peptides, or metal complexes. The ability of IDPs and IDPRs to undergo

induced folding or remain in 'fuzzy' complexes upon binding provides a unique avenue for modulating their function. Given the critical role of Nsp1 in immune suppression and its reliance on a disordered region to bind the ribosome, targeting this domain represents a promising and underexplored antiviral strategy.

Problem Statement and Research Approach

SARS-CoV-2 continues to pose a global health challenge, not only due to its rapid transmission and mutation rates but also because of its immune evasion mechanisms. Key to these mechanisms is nonstructural protein 1 (Nsp1), a key virulence factor responsible for shutting down host protein synthesis and impairing innate immune responses. Despite its critical role in viral pathogenicity, Nsp1 has received comparatively less attention as a therapeutic target than structural proteins such as the spike (S) glycoprotein.

A major feature that complicates traditional drug design efforts against Nsp1 is the intrinsically disordered nature of its C-terminal region. This disordered segment is essential for binding to the 40S ribosomal subunit, where it adopts a helix–turn–helix conformation upon interaction, effectively blocking host mRNA translation. The dynamic and flexible characteristics of intrinsically disordered protein regions (IDPRs) present both challenges and unique opportunities in drug discovery. Unlike well-structured proteins, IDPRs lack stable binding pockets in their unbound state, making conventional structure-based drug design approaches less effective. However, their conformational flexibility allows for diverse modes of interaction, particularly with small molecules or metal complexes capable of inducing or stabilizing specific conformations.

Given Nsp1's pivotal role in immune suppression and its highly conserved sequence across SARS-CoV-2 variants, it represents a compelling yet underexplored target for antiviral intervention. Targeting the C-terminal IDPR of Nsp1 offers the potential to disrupt its interaction with the ribosome, thereby restoring host translation and immune function.

The research presented in this thesis focuses on leveraging metal coordination chemistry, specifically using copper(II) and cobalt(II/III) complexes, as a novel strategy to modulate the structure and function of Nsp1. Metal complexes offer a versatile platform for interacting with

disordered regions due to their ability to form stable coordination bonds with amino acid side chains, particularly histidine residues. By exploiting these properties, this work aims to investigate whether metal-based compounds can effectively bind to Nsp1, alter its conformation, and impair its ability to inhibit host translation.

References

(1)Dong, E.; Du, H.; Gardner, L. An Interactive Web-Based Dashboard to Track COVID-19 in Real Time. *The Lancet Infectious Diseases* **2020**, *20* (5), 533–534. https://doi.org/10.1016/S1473-3099(20)30120-1.

(2)Van Egeren, D.; Novokhodko, A.; Stoddard, M.; Tran, U.; Zetter, B.; Rogers, M.; Pentelute, B. L.; Carlson, J. M.; Hixon, M.; Joseph-McCarthy, D.; Chakravarty, A. Risk of Rapid Evolutionary Escape from Biomedical Interventions Targeting SARS-CoV-2 Spike Protein. *PLoS One* **2021**, *16* (4), e0250780. https://doi.org/10.1371/journal.pone.0250780.

(3)Huang, C.; Wang, Y.; Li, X.; Ren, L.; Zhao, J.; Hu, Y.; Zhang, L.; Fan, G.; Xu, J.; Gu, X.; Cheng, Z.; Yu, T.; Xia, J.; Wei, Y.; Wu, W.; Xie, X.; Yin, W.; Li, H.; Liu, M.; Xiao, Y.; Gao, H.; Guo, L.; Xie, J.; Wang, G.; Jiang, R.; Gao, Z.; Jin, Q.; Wang, J.; Cao, B. Clinical Features of Patients Infected with 2019 Novel Coronavirus in Wuhan, China. *The Lancet* **2020**, *395* (10223), 497–506. https://doi.org/10.1016/S0140-6736(20)30183-5.

(4)Zhou, P.; Yang, X.-L.; Wang, X.-G.; Hu, B.; Zhang, L.; Zhang, W.; Si, H.-R.; Zhu, Y.; Li, B.; Huang, C.-L.; Chen, H.-D.; Chen, J.; Luo, Y.; Guo, H.; Jiang, R.-D.; Liu, M.-Q.; Chen, Y.; Shen, X.-R.; Wang, X.; Zheng, X.-S.; Zhao, K.; Chen, Q.-J.; Deng, F.; Liu, L.-L.; Yan, B.; Zhan, F.-X.; Wang, Y.-Y.; Xiao, G.-F.; Shi, Z.-L. A Pneumonia Outbreak Associated with a New Coronavirus of Probable Bat Origin. *Nature* **2020**, *579* (7798), 270–273. https://doi.org/10.1038/s41586-020-2012-7.

(5)Chan, J. F.-W.; Yuan, S.; Kok, K.-H.; To, K. K.-W.; Chu, H.; Yang, J.; Xing, F.; Liu, J.; Yip, C. C.-Y.; Poon, R. W.-S.; Tsoi, H.-W.; Lo, S. K.-F.; Chan, K.-H.; Poon, V. K.-M.; Chan, W.-M.; Ip, J. D.; Cai, J.-P.; Cheng, V. C.-C.; Chen, H.; Hui, C. K.-M.; Yuen, K.-Y. A Familial Cluster of Pneumonia Associated with the 2019 Novel Coronavirus Indicating Person-to-Person Transmission: A Study of a Family Cluster. *The Lancet* **2020**, *395* (10223), 514–523. https://doi.org/10.1016/S0140-6736(20)30154-9.

(6)Paraskevis, D.; Kostaki, E. G.; Magiorkinis, G.; Panayiotakopoulos, G.; Sourvinos, G.; Tsiodras, S. Full-Genome Evolutionary Analysis of the Novel Corona Virus (2019-nCoV) Rejects the Hypothesis of Emergence as a Result of a Recent Recombination Event. *Infect Genet Evol.* **2020**, *79*, 104212. https://doi.org/10.1016/j.meegid.2020.104212.

(7)Luis, A. D.; Hayman, D. T. S.; O'Shea, T. J.; Cryan, P. M.; Gilbert, A. T.; Pulliam, J. R. C.; Mills, J. N.; Timonin, M. E.; Willis, C. K. R.; Cunningham, A. A.; Fooks, A. R.; Rupprecht, C. E.; Wood, J. L. N.; Webb, C. T. A Comparison of Bats and Rodents as Reservoirs of Zoonotic Viruses: Are Bats Special? *Proc. R. Soc. B.* **2013**, *280* (1756), 20122753. https://doi.org/10.1098/rspb.2012.2753.

(8)Rothe, C.; Schunk, M.; Sothmann, P.; Bretzel, G.; Froeschl, G.; Wallrauch, C.; Zimmer, T.; Thiel, V.; Janke, C.; Guggemos, W.; Seilmaier, M.; Drosten, C.; Vollmar, P.; Zwirglmaier, K.; Zange, S.; Wölfel, R.; Hoelscher, M. Transmission of 2019-nCoV Infection from an Asymptomatic Contact in Germany. *N Engl J Med* **2020**, *382* (10), 970–971. https://doi.org/10.1056/NEJMc2001468.

(9)Chan, J. F.-W.; Kok, K.-H.; Zhu, Z.; Chu, H.; To, K. K.-W.; Yuan, S.; Yuen, K.-Y. Genomic Characterization of the 2019 Novel Human-Pathogenic Coronavirus Isolated from a Patient with Atypical Pneumonia after Visiting Wuhan. *Emerg Microbes Infect* **2020**, *9* (1), 221–236. https://doi.org/10.1080/22221751.2020.1719902.

(10)Cowling, B. J.; Leung, G. M. Epidemiological Research Priorities for Public Health Control of the Ongoing Global Novel Coronavirus (2019-nCoV) Outbreak. *Eurosurveillance* **2020**, *25* (6). https://doi.org/10.2807/1560-7917.ES.2020.25.6.2000110.

(11)Krammer, F. SARS-CoV-2 Vaccines in Development. *Nature* **2020**, *586* (7830), 516–527. https://doi.org/10.1038/s41586-020-2798-3.

(12)Zhou, Y.; Jiang, S.; Du, L. Prospects for a MERS-CoV Spike Vaccine. *Expert Rev Vaccines* **2018**, *17* (8), 677–686. https://doi.org/10.1080/14760584.2018.1506702.

(13)Mubarak, A.; Alturaiki, W.; Hemida, M. G. Middle East Respiratory Syndrome Coronavirus (MERS-CoV): Infection, Immunological Response, and Vaccine Development. *J Immunol Res* **2019**, *2019*, 6491738. https://doi.org/10.1155/2019/6491738.

(14)Modjarrad, K. MERS-CoV Vaccine Candidates in Development: The Current Landscape. *Vaccine* **2016**, *34* (26), 2982–2987. https://doi.org/10.1016/j.vaccine.2016.03.104.

(15)Su, S.; Du, L.; Jiang, S. Learning from the Past: Development of Safe and Effective COVID-19 Vaccines. *Nat Rev Microbiol* **2021**, *19* (3), 211–219. https://doi.org/10.1038/s41579-020-00462-y.

(16)Creech, C. B.; Walker, S. C.; Samuels, R. J. SARS-CoV-2 Vaccines. *JAMA* **2021**, *325* (13), 1318–1320. https://doi.org/10.1001/jama.2021.3199.

(17)Dai, L.; Gao, G. F. Viral Targets for Vaccines against COVID-19. *Nat Rev Immunol* **2021**, *21* (2), 73–82. https://doi.org/10.1038/s41577-020-00480-0.

(18)Folegatti, P. M.; Ewer, K. J.; Aley, P. K.; Angus, B.; Becker, S.; Belij-Rammerstorfer, S.; Bellamy, D.; Bibi, S.; Bittaye, M.; Clutterbuck, E. A.; Dold, C.; Faust, S. N.; Finn, A.; Flaxman, A. L.; Hallis, B.; Heath, P.; Jenkin, D.; Lazarus, R.; Makinson, R.; Minassian, A. M.; Pollock, K. M.; Ramasamy, M.; Robinson, H.; Snape, M.; Tarrant, R.; Voysey, M.; Green, C.; Douglas, A. D.; Hill, A. V. S.; Lambe, T.; Gilbert, S. C.; Pollard, A. J.; Oxford COVID Vaccine Trial Group. Safety and Immunogenicity of the ChAdOx1 nCoV-19 Vaccine against SARS-CoV-2: A Preliminary Report of a Phase 1/2, Single-Blind, Randomised Controlled Trial. *Lancet* **2020**, *396* (10249), 467–478. https://doi.org/10.1016/S0140-6736(20)31604-4.

(19)Stephenson, K. E.; Le Gars, M.; Sadoff, J.; de Groot, A. M.; Heerwegh, D.; Truyers, C.; Atyeo, C.; Loos, C.; Chandrashekar, A.; McMahan, K.; Tostanoski, L. H.; Yu, J.; Gebre, M. S.; Jacob-Dolan, C.; Li, Z.; Patel, S.; Peter, L.; Liu, J.; Borducchi, E. N.; Nkolola, J. P.; Souza, M.; Tan, C. S.; Zash, R.; Julg, B.; Nathavitharana, R. R.; Shapiro, R. L.; Azim, A. A.; Alonso, C. D.; Jaegle, K.; Ansel, J. L.; Kanjilal, D. G.; Guiney, C. J.; Bradshaw, C.; Tyler, A.; Makoni, T.; Yanosick, K. E.; Seaman, M. S.; Lauffenburger, D. A.; Alter, G.; Struyf, F.; Douoguih, M.; Van Hoof, J.; Schuitemaker, H.; Barouch, D. H. Immunogenicity of the Ad26.COV2.S Vaccine for COVID-19. *JAMA* **2021**, *325* (15), 1535–1544. https://doi.org/10.1001/jama.2021.3645.

(20)Legros, V.; Denolly, S.; Vogrig, M.; Boson, B.; Siret, E.; Rigaill, J.; Pillet, S.; Grattard, F.; Gonzalo, S.; Verhoeven, P.; Allatif, O.; Berthelot, P.; Pélissier, C.; Thiery, G.; Botelho-Nevers, E.; Millet, G.; Morel, J.; Paul, S.; Walzer, T.; Cosset, F.-L.; Bourlet, T.; Pozzetto, B. A Longitudinal Study of SARS-CoV-2-Infected Patients Reveals a High Correlation between Neutralizing Antibodies and COVID-19 Severity. *Cell Mol Immunol* **2021**, *18* (2), 318–327. https://doi.org/10.1038/s41423-020-00588-2.

(21)Turner, J. S.; O'Halloran, J. A.; Kalaidina, E.; Kim, W.; Schmitz, A. J.; Zhou, J. Q.; Lei, T.; Thapa, M.; Chen, R. E.; Case, J. B.; Amanat, F.; Rauseo, A. M.; Haile, A.; Xie, X.; Klebert, M. K.; Suessen, T.; Middleton, W. D.; Shi, P.-Y.; Krammer, F.; Teefey, S. A.; Diamond, M. S.; Presti,

R. M.; Ellebedy, A. H. SARS-CoV-2 mRNA Vaccines Induce Persistent Human Germinal Centre Responses. *Nature* **2021**, *596* (7870), 109–113. https://doi.org/10.1038/s41586-021-03738-2.

(22)Goel, R. R.; Apostolidis, S. A.; Painter, M. M.; Mathew, D.; Pattekar, A.; Kuthuru, O.; Gouma, S.; Hicks, P.; Meng, W.; Rosenfeld, A. M.; Dysinger, S.; Lundgreen, K. A.; Kuri-Cervantes, L.; Adamski, S.; Hicks, A.; Korte, S.; Oldridge, D. A.; Baxter, A. E.; Giles, J. R.; Weirick, M. E.; McAllister, C. M.; Dougherty, J.; Long, S.; D'Andrea, K.; Hamilton, J. T.; Betts, M. R.; Luning Prak, E. T.; Bates, P.; Hensley, S. E.; Greenplate, A. R.; Wherry, E. J. Distinct Antibody and Memory B Cell Responses in SARS-CoV-2 Naïve and Recovered Individuals Following mRNA Vaccination. *Sci Immunol* **2021**, *6* (58), eabi6950. https://doi.org/10.1126/sciimmunol.abi6950.

(23) Knipe, D. M.; Howley, P. *Fields Virology*; Wolters Kluwer: Philadelphia, 2015.

(24)Tyrrell, D. A. J.; Almeida, J. D.; Cunningham, C. H.; Dowdle, W. R.; Hofstad, M. S.; McIntosh, K.; Tajima, M.; Zakstelskaya, L. Ya.; Easterday, B. C.; Kapikian, A.; Bingham, R. W. Coronaviridae. *Intervirology* **1975**, *5* (1–2), 76–82. https://doi.org/10.1159/000149883.

(25)Helmy, Y. A.; Fawzy, M.; Elaswad, A.; Sobieh, A.; Kenney, S. P.; Shehata, A. A. The COVID-19 Pandemic: A Comprehensive Review of Taxonomy, Genetics, Epidemiology, Diagnosis, Treatment, and Control. *J Clin Med* **2020**, *9* (4), 1225. https://doi.org/10.3390/jcm9041225.

(26)Forni, D.; Cagliani, R.; Clerici, M.; Sironi, M. Molecular Evolution of Human Coronavirus Genomes. *Trends in Microbiology* **2017**, *25* (1), 35–48. https://doi.org/10.1016/j.tim.2016.09.001.

(27)F.R. Beaudette; C.B. Hudson. Cultivation of the Virus of Infectious Bronchitis. *J Am Vet Med Assoc* **1937**, *90*, 51–60.

(28)Cheever, F. S.; Daniels, J. B.; Pappenheimer, A. M.; Bailey, O. T. A Murine Virus (JHM) Causing Disseminated Encephalomyetlitis with Extensive Destruction of Myelin. *J Exp Med* **1949**, *90* (3), 181–194. https://doi.org/10.1084/jem.90.3.181.

(29)Kahn, J. S.; McIntosh, K. History and Recent Advances in Coronavirus Discovery. *Pediatr Infect Dis J* **2005**, *24* (11), S223–S227. https://doi.org/10.1097/01.inf.0000188166.17324.60.

(30)Cherry, J. D.; Krogstad, P. SARS: The First Pandemic of the 21st Century. *Pediatr Res* **2004**, *56* (1), 1–5. https://doi.org/10.1203/01.PDR.0000129184.87042.FC.

(31)Graham, R. L.; Donaldson, E. F.; Baric, R. S. A Decade after SARS: Strategies for Controlling Emerging Coronaviruses. *Nat Rev Microbiol* **2013**, *11* (12), 836–848. https://doi.org/10.1038/nrmicro3143.

(32)Guan, Y.; Zheng, B. J.; He, Y. Q.; Liu, X. L.; Zhuang, Z. X.; Cheung, C. L.; Luo, S. W.; Li, P. H.; Zhang, L. J.; Guan, Y. J.; Butt, K. M.; Wong, K. L.; Chan, K. W.; Lim, W.; Shortridge, K. F.; Yuen, K. Y.; Peiris, J. S. M.; Poon, L. L. M. Isolation and Characterization of Viruses Related to the SARS Coronavirus from Animals in Southern China. *Science* **2003**, *302* (5643), 276–278. https://doi.org/10.1126/science.1087139.

(33)Cui, J.; Li, F.; Shi, Z.-L. Origin and Evolution of Pathogenic Coronaviruses. *Nat Rev Microbiol* **2019**, *17* (3), 181–192. https://doi.org/10.1038/s41579-018-0118-9.

(34)Omrani, A. S.; Shalhoub, S. Middle East Respiratory Syndrome Coronavirus (MERS-CoV): What Lessons Can We Learn? *J Hosp Infect* **2015**, *91* (3), 188–196. https://doi.org/10.1016/j.jhin.2015.08.002.

(35)Dudas, G.; Carvalho, L. M.; Rambaut, A.; Bedford, T. MERS-CoV Spillover at the Camel-Human Interface. *Elife* **2018**, *7*, e31257. https://doi.org/10.7554/eLife.31257.

(36)Zaki, A. M.; Van Boheemen, S.; Bestebroer, T. M.; Osterhaus, A. D. M. E.; Fouchier, R. A. M. Isolation of a Novel Coronavirus from a Man with Pneumonia in Saudi Arabia. *N Engl J Med* **2012**, *367* (19), 1814–1820. https://doi.org/10.1056/NEJMoa1211721.

(37)Lau, S. K. P.; Li, K. S. M.; Tsang, A. K. L.; Lam, C. S. F.; Ahmed, S.; Chen, H.; Chan, K.-H.; Woo, P. C. Y.; Yuen, K.-Y. Genetic Characterization of Betacoronavirus Lineage C Viruses in Bats Reveals Marked Sequence Divergence in the Spike Protein of Pipistrellus Bat Coronavirus HKU5 in Japanese Pipistrelle: Implications for the Origin of the Novel Middle East Respiratory Syndrome Coronavirus. *J Virol* **2013**, *87* (15), 8638–8650. https://doi.org/10.1128/JVI.01055-13.

(38)Corman, V. M.; Muth, D.; Niemeyer, D.; Drosten, C. Hosts and Sources of Endemic Human Coronaviruses. *Adv Virus Res* **2018**, *100*, 163–188. https://doi.org/10.1016/bs.aivir.2018.01.001.

(39)Wu, A.; Peng, Y.; Huang, B.; Ding, X.; Wang, X.; Niu, P.; Meng, J.; Zhu, Z.; Zhang, Z.; Wang, J.; Sheng, J.; Quan, L.; Xia, Z.; Tan, W.; Cheng, G.; Jiang, T. Genome Composition and Divergence of the Novel Coronavirus (2019-nCoV) Originating in China. *Cell Host & Microbe* **2020**, *27* (3), 325–328. https://doi.org/10.1016/j.chom.2020.02.001.

(40)Kim, D.; Lee, J.-Y.; Yang, J.-S.; Kim, J. W.; Kim, V. N.; Chang, H. The Architecture of SARS-CoV-2 Transcriptome. *Cell* **2020**, *181* (4), 914-921.e10. https://doi.org/10.1016/j.cell.2020.04.011.

(41)Gorbalenya, A. E.; Enjuanes, L.; Ziebuhr, J.; Snijder, E. J. Nidovirales: Evolving the Largest RNA Virus Genome. *Virus Res* **2006**, *117* (1), 17–37. https://doi.org/10.1016/j.virusres.2006.01.017.

(42)Jungreis, I.; Sealfon, R.; Kellis, M. SARS-CoV-2 Gene Content and COVID-19 Mutation Impact by Comparing 44 Sarbecovirus Genomes. *Res Sq* October 1, 2020. https://doi.org/10.21203/rs.3.rs-80345/v1.

(43)Wu, F.; Zhao, S.; Yu, B.; Chen, Y.-M.; Wang, W.; Song, Z.-G.; Hu, Y.; Tao, Z.-W.; Tian, J.-H.; Pei, Y.-Y.; Yuan, M.-L.; Zhang, Y.-L.; Dai, F.-H.; Liu, Y.; Wang, Q.-M.; Zheng, J.-J.; Xu, L.; Holmes, E. C.; Zhang, Y.-Z. A New Coronavirus Associated with Human Respiratory Disease in China. *Nature* **2020**, *579* (7798), 265–269. https://doi.org/10.1038/s41586-020-2008-3.

(44)Hoffmann, M.; Kleine-Weber, H.; Pöhlmann, S. A Multibasic Cleavage Site in the Spike Protein of SARS-CoV-2 Is Essential for Infection of Human Lung Cells. *Mol Cell* **2020**, *78* (4), 779-784.e5. https://doi.org/10.1016/j.molcel.2020.04.022.

(45)Shang, J.; Wan, Y.; Luo, C.; Ye, G.; Geng, Q.; Auerbach, A.; Li, F. Cell Entry Mechanisms of SARS-CoV-2. *Proc Natl Acad Sci USA* **2020**, *117* (21), 11727–11734. https://doi.org/10.1073/pnas.2003138117.

(46)Kuba, K.; Imai, Y.; Rao, S.; Gao, H.; Guo, F.; Guan, B.; Huan, Y.; Yang, P.; Zhang, Y.; Deng, W.; Bao, L.; Zhang, B.; Liu, G.; Wang, Z.; Chappell, M.; Liu, Y.; Zheng, D.; Leibbrandt, A.; Wada, T.; Slutsky, A. S.; Liu, D.; Qin, C.; Jiang, C.; Penninger, J. M. A Crucial Role of Angiotensin Converting Enzyme 2 (ACE2) in SARS Coronavirus-Induced Lung Injury. *Nat Med* **2005**, *11* (8), 875–879. https://doi.org/10.1038/nm1267.

(47)Zhao, M.-M.; Yang, W.-L.; Yang, F.-Y.; Zhang, L.; Huang, W.-J.; Hou, W.; Fan, C.-F.; Jin, R.-H.; Feng, Y.-M.; Wang, Y.-C.; Yang, J.-K. Cathepsin L Plays a Key Role in SARS-CoV-2 Infection in Humans and Humanized Mice and Is a Promising Target for New Drug Development. *Signal Transduct Target Ther* **2021**, *6* (1), 134. https://doi.org/10.1038/s41392-021-00558-8.

(48)Osipiuk, J.; Azizi, S.-A.; Dvorkin, S.; Endres, M.; Jedrzejczak, R.; Jones, K. A.; Kang, S.; Kathayat, R. S.; Kim, Y.; Lisnyak, V. G.; Maki, S. L.; Nicolaescu, V.; Taylor, C. A.; Tesar, C.; Zhang, Y.-A.; Zhou, Z.; Randall, G.; Michalska, K.; Snyder, S. A.; Dickinson, B. C.; Joachimiak,

A. Structure of Papain-like Protease from SARS-CoV-2 and Its Complexes with Non-Covalent Inhibitors. *Nat Commun* **2021**, *12* (1), 743. https://doi.org/10.1038/s41467-021-21060-3.

(49)Jin, Z.; Du, X.; Xu, Y.; Deng, Y.; Liu, M.; Zhao, Y.; Zhang, B.; Li, X.; Zhang, L.; Peng, C.; Duan, Y.; Yu, J.; Wang, L.; Yang, K.; Liu, F.; Jiang, R.; Yang, X.; You, T.; Liu, X.; Yang, X.; Bai, F.; Liu, H.; Liu, X.; Guddat, L. W.; Xu, W.; Xiao, G.; Qin, C.; Shi, Z.; Jiang, H.; Rao, Z.; Yang, H. Structure of Mpro from SARS-CoV-2 and Discovery of Its Inhibitors. *Nature* **2020**, *582* (7811), 289–293. https://doi.org/10.1038/s41586-020-2223-y.

(50)Thoms, M.; Buschauer, R.; Ameismeier, M.; Koepke, L.; Denk, T.; Hirschenberger, M.; Kratzat, H.; Hayn, M.; Mackens-Kiani, T.; Cheng, J.; Straub, J. H.; Stürzel, C. M.; Fröhlich, T.; Berninghausen, O.; Becker, T.; Kirchhoff, F.; Sparrer, K. M. J.; Beckmann, R. Structural Basis for Translational Shutdown and Immune Evasion by the Nsp1 Protein of SARS-CoV-2. *Science* **2020**, *369* (6508), 1249–1255. https://doi.org/10.1126/science.abc8665.

(51)Schubert, K.; Karousis, E. D.; Jomaa, A.; Scaiola, A.; Echeverria, B.; Gurzeler, L.-A.; Leibundgut, M.; Thiel, V.; Mühlemann, O.; Ban, N. SARS-CoV-2 Nsp1 Binds the Ribosomal mRNA Channel to Inhibit Translation. *Nat Struct Mol Biol* **2020**, *27* (10), 959–966. https://doi.org/10.1038/s41594-020-0511-8.

(52)Fisher, T.; Gluck, A.; Narayanan, K.; Kuroda, M.; Nachshon, A.; Hsu, J. C.; Halfmann, P. J.; Yahalom-Ronen, Y.; Tamir, H.; Finkel, Y.; Schwartz, M.; Weiss, S.; Tseng, C.-T. K.; Israely, T.; Paran, N.; Kawaoka, Y.; Makino, S.; Stern-Ginossar, N. Parsing the Role of NSP1 in SARS-CoV-2 Infection. *Cell Rep* **2022**, *39* (11), 110954. https://doi.org/10.1016/j.celrep.2022.110954.

(53)Cortese, M.; Lee, J.-Y.; Cerikan, B.; Neufeldt, C. J.; Oorschot, V. M. J.; Köhrer, S.; Hennies, J.; Schieber, N. L.; Ronchi, P.; Mizzon, G.; Romero-Brey, I.; Santarella-Mellwig, R.; Schorb, M.; Boermel, M.; Mocaer, K.; Beckwith, M. S.; Templin, R. M.; Gross, V.; Pape, C.; Tischer, C.; Frankish, J.; Horvat, N. K.; Laketa, V.; Stanifer, M.; Boulant, S.; Ruggieri, A.; Chatel-Chaix, L.; Schwab, Y.; Bartenschlager, R. Integrative Imaging Reveals SARS-CoV-2-Induced Reshaping of Subcellular Morphologies. *Cell Host Microbe* **2020**, *28* (6), 853-866.e5. https://doi.org/10.1016/j.chom.2020.11.003.

(54)Wolff, G.; Melia, C. E.; Snijder, E. J.; Bárcena, M. Double-Membrane Vesicles as Platforms for Viral Replication. *Trends Microbiol* **2020**, *28* (12), 1022–1033. https://doi.org/10.1016/j.tim.2020.05.009.

(55)Ricciardi, S.; Guarino, A. M.; Giaquinto, L.; Polishchuk, E. V.; Santoro, M.; Di Tullio, G.; Wilson, C.; Panariello, F.; Soares, V. C.; Dias, S. S. G.; Santos, J. C.; Souza, T. M. L.; Fusco, G.;

Viscardi, M.; Brandi, S.; Bozza, P. T.; Polishchuk, R. S.; Venditti, R.; De Matteis, M. A. The Role of NSP6 in the Biogenesis of the SARS-CoV-2 Replication Organelle. *Nature* **2022**, *606* (7915), 761–768. https://doi.org/10.1038/s41586-022-04835-6.

(56)Twu, W.-I.; Lee, J.-Y.; Kim, H.; Prasad, V.; Cerikan, B.; Haselmann, U.; Tabata, K.; Bartenschlager, R. Contribution of Autophagy Machinery Factors to HCV and SARS-CoV-2 Replication Organelle Formation. *Cell Rep* **2021**, *37* (8), 110049. https://doi.org/10.1016/j.celrep.2021.110049.

(57)Tabata, K.; Prasad, V.; Paul, D.; Lee, J.-Y.; Pham, M.-T.; Twu, W.-I.; Neufeldt, C. J.; Cortese, M.; Cerikan, B.; Stahl, Y.; Joecks, S.; Tran, C. S.; Lüchtenborg, C.; V'kovski, P.; Hörmann, K.; Müller, A. C.; Zitzmann, C.; Haselmann, U.; Beneke, J.; Kaderali, L.; Erfle, H.; Thiel, V.; Lohmann, V.; Superti-Furga, G.; Brügger, B.; Bartenschlager, R. Convergent Use of Phosphatidic Acid for Hepatitis C Virus and SARS-CoV-2 Replication Organelle Formation. *Nat Commun* **2021**, *12* (1), 7276. https://doi.org/10.1038/s41467-021-27511-1.

(58)Malone, B.; Urakova, N.; Snijder, E. J.; Campbell, E. A. Structures and Functions of Coronavirus Replication–Transcription Complexes and Their Relevance for SARS-CoV-2 Drug Design. *Nat Rev Mol Cell Biol* **2022**, *23* (1), 21–39. https://doi.org/10.1038/s41580-021-00432-z.

(59)Hillen, H. S.; Kokic, G.; Farnung, L.; Dienemann, C.; Tegunov, D.; Cramer, P. Structure of Replicating SARS-CoV-2 Polymerase. *Nature* **2020**, *584* (7819), 154–156. https://doi.org/10.1038/s41586-020-2368-8.

(60)Gao, Y.; Yan, L.; Huang, Y.; Liu, F.; Zhao, Y.; Cao, L.; Wang, T.; Sun, Q.; Ming, Z.; Zhang, L.; Ge, J.; Zheng, L.; Zhang, Y.; Wang, H.; Zhu, Y.; Zhu, C.; Hu, T.; Hua, T.; Zhang, B.; Yang, X.; Li, J.; Yang, H.; Liu, Z.; Xu, W.; Guddat, L. W.; Wang, Q.; Lou, Z.; Rao, Z. Structure of the RNA-Dependent RNA Polymerase from COVID-19 Virus. *Science* **2020**, *368* (6492), 779–782. https://doi.org/10.1126/science.abb7498.

(61)Snijder, E. J.; Decroly, E.; Ziebuhr, J. The Nonstructural Proteins Directing Coronavirus RNA Synthesis and Processing. *Adv Virus Res* **2016**, *96*, 59–126. https://doi.org/10.1016/bs.aivir.2016.08.008.

(62)Mickolajczyk, K. J.; Shelton, P. M. M.; Grasso, M.; Cao, X.; Warrington, S. E.; Aher, A.; Liu, S.; Kapoor, T. M. Force-Dependent Stimulation of RNA Unwinding by SARS-CoV-2 Nsp13 Helicase. *Biophys J* **2021**, *120* (6), 1020–1030. https://doi.org/10.1016/j.bpj.2020.11.2276.

(63)Shannon, A.; Selisko, B.; Le, N.-T.-T.; Huchting, J.; Touret, F.; Piorkowski, G.; Fattorini, V.; Ferron, F.; Decroly, E.; Meier, C.; Coutard, B.; Peersen, O.; Canard, B. Rapid Incorporation of Favipiravir by the Fast and Permissive Viral RNA Polymerase Complex Results in SARS-CoV-2 Lethal Mutagenesis. *Nat Commun* **2020**, *11* (1), 4682. https://doi.org/10.1038/s41467-020-18463-z.

(64)Smith, E. C.; Blanc, H.; Surdel, M. C.; Vignuzzi, M.; Denison, M. R. Coronaviruses Lacking Exoribonuclease Activity Are Susceptible to Lethal Mutagenesis: Evidence for Proofreading and Potential Therapeutics. *PLoS Pathog* **2013**, *9* (8), e1003565. https://doi.org/10.1371/journal.ppat.1003565.

(65)Lin, S.; Chen, H.; Chen, Z.; Yang, F.; Ye, F.; Zheng, Y.; Yang, J.; Lin, X.; Sun, H.; Wang, L.; Wen, A.; Dong, H.; Xiao, Q.; Deng, D.; Cao, Y.; Lu, G. Crystal Structure of SARS-CoV-2 Nsp10 Bound to Nsp14-ExoN Domain Reveals an Exoribonuclease with Both Structural and Functional Integrity. *Nucleic Acids Res* **2021**, *49* (9), 5382–5392. https://doi.org/10.1093/nar/gkab320.

(66)Liu, C.; Shi, W.; Becker, S. T.; Schatz, D. G.; Liu, B.; Yang, Y. Structural Basis of Mismatch Recognition by a SARS-CoV-2 Proofreading Enzyme. *Science* **2021**, *373* (6559), 1142–1146. https://doi.org/10.1126/science.abi9310.

(67)V'kovski, P.; Kratzel, A.; Steiner, S.; Stalder, H.; Thiel, V. Coronavirus Biology and Replication: Implications for SARS-CoV-2. *Nat Rev Microbiol* **2021**, *19* (3), 155–170. https://doi.org/10.1038/s41579-020-00468-6.

(68)Sawicki, S. G.; Sawicki, D. L. Coronaviruses Use Discontinuous Extension for Synthesis of Subgenome-Length Negative Strands. *Adv Exp Med Biol* **1995**, *380*, 499–506. https://doi.org/10.1007/978-1-4615-1899-0_79.

(69)Sola, I.; Almazán, F.; Zúñiga, S.; Enjuanes, L. Continuous and Discontinuous RNA Synthesis in Coronaviruses. *Annu Rev Virol* **2015**, *2* (1), 265–288. https://doi.org/10.1146/annurev-virology-100114-055218.

(70)Di, H.; McIntyre, A. A.; Brinton, M. A. New Insights about the Regulation of Nidovirus Subgenomic mRNA Synthesis. *Virology* **2018**, *517*, 38–43. https://doi.org/10.1016/j.virol.2018.01.026.

(71)Steiner, S.; Kratzel, A.; Barut, G. T.; Lang, R. M.; Aguiar Moreira, E.; Thomann, L.; Kelly, J. N.; Thiel, V. SARS-CoV-2 Biology and Host Interactions. *Nat Rev Microbiol* **2024**, *22* (4), 206–225. https://doi.org/10.1038/s41579-023-01003-z.

(72)Mendonça, L.; Howe, A.; Gilchrist, J. B.; Sheng, Y.; Sun, D.; Knight, M. L.; Zanetti-Domingues, L. C.; Bateman, B.; Krebs, A.-S.; Chen, L.; Radecke, J.; Li, V. D.; Ni, T.; Kounatidis, I.; Koronfel, M. A.; Szynkiewicz, M.; Harkiolaki, M.; Martin-Fernandez, M. L.; James, W.; Zhang, P. Correlative Multi-Scale Cryo-Imaging Unveils SARS-CoV-2 Assembly and Egress. *Nat Commun* **2021**, *12* (1), 4629. https://doi.org/10.1038/s41467-021-24887-y.

(73)Lu, S.; Ye, Q.; Singh, D.; Cao, Y.; Diedrich, J. K.; Yates, J. R.; Villa, E.; Cleveland, D. W.; Corbett, K. D. The SARS-CoV-2 Nucleocapsid Phosphoprotein Forms Mutually Exclusive Condensates with RNA and the Membrane-Associated M Protein. *Nat Commun* **2021**, *12* (1), 502. https://doi.org/10.1038/s41467-020-20768-y.

(74)Scherer, K. M.; Mascheroni, L.; Carnell, G. W.; Wunderlich, L. C. S.; Makarchuk, S.; Brockhoff, M.; Mela, I.; Fernandez-Villegas, A.; Barysevich, M.; Stewart, H.; Suau Sans, M.; George, C. L.; Lamb, J. R.; Kaminski-Schierle, G. S.; Heeney, J. L.; Kaminski, C. F. SARS-CoV-2 Nucleocapsid Protein Adheres to Replication Organelles before Viral Assembly at the Golgi/ERGIC and Lysosome-Mediated Egress. *Sci Adv* **2022**, *8* (1), eabl4895. https://doi.org/10.1126/sciadv.abl4895.

(75)Murigneux, E.; Softic, L.; Aubé, C.; Grandi, C.; Judith, D.; Bruce, J.; Le Gall, M.; Guillonneau, F.; Schmitt, A.; Parissi, V.; Berlioz-Torrent, C.; Meertens, L.; Hansen, M. M. K.; Gallois-Montbrun, S. Proteomic Analysis of SARS-CoV-2 Particles Unveils a Key Role of G3BP Proteins in Viral Assembly. *Nat Commun* **2024**, *15* (1), 640. https://doi.org/10.1038/s41467-024-44958-0.

(76)Miura, K.; Suzuki, Y.; Ishida, K.; Arakawa, M.; Wu, H.; Fujioka, Y.; Emi, A.; Maeda, K.; Hamajima, R.; Nakano, T.; Tenno, T.; Hiroaki, H.; Morita, E. Distinct Motifs in the E Protein Are Required for SARS-CoV-2 Virus Particle Formation and Lysosomal Deacidification in Host Cells. *J Virol* **2023**, *97* (10), e00426-23. https://doi.org/10.1128/jvi.00426-23.

(77)Alsaadi, E. A. J.; Neuman, B. W.; Jones, I. M. Identification of a Membrane Binding Peptide in the Envelope Protein of MHV Coronavirus. *Viruses* **2020**, *12* (9), 1054. https://doi.org/10.3390/v12091054.

(78)Maeda, J.; Maeda, A.; Makino, S. Release of Coronavirus E Protein in Membrane Vesicles from Virus-Infected Cells and E Protein-Expressing Cells. *Virology* **1999**, *263* (2), 265–272. https://doi.org/10.1006/viro.1999.9955.

(79)Wölk, C.; Shen, C.; Hause, G.; Surya, W.; Torres, J.; Harvey, R. D.; Bello, G. Membrane Condensation and Curvature Induced by SARS-CoV-2 Envelope Protein. *Langmuir* **2024**, *40* (5), 2646–2655. https://doi.org/10.1021/acs.langmuir.3c03079.

(80)Ghosh, S.; Dellibovi-Ragheb, T. A.; Kerviel, A.; Pak, E.; Qiu, Q.; Fisher, M.; Takvorian, P. M.; Bleck, C.; Hsu, V. W.; Fehr, A. R.; Perlman, S.; Achar, S. R.; Straus, M. R.; Whittaker, G. R.; De Haan, C. A. M.; Kehrl, J.; Altan-Bonnet, G.; Altan-Bonnet, N. β-Coronaviruses Use Lysosomes for Egress Instead of the Biosynthetic Secretory Pathway. *Cell* **2020**, *183* (6), 1520-1535.e14. https://doi.org/10.1016/j.cell.2020.10.039.

(81)Katiyar, H.; Arduini, A.; Li, Y.; Liang, C. SARS-CoV-2 Assembly: Gaining Infectivity and Beyond. *Viruses* **2024**, *16* (11), 1648. https://doi.org/10.3390/v16111648.

(82)Pu, J.; Schindler, C.; Jia, R.; Jarnik, M.; Backlund, P.; Bonifacino, J. S. BORC, a Multisubunit Complex That Regulates Lysosome Positioning. *Dev Cell* **2015**, *33* (2), 176–188. https://doi.org/10.1016/j.devcel.2015.02.011.

(83)Chen, D.; Zheng, Q.; Sun, L.; Ji, M.; Li, Y.; Deng, H.; Zhang, H. ORF3a of SARS-CoV-2 Promotes Lysosomal Exocytosis-Mediated Viral Egress. *Dev Cell* **2021**, *56* (23), 3250-3263.e5. https://doi.org/10.1016/j.devcel.2021.10.006.

(84)Bouayad, A. Innate Immune Evasion by SARS-CoV -2: Comparison with SARS-CoV. *Rev Med Virol* **2020**, *30* (6), 1–9. https://doi.org/10.1002/rmv.2135.

(85)Walker, A. P.; Fan, H.; Keown, J. R.; Knight, M. L.; Grimes, J. M.; Fodor, E. The SARS-CoV-2 RNA Polymerase Is a Viral RNA Capping Enzyme. *Nucleic Acids Res* **2021**, *49* (22), 13019–13030. https://doi.org/10.1093/nar/gkab1160.

(86)Park, G. J.; Osinski, A.; Hernandez, G.; Eitson, J. L.; Majumdar, A.; Tonelli, M.; Henzler-Wildman, K.; Pawłowski, K.; Chen, Z.; Li, Y.; Schoggins, J. W.; Tagliabracci, V. S. The Mechanism of RNA Capping by SARS-CoV-2. *Nature* **2022**, *609* (7928), 793–800. https://doi.org/10.1038/s41586-022-05185-z.

(87)Banerjee, A. K.; Blanco, M. R.; Bruce, E. A.; Honson, D. D.; Chen, L. M.; Chow, A.; Bhat, P.; Ollikainen, N.; Quinodoz, S. A.; Loney, C.; Thai, J.; Miller, Z. D.; Lin, A. E.; Schmidt, M. M.; Stewart, D. G.; Goldfarb, D.; De Lorenzo, G.; Rihn, S. J.; Voorhees, R. M.; Botten, J. W.; Majumdar, D.; Guttman, M. SARS-CoV-2 Disrupts Splicing, Translation, and Protein Trafficking to Suppress Host Defenses. *Cell* **2020**, *183* (5), 1325-1339.e21. https://doi.org/10.1016/j.cell.2020.10.004.

(88)Hayn, M.; Hirschenberger, M.; Koepke, L.; Nchioua, R.; Straub, J. H.; Klute, S.; Hunszinger, V.; Zech, F.; Prelli Bozzo, C.; Aftab, W.; Christensen, M. H.; Conzelmann, C.; Müller, J. A.; Srinivasachar Badarinarayan, S.; Stürzel, C. M.; Forne, I.; Stenger, S.; Conzelmann, K.-K.; Münch, J.; Schmidt, F. I.; Sauter, D.; Imhof, A.; Kirchhoff, F.; Sparrer, K. M. J. Systematic Functional Analysis of SARS-CoV-2 Proteins Uncovers Viral Innate Immune Antagonists and Remaining Vulnerabilities. *Cell Rep* **2021**, *35* (7), 109126. https://doi.org/10.1016/j.celrep.2021.109126.

(89)Li, Z.-L.; Zhang, H.-L.; Huang, Y.; Huang, J.-H.; Sun, P.; Zhou, N.-N.; Chen, Y.-H.; Mai, J.; Wang, Y.; Yu, Y.; Zhou, L.-H.; Li, X.; Yang, D.; Peng, X.-D.; Feng, G.-K.; Tang, J.; Zhu, X.-F.; Deng, R. Autophagy Deficiency Promotes Triple-Negative Breast Cancer Resistance to T Cell-Mediated Cytotoxicity by Blocking Tenascin-C Degradation. *Nat Commun* **2020**, *11* (1), 3806. https://doi.org/10.1038/s41467-020-17395-y.

(90)Li, J.-Y.; Liao, C.-H.; Wang, Q.; Tan, Y.-J.; Luo, R.; Qiu, Y.; Ge, X.-Y. The ORF6, ORF8 and Nucleocapsid Proteins of SARS-CoV-2 Inhibit Type I Interferon Signaling Pathway. *Virus Research* **2020**, *286*, 198074. https://doi.org/10.1016/j.virusres.2020.198074.

(91)Shemesh, M.; Aktepe, T. E.; Deerain, J. M.; McAuley, J. L.; Audsley, M. D.; David, C. T.; Purcell, D. F. J.; Urin, V.; Hartmann, R.; Moseley, G. W.; Mackenzie, J. M.; Schreiber, G.; Harari, D. SARS-CoV-2 Suppresses IFNβ Production Mediated by NSP1, 5, 6, 15, ORF6 and ORF7b but Does Not Suppress the Effects of Added Interferon. *PLoS Pathog* **2021**, *17* (8), e1009800. https://doi.org/10.1371/journal.ppat.1009800.

(92)Stukalov, A.; Girault, V.; Grass, V.; Karayel, O.; Bergant, V.; Urban, C.; Haas, D. A.; Huang, Y.; Oubraham, L.; Wang, A.; Hamad, M. S.; Piras, A.; Hansen, F. M.; Tanzer, M. C.; Paron, I.; Zinzula, L.; Engleitner, T.; Reinecke, M.; Lavacca, T. M.; Ehmann, R.; Wölfel, R.; Jores, J.; Kuster, B.; Protzer, U.; Rad, R.; Ziebuhr, J.; Thiel, V.; Scaturro, P.; Mann, M.; Pichlmair, A. Multilevel Proteomics Reveals Host Perturbations by SARS-CoV-2 and SARS-CoV. *Nature* **2021**, *594* (7862), 246–252. https://doi.org/10.1038/s41586-021-03493-4.

(93)Vazquez, C.; Swanson, S. E.; Negatu, S. G.; Dittmar, M.; Miller, J.; Ramage, H. R.; Cherry, S.; Jurado, K. A. SARS-CoV-2 Viral Proteins NSP1 and NSP13 Inhibit Interferon Activation through Distinct Mechanisms. *PLoS One* **2021**, *16* (6), e0253089. https://doi.org/10.1371/journal.pone.0253089.

(94)Xia, H.; Cao, Z.; Xie, X.; Zhang, X.; Chen, J. Y.-C.; Wang, H.; Menachery, V. D.; Rajsbaum, R.; Shi, P.-Y. Evasion of Type I Interferon by SARS-CoV-2. *Cell Rep* **2020**, *33* (1), 108234. https://doi.org/10.1016/j.celrep.2020.108234.

(95)Yuen, C.-K.; Lam, J.-Y.; Wong, W.-M.; Mak, L.-F.; Wang, X.; Chu, H.; Cai, J.-P.; Jin, D.-Y.; To, K. K.-W.; Chan, J. F.-W.; Yuen, K.-Y.; Kok, K.-H. SARS-CoV-2 Nsp13, Nsp14, Nsp15 and Orf6 Function as Potent Interferon Antagonists. *Emerg Microbes Infect* **2020**, *9* (1), 1418–1428. https://doi.org/10.1080/22221751.2020.1780953.

(96)Zheng, M.; Karki, R.; Williams, E. P.; Yang, D.; Fitzpatrick, E.; Vogel, P.; Jonsson, C. B.; Kanneganti, T.-D. TLR2 Senses the SARS-CoV-2 Envelope Protein to Produce Inflammatory Cytokines. *Nat Immunol* **2021**, *22* (7), 829–838. https://doi.org/10.1038/s41590-021-00937-x.

(97)Planès, R.; Bert, J.-B.; Tairi, S.; BenMohamed, L.; Bahraoui, E. SARS-CoV-2 Envelope (E) Protein Binds and Activates TLR2 Pathway: A Novel Molecular Target for COVID-19 Interventions. *Viruses* **2022**, *14* (5), 999. https://doi.org/10.3390/v14050999.

(98)Rebendenne, A.; Valadão, A. L. C.; Tauziet, M.; Maarifi, G.; Bonaventure, B.; McKellar, J.; Planès, R.; Nisole, S.; Arnaud-Arnould, M.; Moncorgé, O.; Goujon, C. SARS-CoV-2 Triggers an MDA-5-Dependent Interferon Response Which Is Unable to Control Replication in Lung Epithelial Cells. *J Virol* **2021**, *95* (8), e02415-20, JVI.02415-20. https://doi.org/10.1128/JVI.02415-20.

(99)Yang, D.-M.; Geng, T.-T.; Harrison, A. G.; Wang, P.-H. Differential Roles of RIG-I like Receptors in SARS-CoV-2 Infection. *Military Med Res* **2021**, *8* (1), 49. https://doi.org/10.1186/s40779-021-00340-5.

(100)Yin, X.; Riva, L.; Pu, Y.; Martin-Sancho, L.; Kanamune, J.; Yamamoto, Y.; Sakai, K.; Gotoh, S.; Miorin, L.; De Jesus, P. D.; Yang, C.-C.; Herbert, K. M.; Yoh, S.; Hultquist, J. F.; García-Sastre, A.; Chanda, S. K. MDA5 Governs the Innate Immune Response to SARS-CoV-2 in Lung Epithelial Cells. *Cell Rep* **2021**, *34* (2), 108628. https://doi.org/10.1016/j.celrep.2020.108628.

(101)Sampaio, N. G.; Chauveau, L.; Hertzog, J.; Bridgeman, A.; Fowler, G.; Moonen, J. P.; Dupont, M.; Russell, R. A.; Noerenberg, M.; Rehwinkel, J. The RNA Sensor MDA5 Detects SARS-CoV-2 Infection. *Sci Rep* **2021**, *11* (1), 13638. https://doi.org/10.1038/s41598-021-92940-3.

(102)Anaeigoudari, A.; Mollaei, H. R.; Arababadi, M. K.; Nosratabadi, R. Severe Acute Respiratory Syndrome Coronavirus 2: The Role of the Main Components of the Innate Immune System. *Inflammation* **2021**, *44* (6), 2151–2169. https://doi.org/10.1007/s10753-021-01519-7.

(103)Kasuga, Y.; Zhu, B.; Jang, K.-J.; Yoo, J.-S. Innate Immune Sensing of Coronavirus and Viral Evasion Strategies. *Exp Mol Med* **2021**, *53* (5), 723–736. https://doi.org/10.1038/s12276-021-00602-1.

(104)Schindler, C.; Levy, D. E.; Decker, T. JAK-STAT Signaling: From Interferons to Cytokines. *Journal of Biological Chemistry* **2007**, *282* (28), 20059–20063. https://doi.org/10.1074/jbc.R700016200.

(105)Schoggins, J. W. Interferon-Stimulated Genes: What Do They All Do? *Annu. Rev. Virol.* **2019**, *6* (1), 567–584. https://doi.org/10.1146/annurev-virology-092818-015756.

(106)Sun, L.; Wu, J.; Du, F.; Chen, X.; Chen, Z. J. Cyclic GMP-AMP Synthase Is a Cytosolic DNA Sensor That Activates the Type I Interferon Pathway. *Science* **2013**, *339* (6121), 786–791. https://doi.org/10.1126/science.1232458.

(107)Schoggins, J. W.; MacDuff, D. A.; Imanaka, N.; Gainey, M. D.; Shrestha, B.; Eitson, J. L.; Mar, K. B.; Richardson, R. B.; Ratushny, A. V.; Litvak, V.; Dabelic, R.; Manicassamy, B.; Aitchison, J. D.; Aderem, A.; Elliott, R. M.; García-Sastre, A.; Racaniello, V.; Snijder, E. J.; Yokoyama, W. M.; Diamond, M. S.; Virgin, H. W.; Rice, C. M. Pan-Viral Specificity of IFN-Induced Genes Reveals New Roles for cGAS in Innate Immunity. *Nature* **2014**, *505* (7485), 691–695. https://doi.org/10.1038/nature12862.

(108)Rui, Y.; Su, J.; Shen, S.; Hu, Y.; Huang, D.; Zheng, W.; Lou, M.; Shi, Y.; Wang, M.; Chen, S.; Zhao, N.; Dong, Q.; Cai, Y.; Xu, R.; Zheng, S.; Yu, X.-F. Unique and Complementary Suppression of cGAS-STING and RNA Sensing- Triggered Innate Immune Responses by SARS-CoV-2 Proteins. *Signal Transduct Target Ther* **2021**, *6* (1), 123. https://doi.org/10.1038/s41392-021-00515-5.

(109)Christgen, S.; Kanneganti, T.-D. Inflammasomes and the Fine Line between Defense and Disease. *Curr Opin Immunol* **2020**, *62*, 39–44. https://doi.org/10.1016/j.coi.2019.11.007.

(110)Kelley, N.; Jeltema, D.; Duan, Y.; He, Y. The NLRP3 Inflammasome: An Overview of Mechanisms of Activation and Regulation. *IJMS* **2019**, *20* (13), 3328. https://doi.org/10.3390/ijms20133328.

(111)Campbell, G. R.; To, R. K.; Hanna, J.; Spector, S. A. SARS-CoV-2, SARS-CoV-1, and HIV-1 Derived ssRNA Sequences Activate the NLRP3 Inflammasome in Human Macrophages

through a Non-Classical Pathway. *iScience* **2021**, *24* (4), 102295. https://doi.org/10.1016/j.isci.2021.102295.

(112)Pan, P.; Shen, M.; Yu, Z.; Ge, W.; Chen, K.; Tian, M.; Xiao, F.; Wang, Z.; Wang, J.; Jia, Y.; Wang, W.; Wan, P.; Zhang, J.; Chen, W.; Lei, Z.; Chen, X.; Luo, Z.; Zhang, Q.; Xu, M.; Li, G.; Li, Y.; Wu, J. SARS-CoV-2 N Protein Promotes NLRP3 Inflammasome Activation to Induce Hyperinflammation. *Nat Commun* **2021**, *12* (1), 4664. https://doi.org/10.1038/s41467-021-25015-6.

(113)Xu, H.; Akinyemi, I. A.; Chitre, S. A.; Loeb, J. C.; Lednicky, J. A.; McIntosh, M. T.; Bhaduri-McIntosh, S. SARS-CoV-2 Viroporin Encoded by ORF3a Triggers the NLRP3 Inflammatory Pathway. *Virology* **2022**, *568*, 13–22. https://doi.org/10.1016/j.virol.2022.01.003.

(114)Lei, X.; Dong, X.; Ma, R.; Wang, W.; Xiao, X.; Tian, Z.; Wang, C.; Wang, Y.; Li, L.; Ren, L.; Guo, F.; Zhao, Z.; Zhou, Z.; Xiang, Z.; Wang, J. Activation and Evasion of Type I Interferon Responses by SARS-CoV-2. *Nat Commun* **2020**, *11* (1), 3810. https://doi.org/10.1038/s41467-020-17665-9.

(115)Li, A.; Zhao, K.; Zhang, B.; Hua, R.; Fang, Y.; Jiang, W.; Zhang, J.; Hui, L.; Zheng, Y.; Li, Y.; Zhu, C.; Wang, P.-H.; Peng, K.; Xia, Y. SARS-CoV-2 NSP12 Protein Is Not an Interferon-β Antagonist. *J Virol* **2021**, *95* (17), e00747-21. https://doi.org/10.1128/JVI.00747-21.

(116)Zheng, Y.; Zhuang, M.-W.; Han, L.; Zhang, J.; Nan, M.-L.; Zhan, P.; Kang, D.; Liu, X.; Gao, C.; Wang, P.-H. Severe Acute Respiratory Syndrome Coronavirus 2 (SARS-CoV-2) Membrane (M) Protein Inhibits Type I and III Interferon Production by Targeting RIG-I/MDA-5 Signaling. *Sig Transduct Target Ther* **2020**, *5* (1), 299. https://doi.org/10.1038/s41392-020-00438-7.

(117)Sui, L.; Zhao, Y.; Wang, W.; Wu, P.; Wang, Z.; Yu, Y.; Hou, Z.; Tan, G.; Liu, Q. SARS-CoV-2 Membrane Protein Inhibits Type I Interferon Production Through Ubiquitin-Mediated Degradation of TBK1. *Front. Immunol.* **2021**, *12*, 662989. https://doi.org/10.3389/fimmu.2021.662989.

(118)Loo, Y.-M.; Gale, M. Immune Signaling by RIG-I-like Receptors. *Immunity* **2011**, *34* (5), 680–692. https://doi.org/10.1016/j.immuni.2011.05.003.

(119)Kawai, T.; Akira, S. The Roles of TLRs, RLRs and NLRs in Pathogen Recognition. *Int Immunol* **2009**, *21* (4), 317–337. https://doi.org/10.1093/intimm/dxp017.

(120)Ma, Z.; Ni, G.; Damania, B. Innate Sensing of DNA Virus Genomes. *Annu Rev Virol* **2018**, *5* (1), 341–362. https://doi.org/10.1146/annurev-virology-092917-043244.

(121)Mogensen, T. H. Pathogen Recognition and Inflammatory Signaling in Innate Immune Defenses. *Clin Microbiol Rev* **2009**, *22* (2), 240–273, Table of Contents. https://doi.org/10.1128/CMR.00046-08.

(122)Yan, L.; Ge, J.; Zheng, L.; Zhang, Y.; Gao, Y.; Wang, T.; Huang, Y.; Yang, Y.; Gao, S.; Li, M.; Liu, Z.; Wang, H.; Li, Y.; Chen, Y.; Guddat, L. W.; Wang, Q.; Rao, Z.; Lou, Z. Cryo-EM Structure of an Extended SARS-CoV-2 Replication and Transcription Complex Reveals an Intermediate State in Cap Synthesis. *Cell* **2021**, *184* (1), 184-193.e10. https://doi.org/10.1016/j.cell.2020.11.016.

(123)Frazier, M. N.; Dillard, L. B.; Krahn, J. M.; Perera, L.; Williams, J. G.; Wilson, I. M.; Stewart, Z. D.; Pillon, M. C.; Deterding, L. J.; Borgnia, M. J.; Stanley, R. E. Characterization of SARS2 Nsp15 Nuclease Activity Reveals It's Mad about U. *Nucleic Acids Res* **2021**, *49* (17), 10136–10149. https://doi.org/10.1093/nar/gkab719.

(124)Hackbart, M.; Deng, X.; Baker, S. C. Coronavirus Endoribonuclease Targets Viral Polyuridine Sequences to Evade Activating Host Sensors. *Proc Natl Acad Sci U S A* **2020**, *117* (14), 8094–8103. https://doi.org/10.1073/pnas.1921485117.

(125)Versteeg, G. A.; Bredenbeek, P. J.; van den Worm, S. H. E.; Spaan, W. J. M. Group 2 Coronaviruses Prevent Immediate Early Interferon Induction by Protection of Viral RNA from Host Cell Recognition. *Virology* **2007**, *361* (1), 18–26. https://doi.org/10.1016/j.virol.2007.01.020.

(126)Zhou, H.; Perlman, S. Mouse Hepatitis Virus Does Not Induce Beta Interferon Synthesis and Does Not Inhibit Its Induction by Double-Stranded RNA. *J Virol* **2007**, *81* (2), 568–574. https://doi.org/10.1128/JVI.01512-06.

(127)Chen, D.; Zhang, H. Autophagy in Severe Acute Respiratory Syndrome Coronavirus 2 Infection. *Curr Opin Physiol* **2022**, *29*, 100596. https://doi.org/10.1016/j.cophys.2022.100596.

(128)Levine, B.; Mizushima, N.; Virgin, H. W. Autophagy in Immunity and Inflammation. *Nature* **2011**, *469* (7330), 323–335. https://doi.org/10.1038/nature09782.

(129)Stern-Ginossar, N.; Thompson, S. R.; Mathews, M. B.; Mohr, I. Translational Control in Virus-Infected Cells. *Cold Spring Harb Perspect Biol* **2019**, *11* (3), a033001. https://doi.org/10.1101/cshperspect.a033001.

(130)Finkel, Y.; Mizrahi, O.; Nachshon, A.; Weingarten-Gabbay, S.; Morgenstern, D.; Yahalom-Ronen, Y.; Tamir, H.; Achdout, H.; Stein, D.; Israeli, O.; Beth-Din, A.; Melamed, S.; Weiss, S.;

Israely, T.; Paran, N.; Schwartz, M.; Stern-Ginossar, N. The Coding Capacity of SARS-CoV-2. *Nature* **2021**, *589* (7840), 125–130. https://doi.org/10.1038/s41586-020-2739-1.

(131)Finkel, Y.; Gluck, A.; Nachshon, A.; Winkler, R.; Fisher, T.; Rozman, B.; Mizrahi, O.; Lubelsky, Y.; Zuckerman, B.; Slobodin, B.; Yahalom-Ronen, Y.; Tamir, H.; Ulitsky, I.; Israely, T.; Paran, N.; Schwartz, M.; Stern-Ginossar, N. SARS-CoV-2 Uses a Multipronged Strategy to Impede Host Protein Synthesis. *Nature* **2021**, *594* (7862), 240–245. https://doi.org/10.1038/s41586-021-03610-3.

(132)Lapointe, C. P.; Grosely, R.; Johnson, A. G.; Wang, J.; Fernández, I. S.; Puglisi, J. D. Dynamic Competition between SARS-CoV-2 NSP1 and mRNA on the Human Ribosome Inhibits Translation Initiation. *Proc Natl Acad Sci USA* **2021**, *118* (6), e2017715118. https://doi.org/10.1073/pnas.2017715118.

(133)Yuan, S.; Balaji, S.; Lomakin, I. B.; Xiong, Y. Coronavirus Nsp1: Immune Response Suppression and Protein Expression Inhibition. *Front Microbiol* **2021**, *12*, 752214. https://doi.org/10.3389/fmicb.2021.752214.

(134)Zhang, K.; Miorin, L.; Makio, T.; Dehghan, I.; Gao, S.; Xie, Y.; Zhong, H.; Esparza, M.; Kehrer, T.; Kumar, A.; Hobman, T. C.; Ptak, C.; Gao, B.; Minna, J. D.; Chen, Z.; García-Sastre, A.; Ren, Y.; Wozniak, R. W.; Fontoura, B. M. A. Nsp1 Protein of SARS-CoV-2 Disrupts the mRNA Export Machinery to Inhibit Host Gene Expression. *Sci Adv* **2021**, *7* (6), eabe7386. https://doi.org/10.1126/sciadv.abe7386.

(135)Narayanan, K.; Huang, C.; Lokugamage, K.; Kamitani, W.; Ikegami, T.; Tseng, C.-T. K.; Makino, S. Severe Acute Respiratory Syndrome Coronavirus Nsp1 Suppresses Host Gene Expression, Including That of Type I Interferon, in Infected Cells. *J Virol* **2008**, *82* (9), 4471–4479. https://doi.org/10.1128/JVI.02472-07.

(136)Pinet, L.; Assrir, N.; Van Heijenoort, C. Expanding the Disorder-Function Paradigm in the C-Terminal Tails of Erbbs. *Biomolecules* **2021**, *11* (11), 1690. https://doi.org/10.3390/biom11111690.

(137)Wright, P. E.; Dyson, H. J. Intrinsically Unstructured Proteins: Re-Assessing the Protein Structure-Function Paradigm. *J Mol Biol* **1999**, *293* (2), 321–331. https://doi.org/10.1006/jmbi.1999.3110.

(138)Dyson, H. J.; Wright, P. E. Intrinsically Unstructured Proteins and Their Functions. *Nat Rev Mol Cell Biol* **2005**, *6* (3), 197–208. https://doi.org/10.1038/nrm1589.

(139)Uversky, V. N. What Does It Mean to Be Natively Unfolded? *European Journal of Biochemistry* **2002**, *269* (1), 2–12. https://doi.org/10.1046/j.0014-2956.2001.02649.x.

(140)Dunker, A. K.; Lawson, J. D.; Brown, C. J.; Williams, R. M.; Romero, P.; Oh, J. S.; Oldfield, C. J.; Campen, A. M.; Ratliff, C. M.; Hipps, K. W.; Ausio, J.; Nissen, M. S.; Reeves, R.; Kang, C.; Kissinger, C. R.; Bailey, R. W.; Griswold, M. D.; Chiu, W.; Garner, E. C.; Obradovic, Z. Intrinsically Disordered Protein. *J Mol Graph Model* **2001**, *19* (1), 26–59. https://doi.org/10.1016/S1093-3263(00)00138-8.

(141)Radivojac, P.; Iakoucheva, L. M.; Oldfield, C. J.; Obradovic, Z.; Uversky, V. N.; Dunker, A. K. Intrinsic Disorder and Functional Proteomics. *Biophys J* **2007**, *92* (5), 1439–1456. https://doi.org/10.1529/biophysj.106.094045.

(142)Williams, R. M.; Obradovic, Z.; Mathura, V.; Braun, W.; Garner, E. C.; Young, J.; Takayama, S.; Brown, C. J.; Dunker, A. K. The Protein Non-folding Probkem: Amino Acid Determinatnts of Intrinsic Order and Disorder. In *Biocomputing 2001*; WORLD SCIENTIFIC: Mauna Lani, Hawaii, 2000; pp 89–100. https://doi.org/10.1142/9789814447362_0010.

(143)Beveridge, R.; Migas, L. G.; Das, R. K.; Pappu, R. V.; Kriwacki, R. W.; Barran, P. E. Ion Mobility Mass Spectrometry Uncovers the Impact of the Patterning of Oppositely Charged Residues on the Conformational Distributions of Intrinsically Disordered Proteins. *J Am Chem Soc* **2019**, *141* (12), 4908–4918. https://doi.org/10.1021/jacs.8b13483.

(144)Martin, E. W.; Holehouse, A. S.; Peran, I.; Farag, M.; Incicco, J. J.; Bremer, A.; Grace, C. R.; Soranno, A.; Pappu, R. V.; Mittag, T. Valence and Patterning of Aromatic Residues Determine the Phase Behavior of Prion-like Domains. *Science* **2020**, *367* (6478), 694–699. https://doi.org/10.1126/science.aaw8653.

(145)Martin, E. W.; Holehouse, A. S.; Grace, C. R.; Hughes, A.; Pappu, R. V.; Mittag, T. Sequence Determinants of the Conformational Properties of an Intrinsically Disordered Protein Prior to and upon Multisite Phosphorylation. *J Am Chem Soc* **2016**, *138* (47), 15323–15335. https://doi.org/10.1021/jacs.6b10272.

(146)Strodel, B. Energy Landscapes of Protein Aggregation and Conformation Switching in Intrinsically Disordered Proteins. *J Mol Biol* **2021**, *433* (20), 167182. https://doi.org/10.1016/j.jmb.2021.167182.

(147)Kriwacki, R. W.; Hengst, L.; Tennant, L.; Reed, S. I.; Wright, P. E. Structural Studies of p21Waf1/Cip1/Sdi1 in the Free and Cdk2-Bound State: Conformational Disorder Mediates

Binding Diversity. *Proc Natl Acad Sci U.S.A.* **1996**, *93* (21), 11504–11509. https://doi.org/10.1073/pnas.93.21.11504.

(148)Uversky, V. N. Analyzing IDPs in Interactomes. In *Intrinsically Disordered Proteins*; Kragelund, B. B., Skriver, K., Eds.; Methods in Molecular Biology; Springer US: New York, NY, 2020; Vol. 2141, pp 895–945. https://doi.org/10.1007/978-1-0716-0524-0_46.

(149)Spolar, R. S.; Record, M. T. Coupling of Local Folding to Site-Specific Binding of Proteins to DNA. *Science* **1994**, *263* (5148), 777–784. https://doi.org/10.1126/science.8303294.

(150)Dyson, H. J.; Wright, P. E. Coupling of Folding and Binding for Unstructured Proteins. *Curr Opin Struct Biol* **2002**, *12* (1), 54–60. https://doi.org/10.1016/S0959-440X(02)00289-0.

(151)Fuxreiter, M.; Simon, I.; Friedrich, P.; Tompa, P. Preformed Structural Elements Feature in Partner Recognition by Intrinsically Unstructured Proteins. *J Mol Biol* **2004**, *338* (5), 1015–1026. https://doi.org/10.1016/j.jmb.2004.03.017.

(152)Bertagna, A.; Toptygin, D.; Brand, L.; Barrick, D. The Effects of Conformational Heterogeneity on the Binding of the Notch Intracellular Domain to Effector Proteins: A Case of Biologically Tuned Disorder. *Biochem Soc Trans* **2008**, *36* (2), 157–166. https://doi.org/10.1042/BST0360157.

(153)Wang, Y.; Fisher, J. C.; Mathew, R.; Ou, L.; Otieno, S.; Sublet, J.; Xiao, L.; Chen, J.; Roussel, M. F.; Kriwacki, R. W. Intrinsic Disorder Mediates the Diverse Regulatory Functions of the Cdk Inhibitor P21. *Nat Chem Biol* **2011**, *7* (4), 214–221. https://doi.org/10.1038/nchembio.536.

(154)Mittag, T.; Marsh, J.; Grishaev, A.; Orlicky, S.; Lin, H.; Sicheri, F.; Tyers, M.; Forman-Kay, J. D. Structure/Function Implications in a Dynamic Complex of the Intrinsically Disordered Sic1 with the Cdc4 Subunit of an SCF Ubiquitin Ligase. *Structure* **2010**, *18* (4), 494–506. https://doi.org/10.1016/j.str.2010.01.020.

(155)Tompa, P. The Interplay between Structure and Function in Intrinsically Unstructured Proteins. *FEBS Letters* **2005**, *579* (15), 3346–3354. https://doi.org/10.1016/j.febslet.2005.03.072.

(156)Trivedi, R.; Nagarajaram, H. A. Intrinsically Disordered Proteins: An Overview. *Int J Mol Sci* **2022**, *23* (22), 14050. https://doi.org/10.3390/ijms232214050.

(157)Piovesan, D.; Tosatto, S. C. E. Mobi 2.0: An Improved Method to Define Intrinsic Disorder, Mobility and Linear Binding Regions in Protein Structures. *Bioinformatics* **2018**, *34* (1), 122–123. https://doi.org/10.1093/bioinformatics/btx592.

(158)Vymětal, J.; Vondrášek, J.; Hlouchová, K. Sequence Versus Composition: What Prescribes IDP Biophysical Properties? *Entropy* **2019**, *21* (7), 654. https://doi.org/10.3390/e21070654.

(159)Cornish, J.; Chamberlain, S. G.; Owen, D.; Mott, H. R. Intrinsically Disordered Proteins and Membranes: A Marriage of Convenience for Cell Signalling? *Biochem Soc Trans* **2020**, *48* (6), 2669–2689. https://doi.org/10.1042/BST20200467.

(160)Schroeder, R.; Barta, A.; Semrad, K. Strategies for RNA Folding and Assembly. *Nat Rev Mol Cell Biol* **2004**, *5* (11), 908–919. https://doi.org/10.1038/nrm1497.

(161)Young, J. C.; Agashe, V. R.; Siegers, K.; Hartl, F. U. Pathways of Chaperone-Mediated Protein Folding in the Cytosol. *Nat Rev Mol Cell Biol* **2004**, *5* (10), 781–791. https://doi.org/10.1038/nrm1492.

(162)Kovacs, D.; Tompa, P. Diverse Functional Manifestations of Intrinsic Structural Disorder in Molecular Chaperones. *Biochem Soc Trans* **2012**, *40* (5), 963–968. https://doi.org/10.1042/BST20120108.

(163)Sugase, K.; Dyson, H. J.; Wright, P. E. Mechanism of Coupled Folding and Binding of an Intrinsically Disordered Protein. *Nature* **2007**, *447* (7147), 1021–1025. https://doi.org/10.1038/nature05858.

(164)Mughal, F.; Caetano-Anollés, G. Evolution of Intrinsic Disorder in the Structural Domains of Viral and Cellular Proteomes. *Sci Rep* **2025**, *15* (1), 2878. https://doi.org/10.1038/s41598-025-86045-4.

Chapter 2

METHODS

Biological Samples and Techniques

Peptides

Multiple synthetic Nsp1-CT peptides were used throughout this work, and all of them were obtained through Genscript Biotech Corporation. All the peptides were prepared with N-terminal acetylation (Ac-). The following peptides were used in these studies:

Nsp1-CT_{33}: Ac- ELGTDPYEDFQENWNTKHSSGVTRELMRELNGG

Nsp1-CT_{33} Y154(YNO_2): ELGTDP(YNO_2)EDFQENWNTKHSSGVTRELMRELNGG

Nsp1-CT_{33} H165A: Ac- ELGTDPYEDFQENWNTKASSGVTRELMRELNGG

Nsp1-CT_{10}: Ac-ENWNTKHSSG.

Protein Expression and Purification

Multiple medias were used in the process of protein expression. Below are the medias and their formulations. Bacto-tryptone and bacto-yeast were purchased from ThermoFisher Scientific Gibco.

SOC Media: To a flask add 20g bacto-tryptone, 5g bacto-yeast, 0.5g NaCl, 10 mL KCl (250mM), 0.2mL NaOH (5M) then adjust the volume to 1L and autoclave. After autoclaving add 5mL sterile $MgCl_2$ (2M). Once it has cooled add 20 mL of a sterile 1 M solution of glucose.

LB Media: To prepare the LB media, add 10g of bacto-tryptone, 5g of bacto-yeast, and 10g of NaCl to a flask along with 1L of MilliQ- water. Adjust the pH to 7 using 5M NaOH. Sterilize by autoclaving before use.

2XYT Media: To prepare the media, add 8 g of Bacto- tryptone, 5 g of Bacto- yeast extract, and 2.5 g of NaCl to 500 mL of Milli-Q water in a flask. Adjust the pH to 7.0 using 5 M NaOH. Sterilize the solution by autoclaving.

LB Agar Plates with antibiotic resistance: To a flask add 4g tryptone, 2g yeast, 4g NaCl, 6g Agar, 80μL NaOH (5M), and adjust with water to 400mL. Autoclave. Once the solution is approximately 55°C antibiotics can be added. Pipet 25mL into each plate, allow to cool and store at 4°C. Antibiotic used was Kanamycin (preparation for antibiotic samples is below).

M9 Minimal Media Preparation for ^{15}N Labeling: To prepare the minimal media, a 5X M9 salt solution was first prepared by dissolving 64 g of $Na_2HPO_4 \cdot 7H_2O$, 15 g of KH_2PO_4, 2.5 g of NaCl, and 5.0 g of NH_4Cl in 1 L of Milli-Q water. For ^{15}N labeling experiments, NH_4Cl was substituted with ^{15}N-labeled ammonium chloride (Cambridge Isotope Laboratories Inc., Item No. NLM-467-5). The salt solution was sterilized by autoclaving. Separately, the following components were prepared and sterilized by autoclaving: 1 M $MgSO_4$ solution ,1 M $CaCl_2$ solution, and a 40% (w/v) glucose solution. To prepare 1 L of final minimal media, the following were combined: 200 mL of the 5X M9 salt solution, 800 mL of Milli-Q water, 2 mL of 1 M $MgSO_4$, 0.1 mL of 1 M $CaCl_2$, and 10 mL of the 40% glucose solution.

Antibiotic preparation: Kanamycin antibiotic stocks were prepared at a concentration of 100 mg/mL to achieve a final working concentration of 100 µg/mL when added to media.

Plasmid details: The plasmid for the wild type protein was obtained from Genscript as powder. The plasmid (0.3µg) was dissolved in 50µL of TE buffer (10mM Tris-HCl, 1mM EDTA pH 8.0). From the solution 0.5µL was used for transformations.

His6-Nsp1 pET-24a(+) plasmid sequence:

TGGCGAATGGGACGCGCCCTGTAGCGGCGCATTAAGCGCGGCGGGTGTGGTG
GTTACGCGCAGCGTGACCGCTACACTTGCCAGCGCCCTAGCGCCCGCTCCTTTC
GCTTTCTTCCCTTCCTTTCTCGCCACGTTCGCCGGCTTTCCCCGTCAAGCTCTAA
ATCGGGGGCTCCCTTTAGGGTTCCGATTTAGTGCTTTACGGCACCTCGACCCCA
AAAAACTTGATTAGGGTGATGGTTCACGTAGTGGGCCATCGCCCTGATAGACG
GTTTTTCGCCCTTTGACGTTGGAGTCCACGTTCTTTAATAGTGGACTCTTGTTCC
AAACTGGAACAACACTCAACCCTATCTCGGTCTATTCTTTTGATTTATAAGGGAT
TTTGCCGATTTCGGCCTATTGGTTAAAAAATGAGCTGATTTAACAAAAATTTAA
CGCGAATTTTAACAAAATATTAACGTTTACAATTTCAGGTGGCACTTTTCGGGG

AAATGTGCGCGGAACCCCTATTTGTTTATTTTTCTAAATACATTCAAATATGTAT
CCGCTCATGAATTAATTCTTAGAAAAACTCATCGAGCATCAAATGAAACTGCAA
TTTATTCATATCAGGATTATCAATACCATATTTTTGAAAAAGCCGTTTCTGTAAT
GAAGGAGAAAACTCACCGAGGCAGTTCCATAGGATGGCAAGATCCTGGTATCG
GTCTGCGATTCCGACTCGTCCAACATCAATACAACCTATTAATTTCCCCTCGTCA
AAAATAAGGTTATCAAGTGAGAAATCACCATGAGTGACGACTGAATCCGGTGA
GAATGGCAAAAGTTTATGCATTTCTTTCCAGACTTGTTCAACAGGCCAGCCATT
ACGCTCGTCATCAAAATCACTCGCATCAACCAAACCGTTATTCATTCGTGATTGC
GCCTGAGCGAGACGAAATACGCGATCGCTGTTAAAAGGACAATTACAAACAGG
AATCGAATGCAACCGGCGCAGGAACACTGCCAGCGCATCAACAATATTTTCACC
TGAATCAGGATATTCTTCTAATACCTGGAATGCTGTTTTCCCGGGGATCGCAGT
GGTGAGTAACCATGCATCATCAGGAGTACGGATAAAATGCTTGATGGTCGGAA
GAGGCATAAATTCCGTCAGCCAGTTTAGTCTGACCATCTCATCTGTAACATCATT
GGCAACGCTACCTTTGCCATGTTTCAGAAACAACTCTGGCGCATCGGGCTTCCC
ATACAATCGATAGATTGTCGCACCTGATTGCCCGACATTATCGCGAGCCCATTT
ATACCCATATAAATCAGCATCCATGTTGGAATTTAATCGCGGCCTAGAGCAAGA
CGTTTCCCGTTGAATATGGCTCATAACACCCCTTGTATTACTGTTTATGTAAGCA
GACAGTTTTATTGTTCATGACCAAAATCCCTTAACGTGAGTTTTCGTTCCACTGA
GCGTCAGACCCCGTAGAAAAGATCAAAGGATCTTCTTGAGATCCTTTTTTTCTG
CGCGTAATCTGCTGCTTGCAAACAAAAAAACCACCGCTACCAGCGGTGGTTTGT
TTGCCGGATCAAGAGCTACCAACTCTTTTTCCGAAGGTAACTGGCTTCAGCAGA
GCGCAGATACCAAATACTGTCCTTCTAGTGTAGCCGTAGTTAGGCCACCACTTC
AAGAACTCTGTAGCACCGCCTACATACCTCGCTCTGCTAATCCTGTTACCAGTG
GCTGCTGCCAGTGGCGATAAGTCGTGTCTTACCGGGTTGGACTCAAGACGATA
GTTACCGGATAAGGCGCAGCGGTCGGGCTGAACGGGGGGTTCGTGCACACAG
CCCAGCTTGGAGCGAACGACCTACACCGAACTGAGATACCTACAGCGTGAGCT
ATGAGAAAGCGCCACGCTTCCCGAAGGGAGAAAGGCGGACAGGTATCCGGTA
AGCGGCAGGGTCGGAACAGGAGAGCGCACGAGGGAGCTTCCAGGGGGAAAC
GCCTGGTATCTTTATAGTCCTGTCGGGTTTCGCCACCTCTGACTTGAGCGTCGA
TTTTTGTGATGCTCGTCAGGGGGGCGGAGCCTATGGAAAAACGCCAGCAACGC
GGCCTTTTTACGGTTCCTGGCCTTTTGCTGGCCTTTTGCTCACATGTTCTTTCCT
GCGTTATCCCCTGATTCTGTGGATAACCGTATTACCGCCTTTGAGTGAGCTGAT

ACCGCTCGCCGCAGCCGAACGACCGAGCGCAGCGAGTCAGTGAGCGAGGAAG
CGGAAGAGCGCCTGATGCGGTATTTTCTCCTTACGCATCTGTGCGGTATTTCAC
ACCGCATATATGGTGCACTCTCAGTACAATCTGCTCTGATGCCGCATAGTTAAG
CCAGTATACACTCCGCTATCGCTACGTGACTGGGTCATGGCTGCGCCCCGACAC
CCGCCAACACCCGCTGACGCGCCCTGACGGGCTTGTCTGCTCCCGGCATCCGCT
TACAGACAAGCTGTGACCGTCTCCGGGAGCTGCATGTGTCAGAGGTTTTCACC
GTCATCACCGAAACGCGCGAGGCAGCTGCGGTAAAGCTCATCAGCGTGGTCGT
GAAGCGATTCACAGATGTCTGCCTGTTCATCCGCGTCCAGCTCGTTGAGTTTCT
CCAGAAGCGTTAATGTCTGGCTTCTGATAAAGCGGGCCATGTTAAGGGCGGTT
TTTTCCTGTTTGGTCACTGATGCCTCCGTGTAAGGGGGATTTCTGTTCATGGGG
GTAATGATACCGATGAAACGAGAGAGGATGCTCACGATACGGGTTACTGATGA
TGAACATGCCCGGTTACTGGAACGTTGTGAGGGTAAACAACTGGCGGTATGG
ATGCGGCGGGACCAGAGAAAAATCACTCAGGGTCAATGCCAGCGCTTCGTTAA
TACAGATGTAGGTGTTCCACAGGGTAGCCAGCAGCATCCTGCGATGCAGATCC
GGAACATAATGGTGCAGGGCGCTGACTTCCGCGTTTCCAGACTTTACGAAACA
CGGAAACCGAAGACCATTCATGTTGTTGCTCAGGTCGCAGACGTTTTGCAGCA
GCAGTCGCTTCACGTTCGCTCGCGTATCGGTGATTCATTCTGCTAACCAGTAAG
GCAACCCCGCCAGCCTAGCCGGGTCCTCAACGACAGGAGCACGATCATGCGCA
CCCGTGGGGCCGCCATGCCGGCGATAATGGCCTGCTTCTCGCCGAAACGTTTG
GTGGCGGGACCAGTGACGAAGGCTTGAGCGAGGGCGTGCAAGATTCCGAATA
CCGCAAGCGACAGGCCGATCATCGTCGCGCTCCAGCGAAAGCGGTCCTCGCCG
AAAATGACCCAGAGCGCTGCCGGCACCTGTCCTACGAGTTGCATGATAAAGAA
GACAGTCATAAGTGCGGCGACGATAGTCATGCCCCGCGCCCACCGGAAGGAGC
TGACTGGGTTGAAGGCTCTCAAGGGCATCGGTCGAGATCCCGGTGCCTAATGA
GTGAGCTAACTTACATTAATTGCGTTGCGCTCACTGCCCGCTTTCCAGTCGGGA
AACCTGTCGTGCCAGCTGCATTAATGAATCGGCCAACGCGCGGGGAGAGGCG
GTTTGCGTATTGGGCGCCAGGGTGGTTTTTCTTTTCACCAGTGAGACGGGCAA
CAGCTGATTGCCCTTCACCGCCTGGCCCTGAGAGAGTTGCAGCAAGCGGTCCA
CGCTGGTTTGCCCCAGCAGGCGAAAATCCTGTTTGATGGTGGTTAACGGCGGG
ATATAACATGAGCTGTCTTCGGTATCGTCGTATCCCACTACCGAGATATCCGCA
CCAACGCGCAGCCCGGACTCGGTAATGGCGCGCATTGCGCCCAGCGCCATCTG
ATCGTTGGCAACCAGCATCGCAGTGGGAACGATGCCCTCATTCAGCATTTGCAT

GGTTTGTTGAAAACCGGACATGGCACTCCAGTCGCCTTCCCGTTCCGCTATCGG
CTGAATTTGATTGCGAGTGAGATATTTATGCCAGCCAGCCAGACGCAGACGCG
CCGAGACAGAACTTAATGGGCCCGCTAACAGCGCGATTTGCTGGTGACCCAAT
GCGACCAGATGCTCCACGCCCAGTCGCGTACCGTCTTCATGGGAGAAAATAAT
ACTGTTGATGGGTGTCTGGTCAGAGACATCAAGAAATAACGCCGGAACATTAG
TGCAGGCAGCTTCCACAGCAATGGCATCCTGGTCATCCAGCGGATAGTTAATG
ATCAGCCCACTGACGCGTTGCGCGAGAAGATTGTGCACCGCCGCTTTACAGGC
TTCGACGCCGCTTCGTTCTACCATCGACACCACCACGCTGGCACCCAGTTGATC
GGCGCGAGATTTAATCGCCGCGACAATTTGCGACGGCGCGTGCAGGGCCAGA
CTGGAGGTGGCAACGCCAATCAGCAACGACTGTTTGCCCGCCAGTTGTTGTGC
CACGCGGTTGGGAATGTAATTCAGCTCCGCCATCGCCGCTTCCACTTTTTCCCG
CGTTTTCGCAGAAACGTGGCTGGCCTGGTTCACCACGCGGGAAACGGTCTGAT
AAGAGACACCGGCATACTCTGCGACATCGTATAACGTTACTGGTTTCACATTCA
CCACCCTGAATTGACTCTCTTCCGGGCGCTATCATGCCATACCGCGAAAGGTTT
TGCGCCATTCGATGGTGTCCGGGATCTCGACGCTCTCCCTTATGCGACTCCTGC
ATTAGGAAGCAGCCCAGTAGTAGGTTGAGGCCGTTGAGCACCGCCGCCGCAA
GGAATGGTGCATGCAAGGAGATGGCGCCCAACAGTCCCCCGGCCACGGGGCC
TGCCACCATACCCACGCCGAAACAAGCGCTCATGAGCCCGAAGTGGCGAGCCC
GATCTTCCCCATCGGTGATGTCGGCGATATAGGCGCCAGCAACCGCACCTGTG
GCGCCGGTGATGCCGGCCACGATGCGTCCGGCGTAGAGGATCGAGATCTCGA
TCCCGCGAAATTAATACGACTCACTATAGGGGAATTGTGAGCGGATAACAATTC
CCCTCTAGAAATAATTTTGTTTAACTTTAAGAAGGAGATATACATATGGGCAGC
AGCCATCATCATCATCATCACAGCAGCGGCGAGAACCTGTACTTCCAGATGGAG
AGCCTTGTCCCTGGTTTCAACGAGAAAACACACGTCCAACTCAGTTTGCCTGTT
TTACAGGTTCGCGACGTGCTCGTACGTGGCTTTGGAGACTCCGTGGAGGAGGT
CTTATCAGAGGCACGTCAACATCTTAAAGATGGCACTTGTGGCTTAGTAGAAGT
TGAAAAAGGCGTTTTGCCTCAACTTGAACAGCCCTATGTGTTCATCAAACGTTC
GGATGCTCGAACTGCACCTCATGGTCATGTTATGGTTGAGCTGGTAGCAGAAC
TCGAAGGCATTCAGTACGGTCGTAGTGGTGAGACACTTGGTGTCCTTGTCCCT
CATGTGGGCGAAATACCAGTGGCTTACCGCAAGGTTCTTCTTCGTAAGAACGG
TAATAAAGGAGCTGGTGGCCATAGTTACGGCGCCGATCTAAAGTCATTTGACT
TAGGCGACGAGCTTGGCACTGATCCTTATGAAGATTTTCAAGAAAACTGGAAC

ACTAAACATAGCAGTGGTGTTACCCGTGAACTCATGCGTGAGCTTAACGGAGG
GTAATAACTCGAGCACCACCACCACCACCACTGAGATCCGGCTGCTAACAAAGC
CCGAAAGGAAGCTGAGTTGGCTGCTGCCACCGCTGAGCAATAACTAGCATAAC
CCCTTGGGGCCTCTAAACGGGTCTTGAGGGGTTTTTTGCTGAAAGGAGGAACT
ATATCCGGAT

Transformation of *E. coli* DH5α with His_6-Nsp1_pET-24a(+) Plasmid: *E. coli* DH5α competent cells were thawed on ice from −80 °C. Simultaneously, 300 µL of SOC medium and an LB agar plate containing kanamycin were warmed to 37 °C. In a sterile 15 mL tube, 100 µL of DH5α cells were combined with 0.5 µL of the His_6-Nsp1_pET-24a(+) plasmid. The tube was gently tapped several times and incubated on ice for 5 minutes. Following this, the cells were heat-shocked at 42 °C for 1 minute and immediately returned to ice for an additional 2 minutes.

After cooling, 200 µL of pre-warmed SOC medium were added to the transformation mixture. The tube was then incubated at 37 °C for 45 minutes with shaking at 250 rpm. Subsequently, 50 µL of the transformed culture were plated onto the pre-warmed LB agar plate containing kanamycin and incubated at 37 °C for 16 hours.

Several resulting colonies were selected for plasmid propagation. Each colony was inoculated into 5 mL of LB medium supplemented with kanamycin and grown for 16 hours at 37 °C. Plasmid DNA was isolated using the QIAprep Spin Miniprep Kit (Qiagen, Cat. No. 27104) following the manufacturer's protocol. Isolated plasmids were submitted to Laragen Inc. for sequencing verification.

To express the His_6-Nsp1_pET-24a(+) plasmid, a second transformation was performed using *E. coli* BL21(DE3) cells. The procedure followed was identical to the one described previously for DH5α cells.

Creation of Glycerol Stocks for Protein Expression: To streamline future protein expression experiments and avoid repeated transformations, glycerol stocks of the transformed BL21(DE3) cells were prepared. A single colony from the transformed LB-kanamycin plate was inoculated into 5 mL of LB medium supplemented with 5 µL of kanamycin. The culture was incubated at 37 °C with shaking at 250 rpm for 16 hours. For long-term storage, 875 µL of the overnight

culture were mixed with 125 µL of sterile 80% glycerol in sterile Eppendorf tubes. The mixture was gently agitated to ensure even distribution before being stored at −80 °C. For subsequent protein expression, a frozen glycerol stock was briefly placed on ice, and a sterile inoculating loop was used to streak a small amount of the culture onto a pre-warmed LB agar plate containing kanamycin. The plate was incubated overnight at 37 °C (16 hours). Stocks were returned to the −80 °C freezer immediately after use, provided they had not thawed.

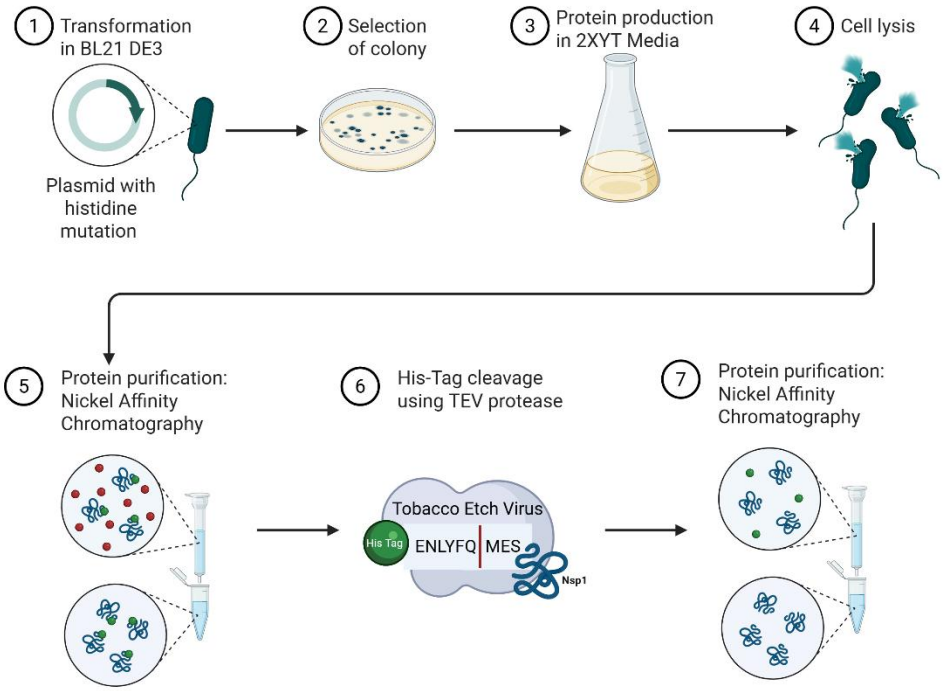

Figure 2.1 Expression and purification methods of full length Nsp1. Figure created with BioRender.com.

Expression of Wild-Type and Mutant Nsp1 Proteins: In order to express the wild type and mutant proteins the following procedure was adapted from Schubert et al.[1] Colonies from the previously transformed *E. coli* BL21(DE3) plates were selected to inoculate small-scale starter cultures.

For each expression, a 5 mL small culture of 2×YT medium supplemented with kanamycin was inoculated with a single colony and incubated at 37 °C with shaking at 180 rpm for approximately 8 hours. After this initial growth phase, the entire small culture was transferred

into 500 mL of pre-warmed 2×YT medium containing kanamycin to initiate the large-scale expression culture.

The large cultures were incubated at 37 °C with shaking at 180 rpm until an optical density at 600 nm (OD_{600}) of 0.6–0.8 was reached (approximately 4 hours). At this point, protein expression was induced by the addition of 1 M IPTG to a final concentration of 0.5 mM. The temperature was then reduced to 18 °C, and the cultures were allowed to express protein overnight (16 hours) with shaking at 180 rpm.

To harvest the expressed cultures, cells were pelleted by centrifugation at 4000 rpm for 10 minutes at 4 °C. The supernatant was discarded. Pellets were either stored at −80 °C for later purification or processed immediately.

Purification of Wild-Type and Mutant Nsp1 Proteins: Cell pellets from expression cultures were resuspended in Buffer A (50 mM HEPES-KOH, pH 7.6, 500 mM KCl, 5 mM $MgCl_2$, 10% [w/v] glycerol, 0.5 mM TCEP). The suspension was sonicated using a probe sonicator for 5 minutes (3 s on, 17 s off, 80% amplitude). Lysozyme, DNase I, RNase A, and protease inhibitors were added, and the lysate was gently stirred at 4 °C for at least 1 hour.

Following lysis, the mixture was centrifuged at 12,000 rpm for 30 minutes at 4 °C. The supernatant was collected, and the pellet was discarded. The clarified lysate was then incubated with Ni-NTA resin overnight at 4 °C for affinity purification of the His_6-tagged Nsp1.

The next day, the resin was transferred to a gravity column. After collecting the flow-through, the resin was washed sequentially with the following: 5 column volumes (CV) of Buffer A, 5 CV of Buffer A containing 20 mM imidazole, 5 CV of Buffer A containing 40 mM imidazole.

His_6-Nsp1 was eluted using 1 CV of Buffer A containing 300 mM imidazole. The eluate was immediately buffer-exchanged back into Buffer A to remove excess imidazole prior to tag removal.

Removal of His_6-Tag: To cleave the His_6-tag, TEV protease from New England Biolabs (Catalog #P8112S) was added according to the manufacturer's instructions. The cleavage mixture was incubated overnight at 4 °C.

Following cleavage, the mixture was incubated once again with Ni-NTA resin overnight at 4 °C. The next day, the flow-through containing the untagged Nsp1 was collected after loading the mixture onto the column.

Protein purity was assessed via SDS-PAGE. If necessary, further purification was performed using size exclusion chromatography. Final samples were concentrated using Amicon Ultra-15 centrifugal filter units (3 kDa molecular weight cutoff), flash-frozen in liquid nitrogen, and stored at −80 °C until use.

^{15}N labelled Nsp1 Expression

The same expression and purification procedures described previously were followed, with the only modification being the use of M9 minimal media instead of 2XYT. Colonies from the BL21 (DE3) transformation plates were used to inoculate small-scale cultures. Specifically, 5 mL of M9 minimal media containing kanamycin were inoculated with a single colony and incubated at 37 °C with shaking at 180 rpm until an OD_{600} of ~0.6 was reached (approximately 2 days).

The entire 5 mL culture was then transferred into a large-scale culture consisting of 500 mL of M9 minimal media with kanamycin. These cultures were incubated under the same conditions (37 °C, 180 rpm) until they reached an OD_{600} of 0.6–0.8, which typically required approximately 4 days.

Once the desired optical density was reached, protein expression was induced by adding 1 M IPTG to a final concentration of 0.5 mM. The temperature was then reduced to 18 °C, and the culture was incubated with shaking (180 rpm) for 22 hours.

Cell harvesting and protein purification were carried out following the same protocol as used for the wild-type and mutant Nsp1 proteins expressed in 2XYT media.

Site Directed Mutagenesis

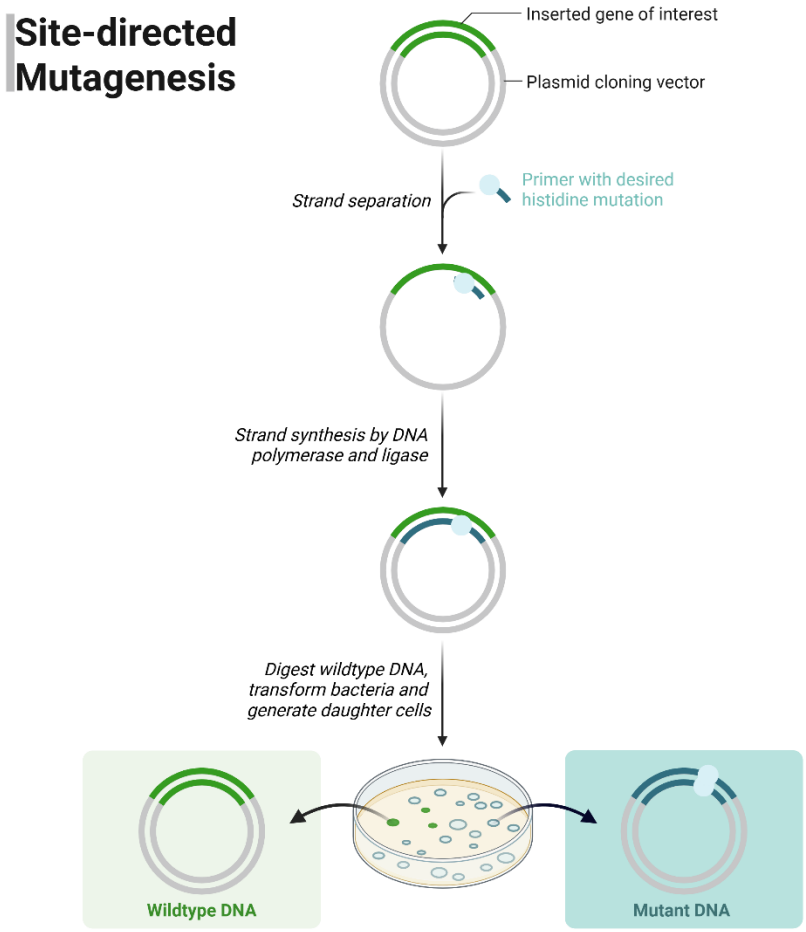

Figure 2.2 Visual representation of site-directed mutagenesis process. Figure created with BioRender.com.

Site-directed mutagenesis was performed to individually mutate each of the seven histidine residues in the Nsp1 protein to generate single-point mutants. Initially, each histidine was mutated to alanine. If the alanine substitution failed to yield soluble or properly expressed protein, alternative substitutions were attempted in the following order: glutamine, then asparagine.

Primers for each mutation were designed accordingly and ordered from Thermo Fisher Scientific. The sequences of the primers used for generating these mutants are listed below:

H165A Primers

Forward: TGGAACACTAAAGCGAGCAGTGGTGTT

Reverse: AACACCACTGCTCGCTTTAGTGTTCCA

H134A Primers

Forward: GGAGCTGGTGGCGCGAGTTACGGCGCC

Reverse: GGCGCCGTAACTCGCGCCACCAGCTCC

H110A Primers

Forward: GTCCTTGTCCCTGCGGTGGGCGAAATA

Reverse: TATTTCGCCCACCGCAGGGACAAGGAC

H83Q Primers

Forward: GCACCTCATGGTCAGGTTATGGTTGAG

Reverse: CTCAACCATAACCTGACCATGAGGTGC

H81N Primers

Forward: CGAACTGCACCTAACGGTCATGTTATG

Reverse: CATAACATGACCGTTAGGTGCAGTTCG

H45A Primers

Forward: GAGGCACGTCAAGCGCTTAAAGATGGC

Reverse: GCCATCTTTAAGCGCTTGACGTGCCTC

H13Q Primer

Forward: AACGAGAAAACACAGGTCCAACTCAGT

Reverse: ACTGAGTTGGACCTGTGTTTTCTCGTT

Mutagenesis was carried out using Thermo Scientific's Phusion Site-Directed Mutagenesis Kit (Catalog No. F541), following the manufacturer's recommended protocol. After transformation, colonies were selected, and plasmids were isolated using the Qiagen QIAprep Spin Miniprep Kit as previously described. The resulting plasmids were then sent to Laragen Inc. for sequencing to confirm the presence of the intended mutations.

***In vitro* translation assay**

Nsp1 is known for shutting down host translation by blocking the 40S ribosomal subunit.[1] To evaluate potential inhibitors, we monitored host translation using a cell-free in vitro translation system derived from HeLa cell lysates.

For these studies, the Thermo Scientific 1-Step Human Coupled IVT Kit – DNA (Catalog No. 88881) was modified. Samples were prepared according to the manufacturer's protocol for GFP expression, followed by the addition of test compounds.

Reagents were added to sterile PCR tubes in the following order using sterile pipette tips: HeLa Lysate (12.5 µL), Accessory Proteins (2.5 µL), Reaction Mix (5 µL), pCFE-GFP DNA (0.5 µg/µL, 2 µL), the test compound or control, and nuclease-free water to a final volume of 25 µL. Samples were gently spun down and then incubated at 30 °C with shaking at 180 rpm for 6 hours.

For Nsp1 inhibition studies, 1 µM of purified Nsp1 was added to each reaction. Inhibitor concentrations varied depending on the compound being tested. Following incubation, each sample was diluted with 75 µL of MOPS buffer (20 mM, pH 7.5), transferred to an NMR tube, and GFP fluorescence was measured.

Fluorescence measurements were performed using a fluorimeter with excitation at 488 nm and emission monitored at 512 nm. A long-pass filter was used to reduce background signal from the excitation source.

Synthetic Chemistry

Synthesis of Copper(II) Iminodiacetate

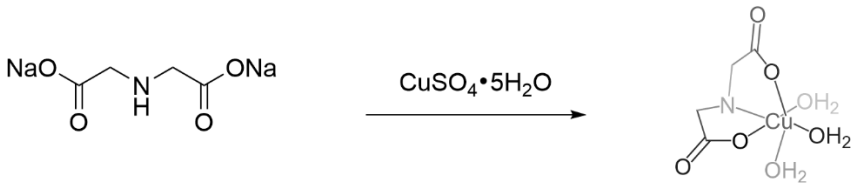

Figure 2.3 Synthetic scheme for Cu(II)IDA.

To make copper(II) iminodiacetate, equimolar amounts of cupric sulfate pentahydrate and sodium iminodiacetate dibasic monohydrate were dissolved in MilliQ water.

Synthesis of Copper(II)Histidinate

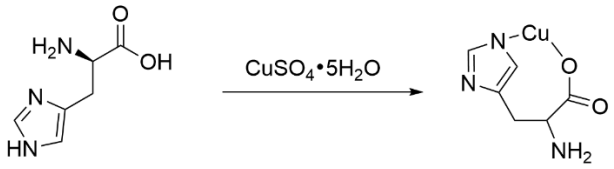

Figure 2.4 Synthetic Scheme for Copper(II) Histidinate.

To make copper(II) iminodiacetate, equimolar amounts of cupric sulfate pentahydrate and L-histidine were dissolved in MilliQ water.

Synthesis of Co(III)EDTA

The preparation was performed following the method described by Bürgisser and Stone[2]. Co(II)EDTA was synthesized by mixing equimolar amounts of cobalt(II) chloride hexahydrate and sodium ethylenediaminetetraacetic acid (EDTA). Hydrogen peroxide was then added to the Co(II)EDTA solution, and the mixture was heated to 90 °C to facilitate oxidation. Upon cooling, a precipitate formed, which was collected and washed with methanol. The resulting deep purple crystals were purified through repeated water–methanol recrystallization and subsequently dried.

Synthesis of $[NaCo(II)(NTA)(H_2O)]_n$

Preparation was repeated according to Zhang et al.[3] A mixture of nitrilotriacetic acid (0.9mmol), Cobalt(II) acetate tetrahydrate (0.5mmol) and water (20mL) was stirred for 30 min. Sodium hydroxide (0.5M) was then added to bring the pH up to 5.5. Three weeks later pink crystals were obtained.

Synthesis of α-$[KCo(III)(NTA)(OH)(H_2O)]\cdot(H_2O)$

Preparation was repeated according to Mori et al.[4] 2g of nitrilotriacetic acid were dissolved in 12.5mL of 2.5M potassium bicarbonate. 2.5g of cobalt chloride hexahydrate and 500uL of 30% hydrogen peroxide were added and the mixture was stirred in an ice bath for 5 hours. The mixture was filtered and washed with cold water to reveal blue/purple crystals. Crystals were recrystallized in hot water containing potassium acetate followed by washing with ether.

Synthesis of $Co(III)(acacen)(NH_3)_2$

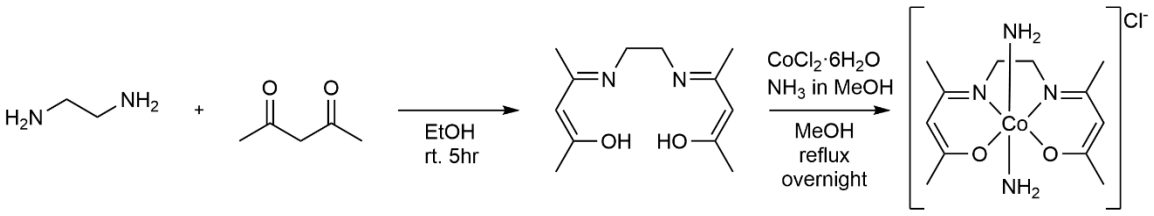

Figure 2.5 Synthetic scheme for acacen and $Co(III)(acacen)(NH_3)_2$.

Synthesis was based on the literature.[5]

Ligand Synthesis: Ethylenediamine (2.71 g, 45.1 mmol) was dissolved in ethanol (50 mL). A solution of freshly distilled acetylacetone (9.21 mL, 90.2 mmol) in ethanol was added drop-wise over 2 h with continuous stirring. The mixture was stirred for an additional 3 h, then filtered. The solid was washed successively with water (3 × 20 mL) and diethyl ether (3 × 20 mL) and dried under vacuum to give the acacen ligand.

^1H NMR (400 MHz, $CDCl_3$) δ 10.90 (s, 2H), 4.99 (s, 2H), 3.49 – 3.36 (m, 4H), 2.00 (s, 6H), 1.91 (s, 6H).

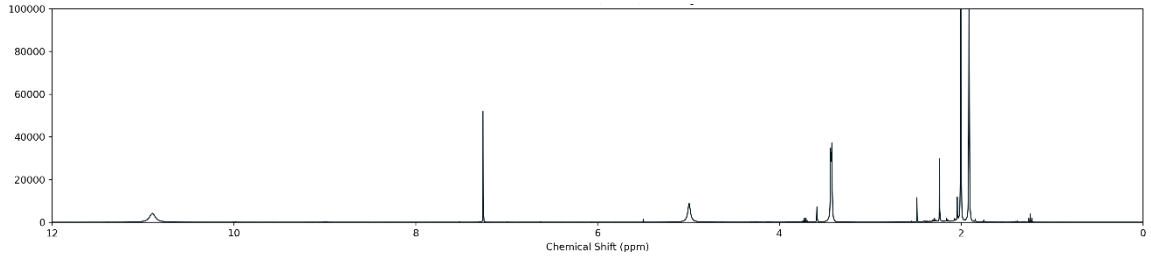

Figure 2.6 NMR spectrum of acacen ligand. Measured in $CDCl_3$.

Metal Complexation: The isolated acacen ligand (500 mg, 2.22 mmol) was dissolved in methanol (50 mL). Cobalt(II) chloride hexahydrate (541 mg, 2.27 mmol) was added under a nitrogen atmosphere, and the solution was heated to 60 °C with stirring for 30 min. Saturated ammonia in methanol (0.25 mL) was then introduced, and the mixture was refluxed for 1 h. An additional 2.5 mL of saturated ammonia in methanol was added, after which oxygen was bubbled through the reaction mixture overnight. The resulting solid was collected by filtration, washed with cold methanol (3 × 10 mL) followed by diethyl ether (3 × 10 mL), and dried under vacuum to yield Co(acacen)$(NH_3)_2 \cdot Cl$.

^{1}H NMR (400 MHz, D_2O) δ 5.15 (s, 2H), 3.61 (s, 4H), 2.25 (s, 6H), 2.09 (s, 6H).

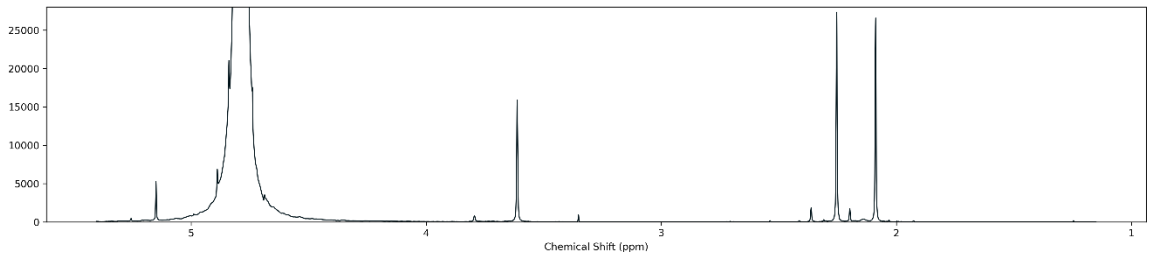

Figure 2.7 NMR spectrum of Co(acacen)$(NH_3)_2$. Measured in D_2O.

Synthesis of Co(III)(acacen)(Imidazole)$_2$

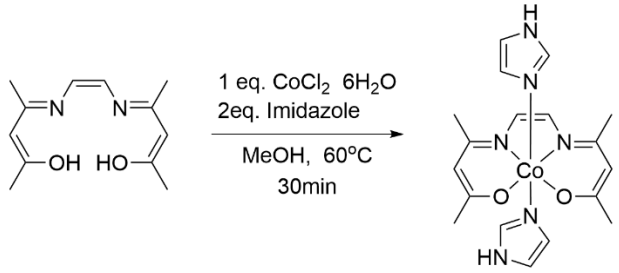

Figure 2.8 Synthetic scheme for Co(III)(acacen)(Im)$_2$.

The isolated acacen ligand (500 mg, 2.22 mmol) was dissolved in methanol (50 mL). Cobalt(II) chloride hexahydrate (541 mg, 2.27 mmol) was added under a nitrogen atmosphere, and the solution was heated to 60 °C with stirring for 30 min. 302 mg (4.44mmol) of imidazole dissolved in methanol were added and the reaction was stirred for three hours, after which oxygen was bubbled through the reaction mixture overnight. The resulting solid was collected by filtration, washed with cold methanol (3 × 10 mL) followed by diethyl ether (3 × 10 mL), and dried under vacuum to yield Co(acacen)(Im)$_2$·Cl.

^{1}H NMR (400 MHz, D_2O) δ 7.45 (d, J = 1.5 Hz, 3H), 7.02 (t, J = 1.6 Hz, 2H), 6.68 (t, J = 1.5 Hz, 2H), 3.43 (s, 4H), 2.25 (s, 6H), 2.06 (s, 6H).

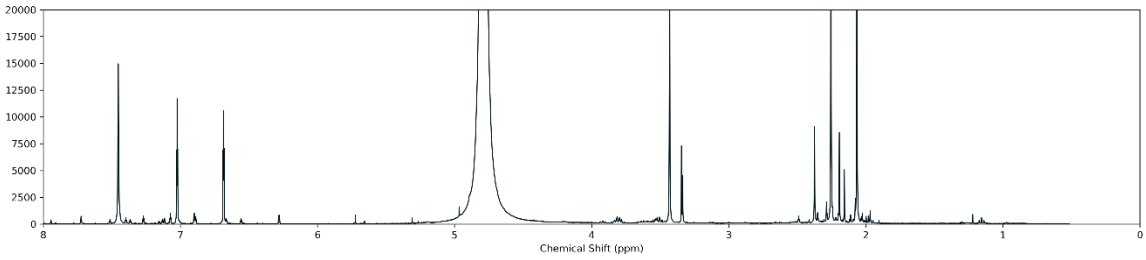

Figure 2.9 NMR spectrum of Co(III)(acacen)(Im)$_2$. Measured in D_2O.

Spectroscopic Techniques

UV-Vis

Absorption spectra were collected on an Agilent 8453 UV-Vis spectrophotometer.

Luminescence Spectroscopy

Fluorescence spectra were recorded on a modified Jobin Yvon Fluorolof-3 using two Ocean Optics QEPro CCD spectrometers as detectors spanning the 300-900nm range. The excitation wavelength used for tryptophan emission spectra was 280nm. The excitation wavelength used for GFP emission when conducting the in vitro assays was 488nm.

Circular Dichroism

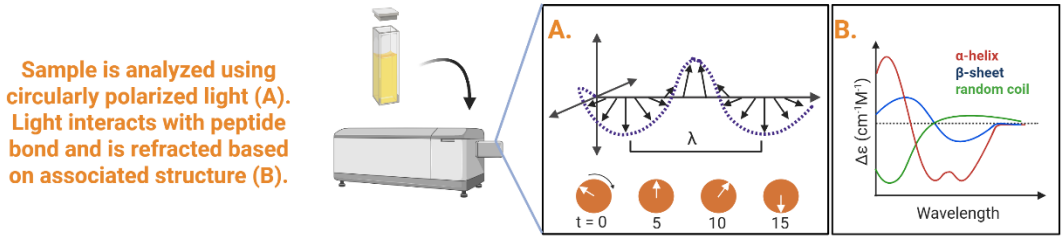

Figure 2.11 Circular dichroism description and schematic. Figure created with Biorender.com.

Circular dichroism spectra were recorded on an Aviv Model 430 spectropolarimeter. Spectra were collected from 190-250nm.

Time Resolved Fluorescence Energy Transfer

For the tryptophan fluorescence decay kinetics the excitation source was the fourth harmonic (266nm, 10ps, 10Hz) of a regeneratively amplified passively mode-locked Nd:YAG laser. Tryptophan fluorescence was collected using reflective optics, filtered through a monochromator, and detected with a picosecond streak camera (Hamamatsu C5680)

Nuclear Magnetic Resonance

NMR measurements were performed at room temperature, obtained using a Varian 400 MHz and the Bruker 400MHz spectrometer. ^{1}H chemical shifts were reported in ppm relative to tetramethylsilane, using residual proton and 13C resonances from solvent as an internal standard.

For ^{59}Co NMR studies, a Bruker Neo 400 with a broadband iProbe was used. It operates at 95.79 MHz for 59Co. The standard parameters called for 16,000 scans with a 10 microsecond observe pulse, a 20 millisecond acquisition time, a 100 millisecond relaxation delay, and a 100,000 Hz (1,044 ppm) sweep width.

Electron Paramagnetic Resonance

X-band CW-EPR spectra were collected using a Bruker EMX spectrometer at 77 K with a quartz liquid nitrogen immersion dewar. Samples were prepared as frozen glasses in 30% glycerol. Pulse ENDOR and HYSCORE spectroscopy were conducted on a Bruker ELEXSYS E580 pulse EPR spectrometer, equipped with either a Bruker MD4 (X-band) or D2 (Q-band) resonator. Temperature control was maintained via a ColdEdge ER 4118HV-CF5-L Flexline Cryogen-Free VT cryostat, coupled with an Oxford Instruments Mercury ITC temperature controller. CW-EPR spectra were simulated using EasySpin's least-squares fitting algorithm (esfit) with the solid-state simulation function (pepper). HYSCORE spectra were simulated using the solid-state pulse EPR module (saffron).

Computational Techniques

Computational Modelling in Copper Studies

For the computational methods used for the copper studies Moon Young Yang and William A. Goddard have provided the following description.

All QM computations were performed using Orca 5.[6] Geometry optimizations were carried out with the B3LYP functional.[7–9] The conductor-like polarizable continuum (CPCM) solvation model was used to account for solvent effects of water.[10] Scalar relativistic effects were treated

using the zeroth-order regular approximation (ZORA).[11,12] The ZORA-recontracted[13] version of the def2-TZVPP basis set[14] was used for Cu and the ZORA-def2-TZVP for all other atoms, along with fully decontracted def2/J auxiliary basis sets.[15] For the calculation of hyperfine coupling and g-tensors, the B2GP-PLYP double-hybrid functional was used[16], which is known to accurately predict the EPR properties for Cu(II) complexes.[17] NoFrozenCore option and tight convergence criteria were used for the calculations with double-hybrid functionals. VMD[18] and Avogadro[19] programs were used for visualization, and EPR simulations were performed using the EasySpin software package.

Computational Modelling in Cobalt Studies

For the computational methods used for the cobalt studies Moon Young Yang has provided the following description.

Computational Co-59 NMR chemical shifts (δ^{59}Co) of Co(III) complexes were computed using the Gaussian16 program. [20] The chemical shift was defined as:

$$\delta^{59}\mathrm{Co} = \sigma_{\mathrm{ref}} - \sigma_{\mathrm{calc}}$$

where σ_{ref} is the calculated shielding constant of the reference complex, $[Co(CN)_6]_3^-$, and σ_{calc} is the shielding constant of the Co(III) complexes investigated in this study.

Geometry optimizations were performed at the BLYP/def2-SVP level of theory under the IEF-PCM implicit solvent model. The Co-59 shielding constants were then calculated using the Gauge-Independent Atomic Orbital (GIAO) approach at the GIAO-LC-ωPBE/NMR-DKH level of theory under the IEF-PCM implicit solvent model. This computational protocol has been previously validated for a benchmark set of 34 Co(III) complexes. [21]

For the *in silico* virtual screening of Nsp1 inhibitors, Joo Youn Lee provided the following descriptions.

Structure-based Virtual Screening

Structure-based virtual screening (SBVS) was performed to identify small-molecule inhibitors against Nsp1. Molecular docking was conducted for three binding sites around Nsp1 using Schrödinger Suite 2023-2 (Schrödinger LLC, New York, USA, 2023). The cryo-electron microscopy structure of Nsp1 bound to the human 40S ribosomal subunit (PDB ID 6ZLW) was obtained from the Protein Data Bank (https://www.rcsb.org) and prepared using Protein Preparation Wizard in Maestro v13.6. A receptor grid box of 25 Å x 25 Å x 25 Å was generated centered on Lys164 and His165, two residues located in C-terminal domain of Nsp1 that are involved in the interaction with the 40S proteasome. A chemical library comprising approximately 6.2 million compounds from ChemBridge, ChemDiv, and Enamine suppliers was employed for virtual screening. All compounds were prepared using LigPrep with OPLS_2005 force field to generated low-energy 3D conformations and appropriate ionization states. Molecular docking was performed using Glide v9.9 with standard precision (SP) mode. Based on the docking score and visual inspection of the binding modes, 340 compounds were selected for further in silico analysis.

Molecular Dynamics (MD) simulations

To further refine the docking results and predicted the binding free energy for 340 compounds in complex with Nsp1 structure, molecular dynamics (MD) simulations were performed using Desmond v7.4 with OPLS_2005 force field in Schrödinger Suite 2023-2 (Desmond Molecular Dynamics System; D. E. Shaw Research: New York, NY, 2024). The System Builder was used for solvation, employing predefined TIP3P water molecules in an orthorhombic box with dimensions of 10 Å x 10 Å x 10 Å. The overall system was neutralized by adding Cl- counterions placed at least 25 Å from the ligand. The NaCl concentration was adjusted to 0.15 mol/L. Short MD simulations of 20 ns were conducted under periodic boundary conditions in the NPT ensemble at normal temperature (300 K) and pressure (1.01325 bar). Energy calculations and trajectory data were recorded at intervals of 1.2 and 500 ps, respectively.

Molecular Mechanics-Generalized Born Surface Area (MM-GBSA) calculation

The final equilibrium states for 340 protein-ligand docking poses were rescored using the MM-GBSA approach, as implemented in the Prime MM-GBSA module in the Schrödinger Suite 2023-2 (Schrödinger LLC, New York, USA, 2023). The OPLS_2005 force field, VSGB solvation model, and default Prime parameters were used for the MM-GBSA calculations. Ligand binding free energies were calculated from 20 frames extracted from the final 20 ns of each MD trajectory. The top 31 compounds were selected based on the predicted binding free energies and visual inspection of binding poses.

Alphafold3

AlphaFold predictions were performed using the AlphaFold3 server by inputting the amino acid sequence of the peptide or protein, followed by the inclusion of relevant metal ions.[22]

Data Analysis

Data analysis was performed using MATLAB (MathWorks Inc.) or Python within JupyterLab, unless otherwise specified. NMR data were analyzed using MestReNova. Chemical structures were drawn using ChemDraw. Protein visualizations presented in this thesis were created using a combination of PyMOL, Discovery Studio Visualizer, and BioRender.com. All citations were managed and generated using Zotero.

References

(1) Schubert, K.; Karousis, E. D.; Jomaa, A.; Scaiola, A.; Echeverria, B.; Gurzeler, L.-A.; Leibundgut, M.; Thiel, V.; Mühlemann, O.; Ban, N. SARS-CoV-2 Nsp1 Binds the Ribosomal mRNA Channel to Inhibit Translation. *Nat Struct Mol Biol* **2020**, *27* (10), 959–966. https://doi.org/10.1038/s41594-020-0511-8.

(2) Bürgisser, C. S.; Stone, A. T. Determination of EDTA, NTA, and Other Amino Carboxylic Acids and Their Co(II) and Co(III) Complexes by Capillary Electrophoresis. *Environ Sci Technol* **1997**, *31* (9), 2656–2664. https://doi.org/10.1021/es970080f.

(3) Zhang, Q.-Z.; Lu, C.-Z.; Yang, W.-B. Synthesis and Structures of Two Cobalt Complexes $[NaCo^{II}(NTA)(H_2O)]_n$ and $NH_4[Co^{III}(IDA)_2] \cdot 2H_2O$. *J Coord Chem* **2006**, *59* (8), 837–844. https://doi.org/10.1080/00958970500412081.

(4) Mori, M.; Shibata, M.; Kyuno, E.; Okubo, Y. Studies on the Synthesis of Metal Complexes. IV. The Cobalt (III) Complexes of Ammoniatriacetic Acid. *Bull Chem Soc Jpn* **1958**, *31* (8), 940–944. https://doi.org/10.1246/bcsj.31.940.

(5) Takeuchi, T.; Böttcher, A.; Quezada, C. M.; Simon, M. I.; Meade, T. J.; Gray, H. B. Selective Inhibition of Human α-Thrombin by Cobalt(III) Schiff Base Complexes. *J Am Chem Soc* **1998**, *120* (33), 8555–8556. https://doi.org/10.1021/ja981191x.

(6) Neese, F.; Wennmohs, F.; Becker, U.; Riplinger, C. The ORCA Quantum Chemistry Program Package. *J Chem Phys* **2020**, *152* (22), 224108. https://doi.org/10.1063/5.0004608.

(7) Becke, A. D. Density-Functional Exchange-Energy Approximation with Correct Asymptotic Behavior. *Phys Rev A* **1988**, *38* (6), 3098–3100. https://doi.org/10.1103/PhysRevA.38.3098.

(8) Lee, C.; Yang, W.; Parr, R. G. Development of the Colle-Salvetti Correlation-Energy Formula into a Functional of the Electron Density. *Phys Rev B* **1988**, *37* (2), 785–789. https://doi.org/10.1103/PhysRevB.37.785.

(9) Becke, A. D. A New Mixing of Hartree–Fock and Local Density-Functional Theories. *J Chem Phys* **1993**, *98* (2), 1372–1377. https://doi.org/10.1063/1.464304.

(10) Marenich, A. V.; Cramer, C. J.; Truhlar, D. G. Universal Solvation Model Based on Solute Electron Density and on a Continuum Model of the Solvent Defined by the Bulk Dielectric Constant and Atomic Surface Tensions. *J Phys Chem B* **2009**, *113* (18), 6378–6396. https://doi.org/10.1021/jp810292n.

(11) Van Lenthe, E.; Baerends, E. J.; Snijders, J. G. Relativistic Total Energy Using Regular Approximations. *The Journal of Chemical Physics* **1994**, *101* (11), 9783–9792. https://doi.org/10.1063/1.467943.

(12) Lenthe, E. V.; Baerends, E. J.; Snijders, J. G. Relativistic Regular Two-Component Hamiltonians. *J Chem Phys* **1993**, *99* (6), 4597–4610. https://doi.org/10.1063/1.466059.

(13) Pantazis, D. A.; Chen, X.-Y.; Landis, C. R.; Neese, F. All-Electron Scalar Relativistic Basis Sets for Third-Row Transition Metal Atoms. *J Chem Theory Comput* **2008**, *4* (6), 908–919. https://doi.org/10.1021/ct800047t.

(14) Weigend, F.; Ahlrichs, R. Balanced Basis Sets of Split Valence, Triple Zeta Valence and Quadruple Zeta Valence Quality for H to Rn: Design and Assessment of Accuracy. *Phys Chem Chem Phys* **2005**, *7* (18), 3297–3305. https://doi.org/10.1039/B508541A.

(15) Weigend, F. Accurate Coulomb-Fitting Basis Sets for H to Rn. *Phys Chem Chem Phys* **2006**, *8* (9), 1057–1065. https://doi.org/10.1039/B515623H.

(16) Karton, A.; Tarnopolsky, A.; Lamère, J.-F.; Schatz, G. C.; Martin, J. M. L. Highly Accurate First-Principles Benchmark Data Sets for the Parametrization and Validation of Density Functional and Other Approximate Methods. Derivation of a Robust, Generally Applicable, Double-Hybrid Functional for Thermochemistry and Thermochemical Kinetics. *J Phys Chem A* **2008**, *112* (50), 12868–12886. https://doi.org/10.1021/jp801805p.

(17) Drosou, M.; Mitsopoulou, C. A.; Orio, M.; Pantazis, D. A. EPR Spectroscopy of Cu(II) Complexes: Prediction of g-Tensors Using Double-Hybrid Density Functional Theory. *Magnetochemistry* **2022**, *8* (4), 36. https://doi.org/10.3390/magnetochemistry8040036.

(18) Humphrey, W.; Dalke, A.; Schulten, K. VMD: Visual Molecular Dynamics. *J Mol Graph* **1996**, *14* (1), 33–38. https://doi.org/10.1016/0263-7855(96)00018-5.

(19) Hanwell, M. D.; Curtis, D. E.; Lonie, D. C.; Vandermeersch, T.; Zurek, E.; Hutchison, G. R. Avogadro: An Advanced Semantic Chemical Editor, Visualization, and Analysis Platform. *J Cheminform* **2012**, *4* (1), 17. https://doi.org/10.1186/1758-2946-4-17.

(20) Frisch, M. J.; Trucks, G. W.; H. B. Schlegel, H. B.; Scuseria, G. E.; Robb, M. A.; Cheeseman, J. R. ; Scalmani, G.; Barone, V.; Petersson, G. A.; Nakatsuji, H.; Li, X.; Caricato, M.; Marenich, A. V.; Bloino, J.; B. G. Janesko, B. G.; Gomperts, R.; Mennucci, B.; Hratchian, H. P. ; Ortiz, J. V.; Izmaylov, A. F.; Sonnenberg, J. L.; Williams-Young, D.; Ding, F.; Lipparini, F.; Egidi, F.; Goings, J.; Peng, B.; Petrone, A.; Henderson, T.; Ranasinghe, D.; Zakrzewski, V. G.; Gao, J.; Rega, N.; Zheng, G.; Liang, W.; Hada, M.; Ehara, M.; Toyota, K.; Fukuda, R.; Hasegawa, J.; Ishida, M.; Nakajima, T.; Honda, Y.; Kitao, O.; Nakai, H.; Vreven, T.; Throssell, K.; Montgomery, Jr., J. A.; Peralta, J. E. ; Ogliaro, F.; Bearpark, M. J.;

Heyd, J. J.; Brothers, E. N.; Kudin, K. N.; Staroverov, V. N.; Keith, T. A.; Kobayashi, R.; Normand, J.; Raghavachari, K.; Rendell, A. P.; Burant, J. C.; Iyengar, S. S.; Tomasi, J.; Cossi, M.; Millam, J. M.; Klene, M.; Adamo, C.; Cammi, R.; Ochterski, J. W.; Martin, R. L.; Morokuma, K.; Farkas, O.; Foresman, J. B.; and Fox, D. J.. Gaussian16, 2016.

(21) Gomes, M. G. R.; De Souza, A. L. F.; Dos Santos, H. F.; De Almeida, W. B.; Paschoal, D. F. S. Assessment of a Computational Protocol for Predicting Co-59 NMR Chemical Shift. *Magnetochemistry* **2023**, *9* (7), 172. https://doi.org/10.3390/magnetochemistry9070172.

(22) Abramson, J.; Adler, J.; Dunger, J.; Evans, R.; Green, T.; Pritzel, A.; Ronneberger, O.; Willmore, L.; Ballard, A. J.; Bambrick, J.; Bodenstein, S. W.; Evans, D. A.; Hung, C.-C.; O'Neill, M.; Reiman, D.; Tunyasuvunakool, K.; Wu, Z.; Žemgulytė, A.; Arvaniti, E.; Beattie, C.; Bertolli, O.; Bridgland, A.; Cherepanov, A.; Congreve, M.; Cowen-Rivers, A. I.; Cowie, A.; Figurnov, M.; Fuchs, F. B.; Gladman, H.; Jain, R.; Khan, Y. A.; Low, C. M. R.; Perlin, K.; Potapenko, A.; Savy, P.; Singh, S.; Stecula, A.; Thillaisundaram, A.; Tong, C.; Yakneen, S.; Zhong, E. D.; Zielinski, M.; Žídek, A.; Bapst, V.; Kohli, P.; Jaderberg, M.; Hassabis, D.; Jumper, J. M. Accurate Structure Prediction of Biomolecular Interactions with AlphaFold 3. *Nature* **2024**, *630* (8016), 493–500. https://doi.org/10.1038/s41586-024-07487-w.

Chapter 3

COPPER BINDING TO NSP1 PEPTIDES

Introduction

Nsp1 is a potent SARS-CoV-2 virulence factor and a promising antiviral drug target. However, its C-terminal polypeptide lacks a well-defined folded structure, making conventional structure-based drug discovery approaches ineffective. Many viral proteins contain intrinsically disordered protein regions (IDPRs), which contribute to their adaptability and survival in dynamic host environments.[1] These flexible regions often undergo disorder-to-order transitions upon binding to host factors, but their lack of stable pockets makes them difficult to inhibit with traditional small-molecule therapeutics.

Given these challenges, alternative approaches such as metal-based inhibition are promising routes for drug discovery. Transition metals can interact with disordered protein regions via coordination to specific amino acid side chains, potentially stabilizing transient conformations or disrupting native interactions. The C-terminal region of Nsp1 (residues 148−180, ELGTDPYEDFQENWNTKHSSGVTRELMRELNGG) contains several potential metal-binding residues, including histidine, aspartate, and glutamate. In this chapter, we explore how Cu(II) interacts with Nsp1-derived peptides using circular dichroism spectroscopy, fluorescence measurements, electron paramagnetic resonance (EPR) techniques, and computational modelling to assess structural changes upon metal binding. These studies provide insight into the coordination environment of Cu(II) and its potential impact on Nsp1 function.

Copper in Biology

Life has evolved through the interactions of both organic and inorganic compounds. Organic components such as amino acids, nucleotides, and carbohydrates form the backbone of biological macromolecules. In contrast, inorganic compounds, particularly those involving metal ions, play essential roles in enzymatic catalysis, structural stabilization, and electron transport. Examples include heme groups, vitamin B12, and metalloenzymes such as lytic polysaccharide monooxygenases.

Copper is a d-block, first-row transition metal with two biologically relevant oxidation states: its reduced state, Cu(I), or its oxidized state, Cu(II). [2] Cu(I), a soft metal center, exhibits high affinity for thiol and thioether groups, commonly coordinating with cysteine and methionine residues. Cu(II), on the other hand, is more inclined to bind oxygen donors, imidazole rings of histidines,

and amine nitrogen atoms. [3] According to the Irving-Williams series, Cu(II) forms more stable complexes than most other biologically relevant divalent metal ions, with the general trend being Mn < Fe < Co < Ni < Cu > Zn.[4]

Organisms have evolved tightly regulated copper homeostasis systems to create a balance and avoid cytotoxicity. These mechanisms involve a network of transporters, chaperones, and storage proteins that maintain copper at optimal concentrations. In humans, copper uptake occurs primarily through the intestine via CTR1 (Copper Transporter 1), after which intracellular chaperones like ATOX1, CCS, and COX17 direct the metal to its target destinations, including cuproenzymes in the mitochondria, cytosol, and Golgi apparatus. Excess copper is sequestered or exported by ATP7A and ATP7B, P-type ATPases critical for preventing toxic accumulation. [5] Disruptions in these pathways can lead to copper-related disorders: Wilson's disease results from mutations in ATP7B, leading to hepatic copper buildup and neurological symptoms, while Menkes disease arises from ATP7A mutations and manifests as copper deficiency in the brain and connective tissues.[6,7] Copper's toxicity is a result of its redox activity and ability to catalyze the formation of reactive oxygen species (ROS) which damages DNA, lipids, and proteins.[8,9] This delicate balance between copper's utility and toxicity highlights the importance of tightly controlled homeostasis in both health and disease.

Copper's high affinity for biological ligands makes it both an essential micronutrient and a potential cytotoxin. At physiological levels, copper is used by the immune system to enhance the phagocytic and bactericidal activity of neutrophils and macrophages. [10] However, excess copper can disrupt cellular function, outcompete other metal ions for binding sites, and catalyze the formation of reactive oxygen species. Acute copper toxicity can result in nausea, vomiting, hematemesis, hypotension, jaundice, and gastrointestinal distress. Chronic exposure can cause liver and kidney damage.[11] Disorders such as Wilson's disease, a rare autosomal recessive condition, impair copper excretion and result in toxic accumulation, particularly in the liver.[6] Conversely, copper deficiency can cause anemia, neutropenia, and neurological symptoms, as seen in Menkes disease, a disorder of impaired copper transport.[7]

Historically, copper has long been recognized for its antimicrobial properties. Ancient Egyptians used copper vessels to purify drinking water and treat wounds as early as 2600 BCE. Greek physicians employed copper compounds for sanitation and the treatment of infections.[12] In

19th-century Europe, workers in the copper industry were noted to have lower incidence of cholera, hinting at copper's protective effects. [13]Although antibiotics became the standard of care in the 20th century, copper remains relevant for infection control, particularly in the face of rising antibiotic resistance.

Today, copper continues to be used in various biomedical applications. It has been shown to possess bactericidal, fungicidal, and antiviral properties. Copper surfaces drastically reduce the survival time of viruses such as Influenza A and SARS-CoV-2 compared to stainless steel or plastic.[14,15] Copper complexes of non-steroidal anti-inflammatory drugs (NSAIDs) have demonstrated enhanced anti-inflammatory and anti-ulcer effects.[16] Copper-based chemotherapeutics and contraceptive devices such as copper intrauterine devices (IUDs) are in clinical use and used by many around us, showcasing copper's therapeutic versatility.[17]

Given its versatile coordination chemistry, redox activity, and deep evolutionary significance, copper occupies a unique niche in biological systems, acting as both a vital micronutrient and a potent cytotoxin. The fine balance between its beneficial and harmful effects is tightly regulated by sophisticated homeostatic mechanisms across all domains of life. Disruptions in this balance are linked to numerous human diseases and can also be strategically exploited for therapeutic purposes. The following chapter explores the complex roles of copper in biology, with a particular focus on its interactions with SARS-CoV-2 Nsp1. Through spectroscopic and computational approaches, these studies investigate how copper's unique chemical properties may be leveraged to disrupt viral function and inform future antiviral strategies.

Results and Discussion

Insights on Intrinsically Disordered Region of Nsp1

The C-terminal of Nsp1 is intrinsically disordered and fluctuates in shape. Using Alphafold3, predictions indicate that it is expected to be mostly helical (Figure 3.1). When the C-terminal is bound to the 40S ribosome this is the case. It adopts a helix-turn-helix shape in the process of blocking the mRNA entry channel. However, prediction and experimentation can vary, therefore obtaining insights into this region of Nsp1 are important for future targetability and drug design when responding to SARS-CoV-2.

Figure 3.1 Alphafold3 prediction of the C-terminal of Nsp1. The blue regions indicate a region of high confidence in the prediction and yellow signifying weaker confidence.

Circular dichroism (CD) spectroscopy provides valuable insights into protein secondary structure, as distinct structural elements such as α-helices and β-sheets exhibit characteristic spectral features in the far-UV region. The far-UV CD spectrum of the Nsp1 C-terminal domain (Nsp1-CT_{33}) displays a pronounced negative ellipticity minimum at 200 nm and a shoulder near 230 nm (Figure 3.2). The molar ellipticity minimum at 200 nm is indicative of a significant random coil content (~40%), with a likely positive contribution from β-sheet or turn structures offsetting the signal. Spectral deconvolution into three components—α-helix, β-sheet, and random coil—reveals that the peptide predominantly adopts β-sheet conformations, with minimal α-helical content (<5%) (Figure 3.2).

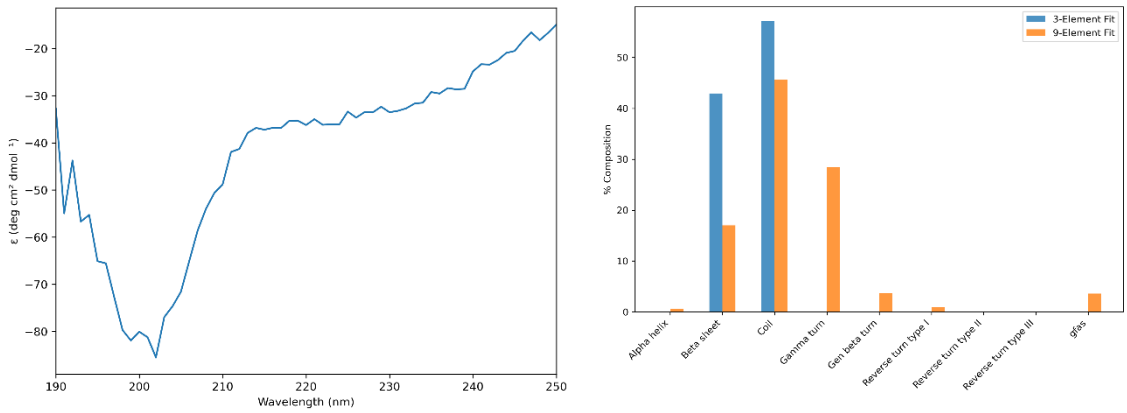

Figure 3.2 The circular dichroism spectrum of Nsp1-CT_{33} can be seen on the left and on the right is the are the elemental fit analysis results that break down the spectrum into its different secondary structures.

The addition of metal ion salts at varying equivalents induces structural changes in the peptide, as evidenced by shifts in the circular dichroism (CD) spectrum. Notably, Cu(II) causes a

significant spectral shift (Figure 3.3), suggesting that its binding promotes the formation of a more defined secondary structure.

Fluorescence spectra were also collected for different metal ions across a range of concentrations, monitoring tryptophan fluorescence. Cu(II) binding results in significant fluorescence quenching, indicating direct interaction with the peptide's fluorophores. In contrast, other metal ions cause minimal quenching or even slight fluorescence enhancement, suggesting weaker or nonspecific interactions. The pronounced spectral changes observed in both CD and fluorescence measurements upon Cu(II) binding suggest a strong coordination with the peptide, warranting further investigation.

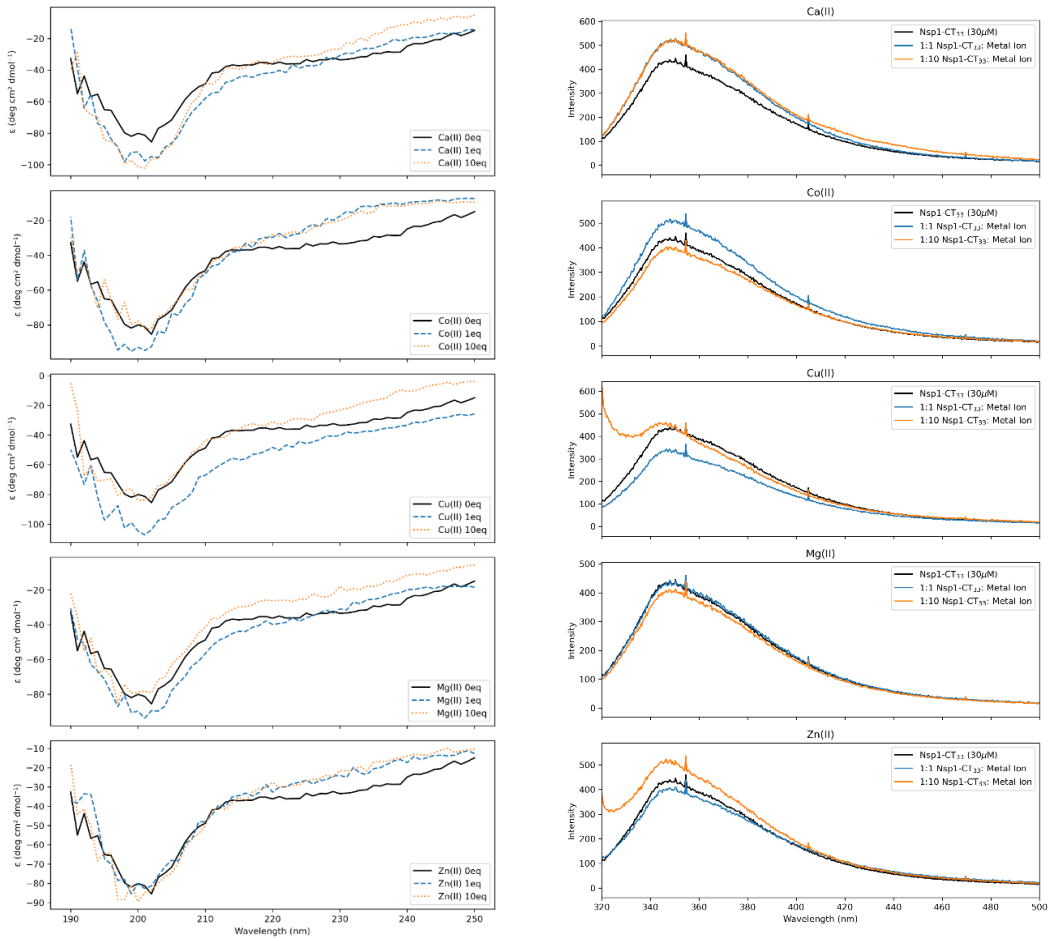

Figure 3.3 On the left the circular dichroism spectra for Nsp1-CT_{33} with different metal ions can be found and on the left is the fluorescence spectra. For the circular dichroism spectra, 0eq refers to no metal ion presence only Nsp1-CT_{33}.

Due to the intrinsically disordered nature of Nsp1, studying its structure under different conditions can provide insights into its conformational preferences and potential functional roles. Trifluoroethanol (TFE) is known to stabilize α-helical conformations, mimicking conditions that may arise upon binding to other biomolecules. This can help determine whether the peptide has an inherent helical propensity that could be relevant in biological contexts. TFE is a slightly stronger proton donor than water but a much weaker proton acceptor. It primarily disrupts non-local hydrophobic interactions while slightly enhancing α-helical properties.[18]

Since intrinsically disordered regions (IDRs) often undergo disorder-to-order transitions upon interacting with ligands or binding partners, TFE-induced α-helicity could indicate whether metal binding stabilizes a more structured state. Figure 3.4 shows the effects of adding 30% TFE to the peptide, as well as the impact of Cu(II) binding.

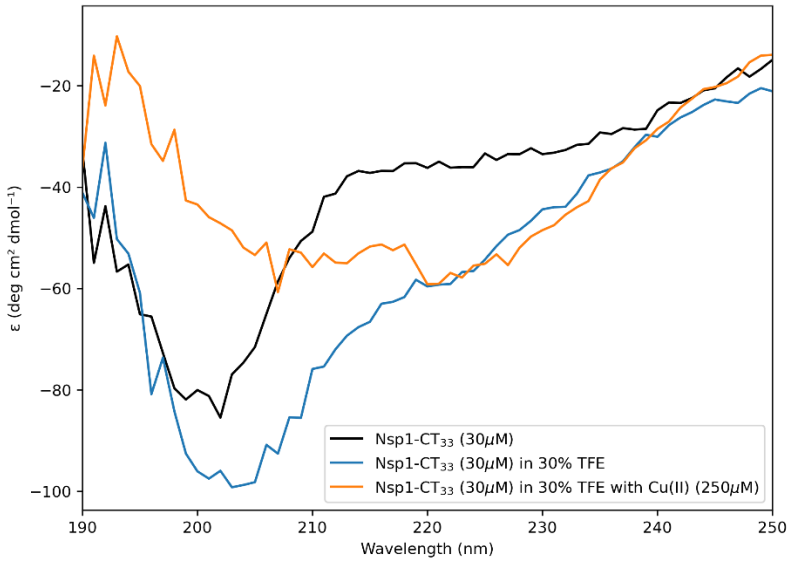

Figure 3.4 The circular dichroism spectra of Nsp1-CT_{33} in the presence of trifluoroacetic acid (TFE) and the effects of adding copper.

The CD spectrum of Nsp1-CT_{33} shows a strong negative peak near 200 nm, characteristic of a predominantly random coil conformation. The absence of a peak at 222 nm confirms the lack of α-helical structure. Upon addition of TFE, the negative peak at 200 nm decreases, while new negative peaks emerge at 208 nm and 222 nm, indicating a transition toward a more ordered state with partial α-helical formation. TFE, a helix-stabilizing solvent that mimics hydrophobic

environments, promotes this structural shift by stabilizing transient helical segments within the disordered protein. Finally, the addition of Cu(II) further enhances helicity, as seen by a deeper 222 nm peak. This suggests that Cu(II) stabilizes α-helical conformations, and the observed peak broadening or shift may indicate the formation of tertiary contacts induced by metal coordination.

All of this work led to further studies on the impact of Cu(II) binding on Nsp1-CT_{33}. While CD spectroscopy demonstrated that Cu(II) promotes helicity and may induce tertiary contacts, it does not provide direct information about specific binding interactions. To gain further insight into these interactions, fluorescence spectroscopy was employed to assess changes in the local environment of aromatic residues. Monitoring tryptophan fluorescence allows for the detection of binding-induced quenching, which can indicate direct coordination or conformational rearrangements upon Cu(II) addition.

Tryptophan fluorescence serves as a sensitive indicator of the polarity of the surrounding environment, offering insight into structural changes upon ligand binding.[19] In Nsp1-CT_{33}, W161 exhibits fluorescence with a maximum at 350 nm, consistent with a solvent-exposed indole group. The addition of increasing concentrations of Cu(II) results in fluorescence quenching (Figure 3.3), suggesting direct interaction between Cu(II) and the tryptophan residue.

The fluorescence decay kinetics of the indole chromophore require an exponential function for accurate modeling, reflecting the complex dynamic environment of the residue (Equation 3.1).

$$\langle \tau \rangle = \int_0^\infty \frac{I(t)-I(\infty)}{I(0)-I(\infty)}\, dt \quad \text{(Equation 3.1)}$$

The effective fluorescence decay time of W161 in Nsp1-CT_{33} is approximately 2.4 ns, which is shorter than the 2.9 ns decay time observed for W4 in α-synuclein.[20] This suggests the presence of an additional quenching pathway for the singlet excited state of the indole chromophore in Nsp1-CT_{33}. To further investigate the structural dynamics of the peptide, fluorescence resonance energy transfer (FRET) was utilized using tryptophan and 3-nitrotyrosine as a donor-acceptor pair. This pair has a Förster distance of 26 Å, making it suitable for modeling the distance between W161 and Y154 (Figure 3.5).[21]

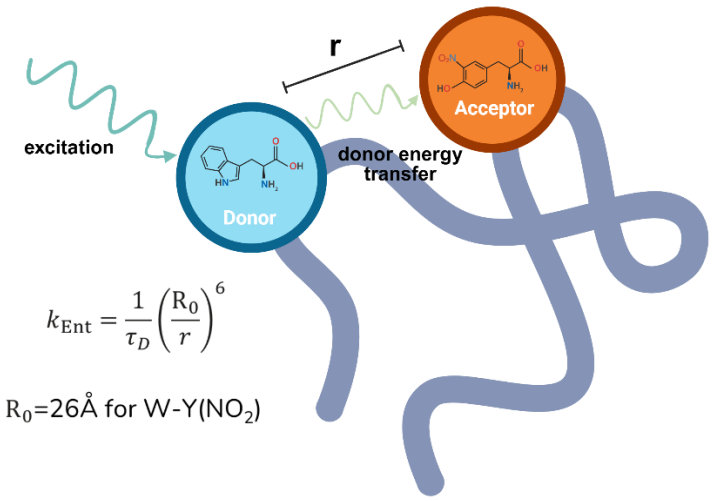

Figure 3.5 Visual representation of using time-resolved energy transfer for measuring distances between donor acceptor pairs.

In the cryo-EM structure of Nsp1 bound to the 40S ribosomal subunit, the centroid-to-centroid distance between W161 and Y154 is 15.4 Å.[22] A β-sheet model of Nsp1-CT_{33} predicts a distance of 29.7 Å. Applying the simplest Förster energy transfer model to Nsp1-CT_{33}-Y(NO_2)154 yields a W161-Y154 distance of approximately 24 Å. However, given that Nsp1-CT_{33} is an intrinsically disordered polypeptide, a single static distance is unlikely to accurately capture the conformational ensemble. Instead, a distribution of distances provides a more appropriate model for W161–Y(NO_2)154 interactions and the fluorescence decay of *W161.

In order to analyze the data, a minimum entropy model was employed to extract distances between the Förster energy transfer pair. The tryptophan luminescence decay kinetics were modeled to the function in Equation 2.2. Where $I_o(t)$ is the tryptophan fluorescence decay in the absence of the Tyr(NO_2). P(r) is the probability of observing a confirmation with donor-acceptor distance r, and $k_{et}(r)$ is the rate of the energy transfer at distance r.

$$I(t) = I_o(t)\int P(r)\exp(-k_{et}(r)t)dr \quad \text{(Equation 3.2)}$$

Distances were determined directly from the decay kinetics through numerical inversion of the Laplace transform describing $I(t)$, with the key constraint that $P(r)$ must remain nonnegative. To achieve this, a linear least-squares algorithm with a nonnegativity constraint was employed, yielding the narrowest P(k) distributions from fluorescence kinetics. These $P(k)$ distributions

were then converted into distance distributions using the Förster equation $r = D_o(k_R/k_{et})^{1/6}$, where $D_o = R_o\Phi_D^{1/6}$ and k_R represents the measured radiative decay rate constant of excited N-Acetyl-L-Tryptophanamide (NATA). The method allows for distance measurements up to an experimental limit of approximately 40 Å.

By extracting minimum entropy, model-independent distributions of W161–Y(NO_2)154 distances from energy-transfer kinetics (Figure 3.6), three distinct populations were identified: ~13 Å (29%), ~17 Å (46%), and ~28 Å (25%). The presence of a significant fraction of extended structures between W161 and Y(NO_2)154 aligns with CD spectra, which indicate β-sheet formation within the peptide.

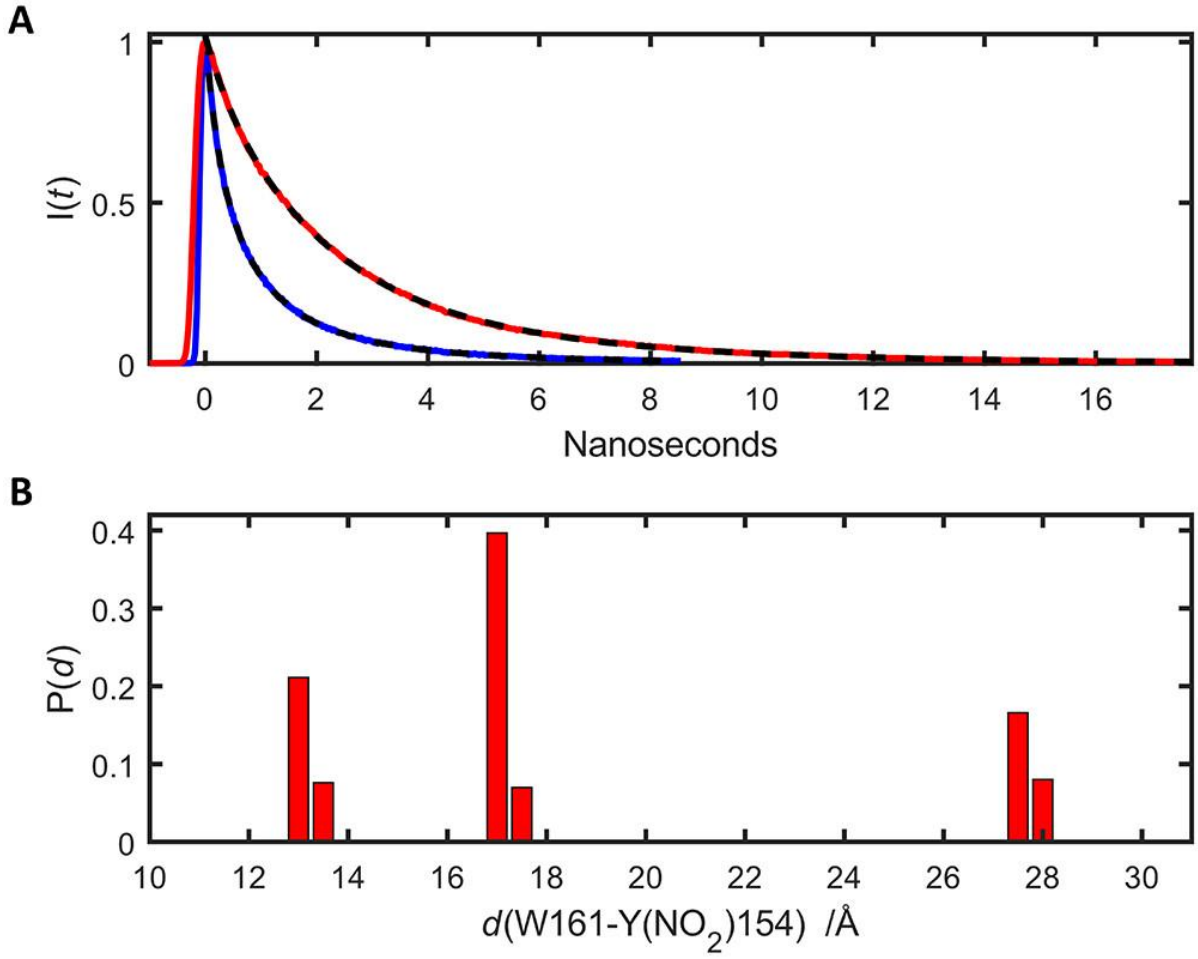

Figure 3.6 Time-Resolved Fluorescence and Distance Distributions Reveal W161–Y(NO_2)154 Energy Transfer Dynamics in Nsp1-CT_{33} (A) Nsp1-CT_{33} (red) and Nsp1-CT_{33} -Y(NO_2)154 (blue) W161 fluorescence decay kinetics ([Nsp1-CT_{33} = 30 μM, pH 6.5, MOPS 20 mM). Dashed black lines are fits to multiexponential decay functions with lifetime values of 2.4 and 0.9 ns. (B) Probability distribution of W161–Y(NO_2)154 distances extracted from W161 energy transfer kinetics.

Copper(II) Binding to Nsp1-CT

At pH 6.5, Nsp1-CT_{33} contains multiple residues capable of coordinating metal ions, including eight carboxylate groups and one imidazole. W161 in Nsp1-CT_{33} is particularly sensitive to low concentrations of Cu(II), as evidenced by the fluorescence quenching observed in Figure 3.7.

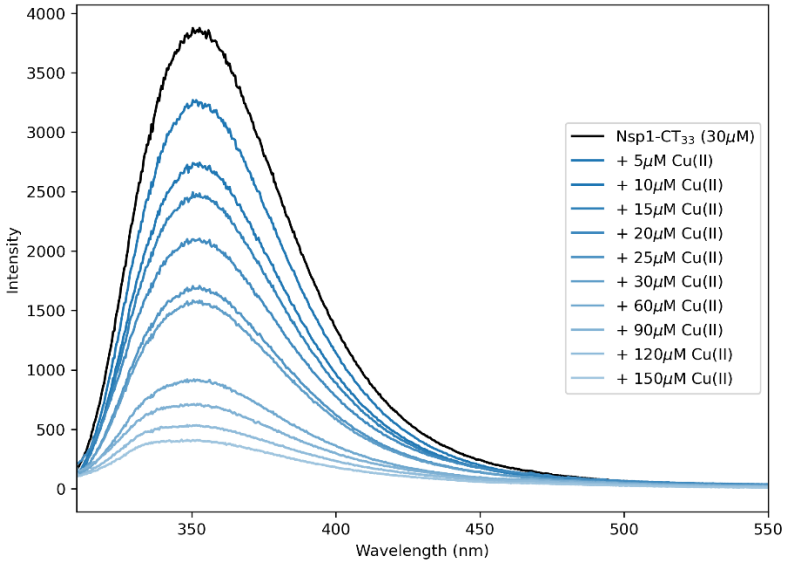

Figure 3.7 Tryptophan fluorescence quenching can be observed upon addition of Cu(II) to Nsp1-CT_{33}. Measurements were done in 20mM MOPS at pH 6.5.

At a peptide concentration of 30 μM, the addition of one molar equivalent of aquo Cu(II) results in a 25% decrease in W161 fluorescence intensity. Cu(II) also systematically reduces the effective W161 fluorescence lifetime. Modeling the decrease in the lifetime using a single Cu-binding-site model yields a dissociation constant of 9.7 μM at pH 6.5 (Figure 3.8). If the H165 is replaced with an alanine, the peptide is only weakly quenched, with a dissociation constant of 106μM at pH 6.5, this makes it clear that the H165 is the coordination site for the Cu(II) (Figure 3.8).

Aquo Cu(II) appears to quench *W161 fluorescence via electron transfer (ET), as indicated by the observed decrease in effective lifetime and a quenching rate constant of 5×10^8 s^{-1}. In structured proteins, an ET rate of this magnitude typically corresponds to a donor–acceptor distance of 10–14Å. [23] This is consistent with the 14 Å separation between the W161 indole and the Nε of H165 in the helix-turn-helix conformation of Nsp1 bound to the 40S ribosome.[22,24,25] However, the far-UV CD spectrum does not show a significant increase in α-helical content

upon Cu(II) binding (Figure 3.2), suggesting that the Cu(II):Nsp1-CT_{33} complex adopts a distinct conformation in solution.

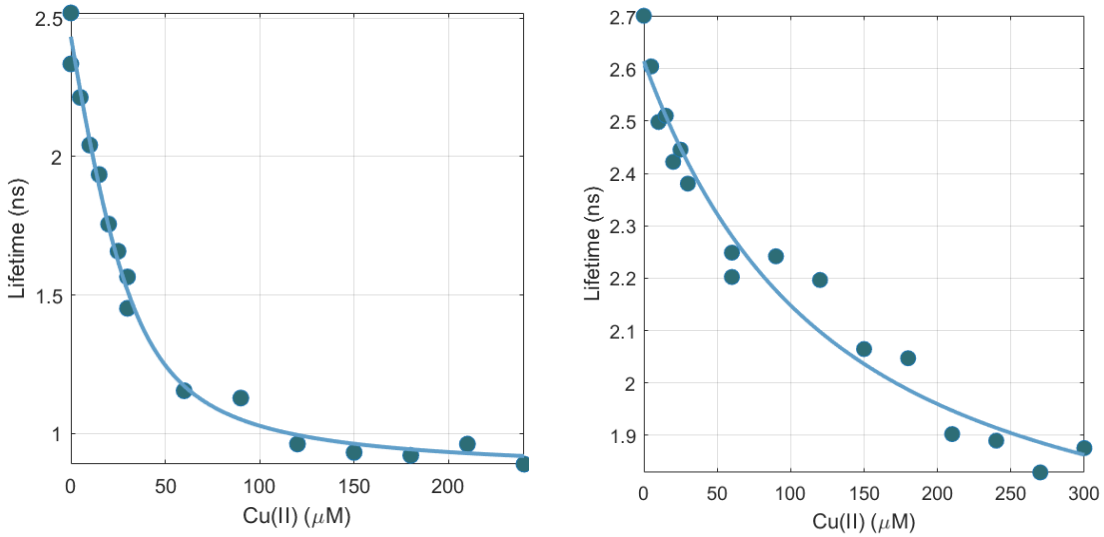

Figure 3.8 Variation in Nsp1-CT_{33} W161 effective fluorescence decay time (Lifetime (ns)) as a function of Cu(II) concentration. On the left is the Nsp1-CT_{33} and on the right is Nsp1-CT_{33} H165A. Solid line is a fit to a single binding site model with K_d = 9.7μM ([Nsp1-CT_{33}] = 30μM, pH 6.5, MOPS 20 mM, 30% glycerol) and K_d = 106μM ([Nsp1-CT_{33} H165A] = 30μM, pH 6.5, MOPS 20 mM, 30% glycerol).

Another possible explanation for the W161 quenching rate constant is that it represents the rate of intrachain diffusion, where the Cu(II)-bound residue transiently interacts with *W161. The quenching rate constant for the peptide-bound Cu(II) complex (~5×10^8 s^{-1}) is at least an order of magnitude higher than the fastest reported rates of tertiary contact formation in disordered polypeptides.[26–29]

To further investigate the interactions between Cu(II) and the peptide, electron paramagnetic resonance (EPR) spectroscopy serves as a valuable tool. The Cu(II) ion, with its $3d^9$ electron configuration and S=1/2, is paramagnetic and thus detectable by EPR. This property enables the characterization of Cu(II) metal complexes, providing insights into their electronic structure and coordination environment.[30]

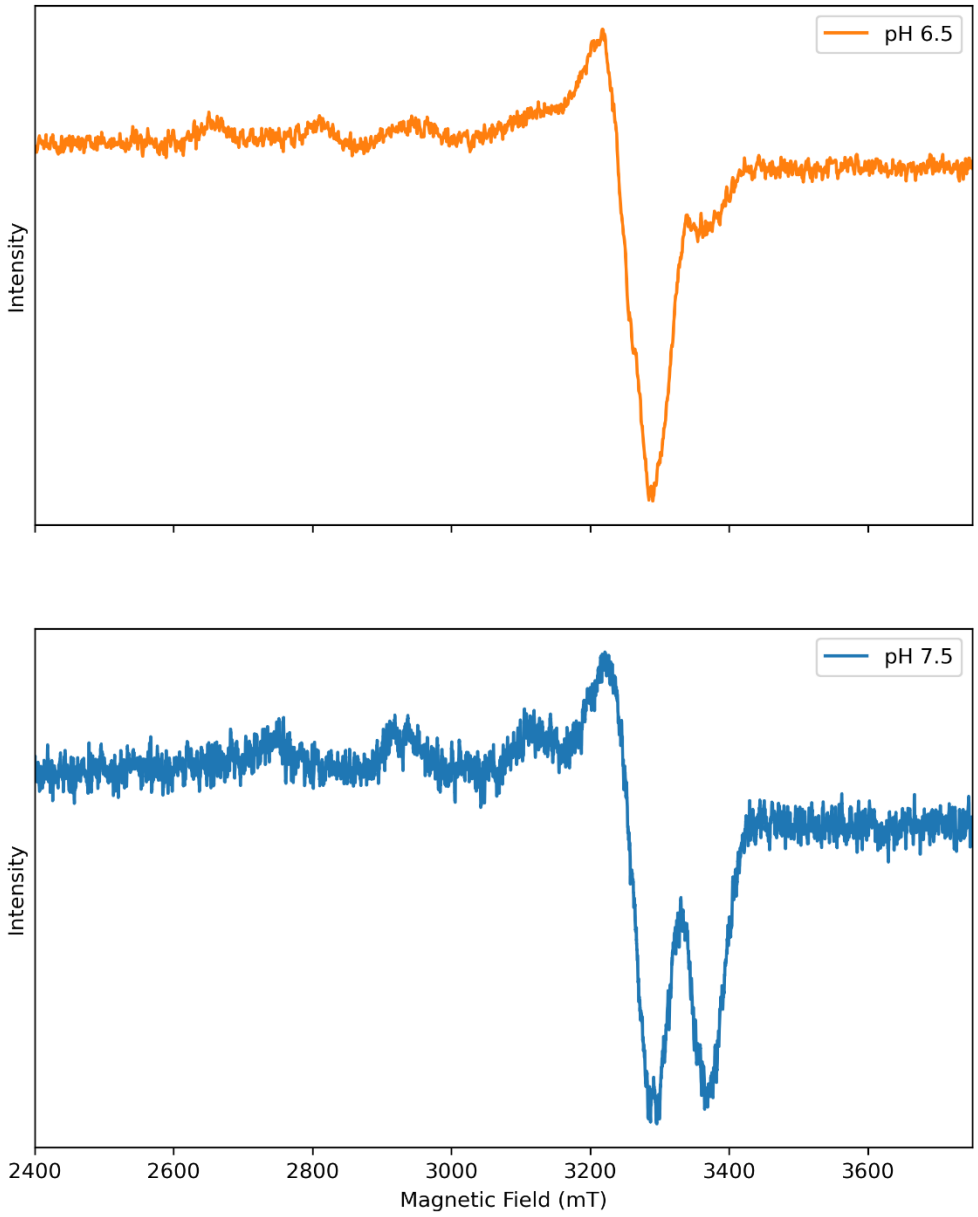

Figure 3.9 X-band EPR spectra of ([Cu] = [Nsp1-CT] = 100 µM, MOPS 20 mM, 30% glycerol) at pH 6.5 (orange) and 7.5 (blue).

EPR spectroscopy offers a sensitive probe of the Cu(II) coordination environment. The continuous-wave X-band spectrum of Nsp1-CT (100 µM) in the presence of one equivalent of Cu(II) at pH 6.5 reveals a predominant species with near-axial Cu(II) coordination (g_1 = 2.060, g_2 = 2.058, g_3 = 2.332). The hyperfine coupling constant for the low-field resonance (g_3) is A_3 = 457 MHz. Notably, the spectrum shows no evidence of unbound aquo Cu(II), indicating that under these conditions, Cu(II) binds to a single Nsp1-CT_{33} peptide (Figure 3.9).

At pH 7.5, the Cu(II) EPR spectrum exhibits increased rhombicity, with g-values shifting to higher magnetic fields (g_1 = 2.040, g_2 = 2.067, g_3 = 2.219; A_3 = 583 MHz), suggesting a less symmetric yet stronger ligand field around Cu(II) (Figure 3.9).

To interpret these spectral changes, Peisach-Blumberg correlations were applied. Cu(II) complexes typically adopt a distorted octahedral geometry, where four ligands form a strong equatorial plane, while two axial ligands are less tightly bound. These axial ligands contribute minimally to the magnetic and optical properties of the complex.[31]

In Cu(II) complexes with a 2N2O coordination, $g_{||}$ values tend to lie between 2.2 and 2.3 generally range from 2.2 to 2.3, depending on the overall charge, closer to 2.2 for a 2^- species and nearer to 2.3 for a 2^+ species. The corresponding $A_{||}$ values range between 450 MHz and 600 MHz, increasing toward 600 MHz for negatively charged species and decreasing toward 450 MHz for positively charged species.

When Cu(II) is coordinated by three oxygen and one nitrogen (3O1N), the complex tends to carry a positive charge, with $g_{||}$ values shifting higher (~2.2–2.4) and $A_{||}$ values decreasing (~374–450 MHz) relative to the 2N2O case. This pattern is observed for Nsp1-CT_{33} at pH 6.5, where $A_{||}$ =457MHz and $g_{||}$=2.332, supporting a 3O1N coordination mode.

In contrast, when Cu(II) is bound to three nitrogens and one oxygen (3N1O), the charge varies, but the $A_{||}$ values remain similar to those in 2N2O systems. However, $g_{||}$ shifts between 2.15 and 2.3, increasing with more positive charge. This pattern aligns with Nsp1-CT33 at pH 7.5, where $A_{||}$=583MHz and $g_{||}$=2.219, indicating a 3N1O coordination environment.

To further analyze the coordination of the Cu(II) peptide complex, pulsed EPR techniques were employed. ENDOR (Electron Nuclear Double Resonance) enhances the resolution of EPR by directly probing hyperfine interactions between the unpaired electron and nearby nuclear spins. This technique is particularly effective for studying Cu(II) complexes as it provides detailed information about the local ligand environment. It gives insights into the identity, coupling strengths, and spatial arrangement of coordinating atoms such as nitrogen and oxygen. ENDOR resolves the hyperfine and quadrupolar interactions enabling precise characterization of the electronic and geometric structure of the complex.

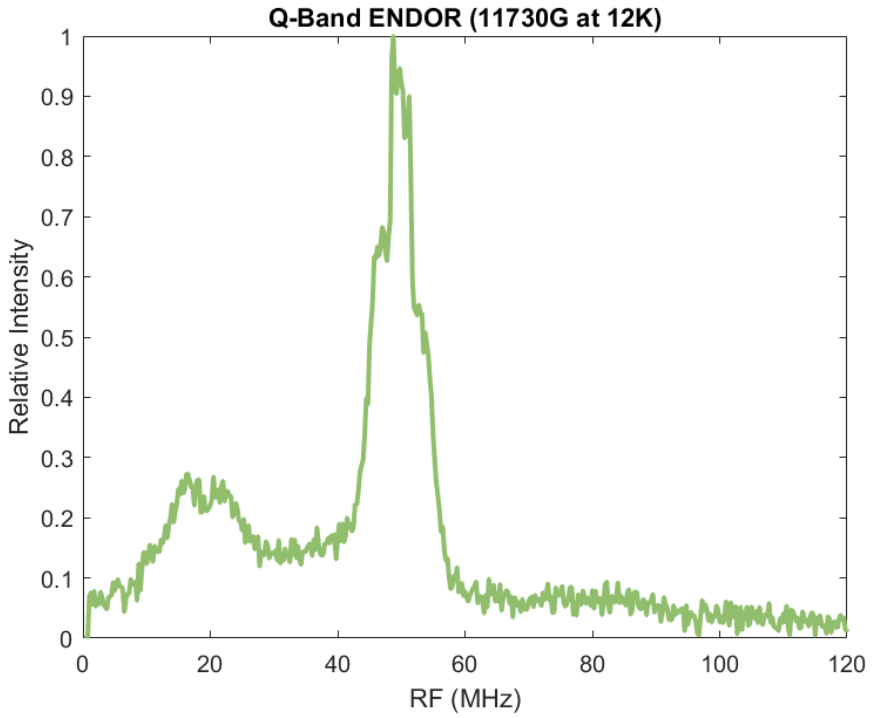

Figure 3.10 The Q-Band ENDOR spectrum was collected of Cu(II):Nsp1-CT_{33} ([Cu] = [Nsp1-CT] = 100 μM, MOPS 20 mM, 30% glycerol) at pH 7.5.

The ENDOR spectrum (Figure 3.10) exhibits two prominent features: a strong peak near 45 MHz and a lower-frequency feature in the 10–30 MHz range. At Q-band and a magnetic field of 11,730 G, the Larmor frequency of protons (^{1}H) is approximately 45 MHz. This suggests that proton nuclei are strongly coupled to the unpaired electron of Cu(II), likely originating from water, hydroxyl groups, or hydrogen-containing ligands. In this case, the observed proton coupling arises from the use of water as a solvent. [32,33]

Additionally, the ENDOR spectrum displays two peaks split by the Larmor frequency of nitrogen, centered around 20 MHz. These lower-frequency features likely correspond to nitrogen nuclei interacting with the Cu(II) center. Since ^{14}N has a nuclear quadrupolar moment, its signals are broader and weaker compared to those of protons, explaining the reduced intensity observed in the spectrum. The 3–4 MHz spacing likely arises from weakly coupled nitrogen ligands,

HYSCORE (Hyperfine Sublevel Correlation Spectroscopy) is a two-dimensional EPR method that enhances the detection of weak hyperfine and quadrupolar interactions by correlating

nuclear frequencies. This technique is particularly valuable for Cu(II) complexes, as it provides detailed information about nearby nuclei. It helps resolve overlapping signals that may be difficult to distinguish in one-dimensional spectra. It offers improved spectral resolution and sensitivity, which enables a more comprehensive characterization of the electronic structure and ligand interactions.

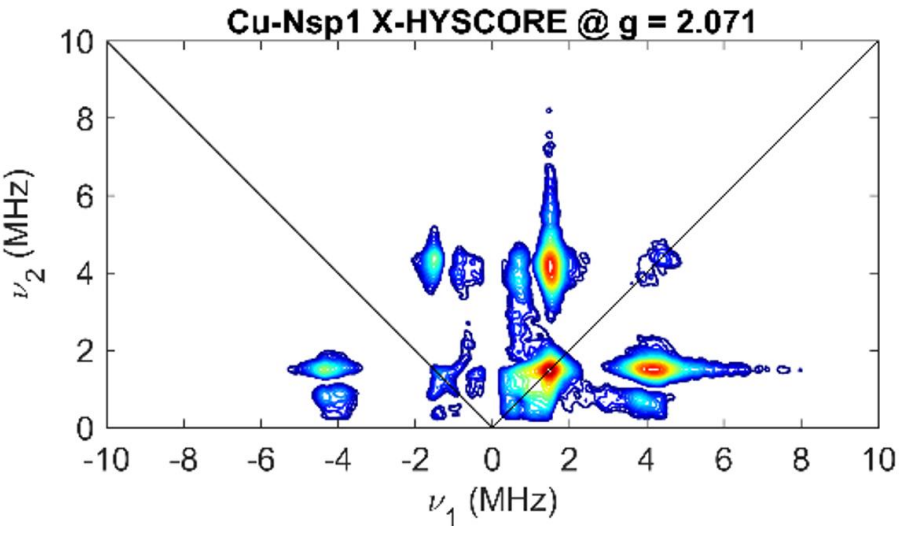

Figure 3.11 The HYSCORE spectrum was collected of Cu(II):Nsp1-CT_{33} ([Cu] = [Nsp1-CT] = 100 μM, MOPS 20 mM, 30% glycerol) at pH 7.5.

The collected HYSCORE spectra collected at g=2.071 (Figure 3.11), reveals a well-defined cross-peak in the low frequency region, this is indicative of hyperfine interactions with nearby nuclei. The presence of the peaks in the 2-4MHz range suggests coupling to nitrogen nuclei consistent with coordination from an imidazole group of a histidine residue. The cross- peaks are a result of the nuclear quadrupole interaction of nitrogen further confirming the involvement of an imidazole nitrogen Cu(II) coordination.

The characteristic splitting pattern observed in the (ν_1, ν_2) quadrants aligns with previously reported spectra of Cu(II)-imidazole complexes. The distinct correlation peaks at the ±2 MHz and the a symmetry of the peak intensity suggest a nitrogen environment typical of histidine coordination.[34]

To narrow down the coordination of the Cu(II) with H165, a smaller decapeptide was employed, Nsp1-CT_{10}. This was done so that computational modelling could be used and compared to experimental results.

W161 was important for reporting on Cu(II) binding to Nsp1-CT_{33}. To further identify potential inner-sphere ligands in the intrinsically disordered protein region, the W161 fluorescence was monitored in the presence of Cu(II) in Nsp1-CT_{10}. The average W161 fluorescence decay time was determined by integrating a normalized W161 fluorescence decay curve. In the absence of Cu(II), Nsp1-CT_{10} has a lifetime of 2.1ns, after the peptide is fully bound to Cu(II) the lifetime decreases to 0.95ns. Dissociations constants of the Cu(II) from the Cu-bound peptide were calculated by measuring the observed lifetime as a function of Cu(II). The dissociation constants can be found in Table 3.1 and noticeably vary at different pH.

pH	**6.5**	**7.5**	**8.5**
K_d	10.1	5.05	<1

Table 3.3 Aquo-Cu(II) dissociation constants extracted from W161 fluorescence of Nsp1-CT_{10}.

Similar to the studies conducted with Nsp1-CT_{33} and Cu(II), EPR can also be used to gain insights on the coordination. The X-band EPR of Nsp1-CT_{10} (100 μM, 77 K) in the presence of 1 equivalent of Cu(II) at pH 6.5 can be modeled with two nearly axial Cu(II) spin systems (Spin 1, 66%: g_1 = 2.044; g_2 = 2.080; g_3 = 2.401; A_3 = 303 MHz. Spin 2, 33%: g_1 = 2.054; g_2 = 2.062; g_3 = 2.231; A_3 = 581 MHz). The spectra (Figure 3.12) recorded at pH 7.5 and 8.5 are nearly identical consistent with a single S = ½ spin center, with somewhat greater rhombic symmetry (g_1 = 2.0426, g_2 = 2.068, g_3 = 2.219, A_3 = 564MHz). Using the Peisach-Blumberg correlation it suggest that at pH 6.5 the Cu(II) coordination is to one nitrogen and three oxygens for the dominant spin system. For the pH 7.5 and pH 8.5 spectra, the g_3 is consistent with a stronger ligand field indicating that most likely there are more nitrogens coordinating to the Cu(II).[31]

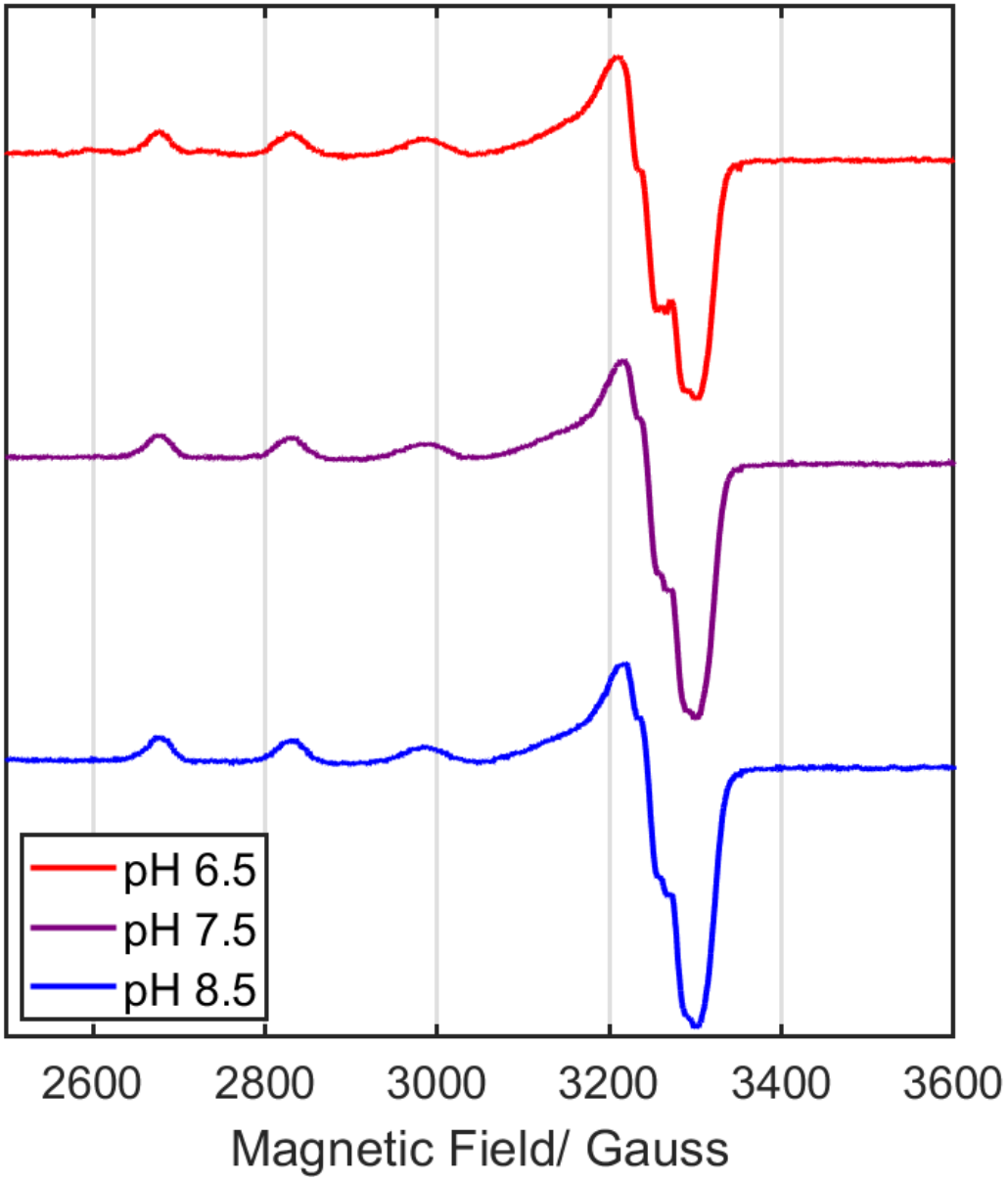

Figure 3.12 X-band EPR spectra of Cu(II): Nsp1-CT_{10} ([Cu]=[Nsp1-CT_{10}] = 100 μM, MOPS 20 mM, 30% glycerol, 77 K).

To further confirm the coordination of the inner sphere ligands quantum mechanical calculations were employed. This work was done in collaboration with Professor William A. Goddard and the calculations were carried out by Moon Young Yang. The Cu(II)-peptide structures were modeled with one or two explicit water molecules depending on the pH of the system. The optimized structures can be seen in Figure 3.13. Conducting calculations on the full

Nsp1-CT peptide sequence would be extremely costly therefore the modeled structures only include residues that form direct contact with Cu(II) and/or hydrogen networks with solvents.

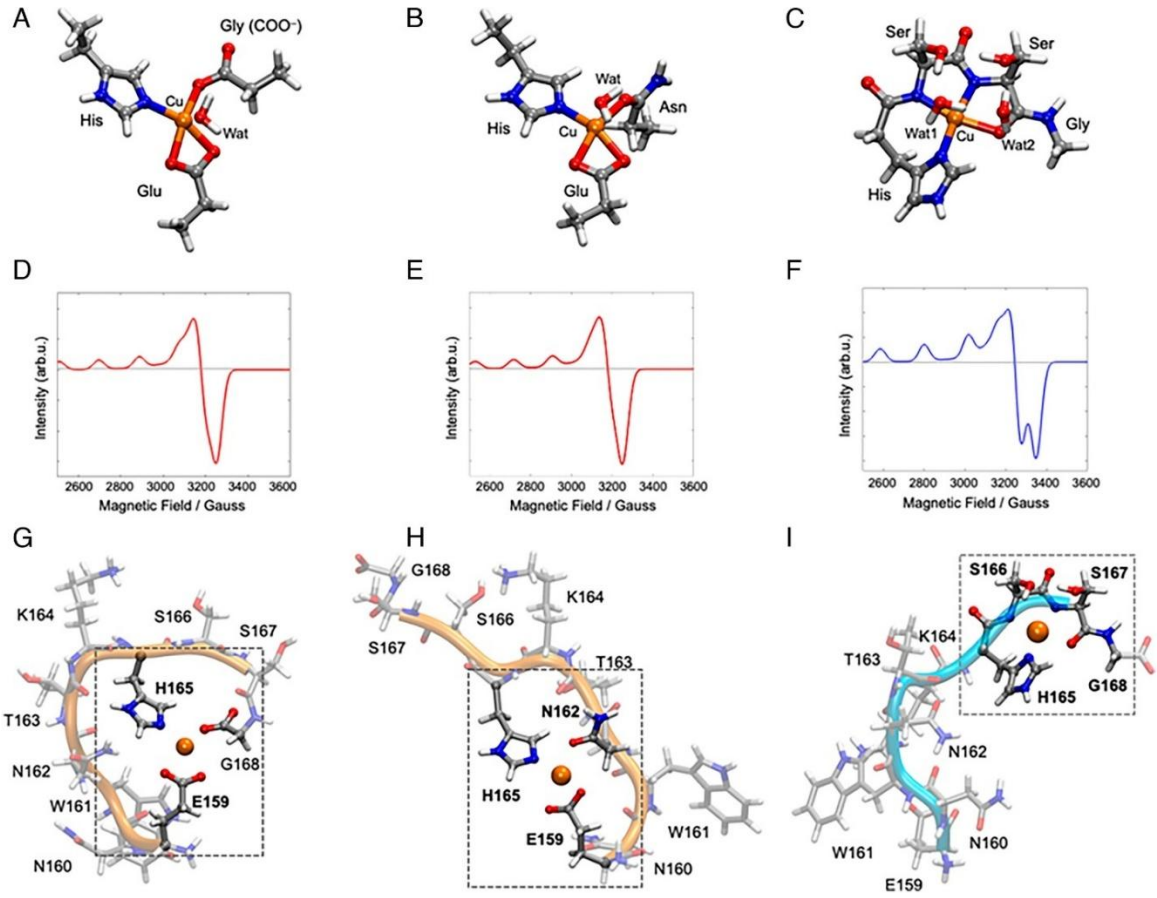

Figure 3.13 Computational models of the Cu(II) coordination environment at (A and B) pH 6.5 and (C) pH 8.5, and (D–F) their simulated EPR spectra, respectively. (G–I) Model structures of Cu(II):Nsp1-CT_{10} constructed based on QM-optimized active sites (A–C), where. Water molecules were omitted and the nonactive sites were shown with transparency for clarity. Thick orange and cyan lines represent the backbone of the peptide.

From the calculations there are two structural models that are consistent with prominent components of the experimental spectrum measure at pH 6.5 (Figure 3.12). Both models include Cu(II) coordinated to one nitrogen and three oxygen atoms from the peptide. Normally, the N-terminal of the peptide might bind to Cu(II) however the peptide is N-terminally acetylated. In one model the Cu(II) is coordinated to the imidazole of H165 and the oxygen donors from E159 and the terminal carboxylate of G168, along with one water molecule. In the other model, one of the O-donors is from N162 instead of the terminal carboxylate of G168. The calculated

g-tensor components for the first model and second model of the pH 6.5 complex are also in reasonable agreement with the experimental results (model 1: $g_1 = 2.103$, $g_2 = 2.109$, $g_3 = 2.403$/ model 2: $g_1 = 2.100$, $g_2 = 2.114$, $g_3 = 2.387$).

If Cu(II)-peptide is compared to the prion octarepeat it is observed that it contains a similar HGGG sequence, compared to HSSG.[35] There is a similar coordination of inner-sphere ligands at pH 7.5 and 8.5 when compared to the prion octarepeat. Cu(II) is coordinated to the imidazole in the H165 and the amide nitrogens in S166 and S167. With the inclusion of an axial water molecule, the coordination environment is square pyramidal. The S166 and S167 form a hydrogen bond network with the two water molecules. In the calculated spectrum the g-tensor components are ($g_1 = 2.064$, $g_2 = 2.085$, $g_3 = 2.307$), which are in reasonable agreement with the experimental results.

Copper(II) Complexes for Binding to Nsp1

To identify a system with stronger binding affinity than aquo copper(II), attention was directed toward copper(II) complexes. Two complexes were selected for investigation: copper(II) iminodiacetate (Cu-IDA) and copper(II) histidinate. Iminodiacetate (IDA) is a tridentate ligand that forms a stable 1:1 complex with Cu(II) ($K_{Cu|IDA} = 10^{10.6}$), leaving three coordination sites available for additional interactions, such as binding to Nsp1.[36]

Using the Nsp1-CT_{33} peptide, it was observed that Cu-IDA effectively quenched tryptophan fluorescence, yielding a dissociation constant K_d=2.82 μM at pH 7.5 (Figure 3.14). This represents a significantly tighter binding interaction compared to aquo copper(II), which exhibited a K_d= 7.67 μM under the same conditions. These results suggest that pre-coordination with IDA enhances copper's binding affinity toward Nsp1, likely by stabilizing the metal center while maintaining available sites for peptide coordination.

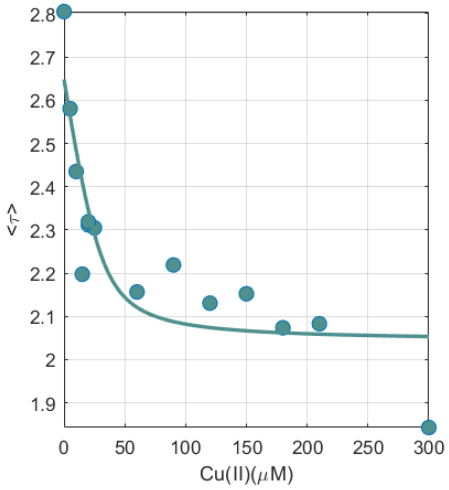

Figure 3.14 Average tryptophan fluorescence lifetimes as a function of increasing Cu-IDA concentration. [Nsp1-CT_{33}]=30μM, samples were made in MOPS buffer (20mM, pH 7.5).

To further characterize the Cu-IDA complex and its interaction with Nsp1-CT_{33}, electron paramagnetic resonance (EPR) spectroscopy was employed to monitor changes in the copper coordination environment upon peptide binding. The resulting spectra, both for Cu-IDA alone and in the presence of peptide, are shown in Figure 3.15.

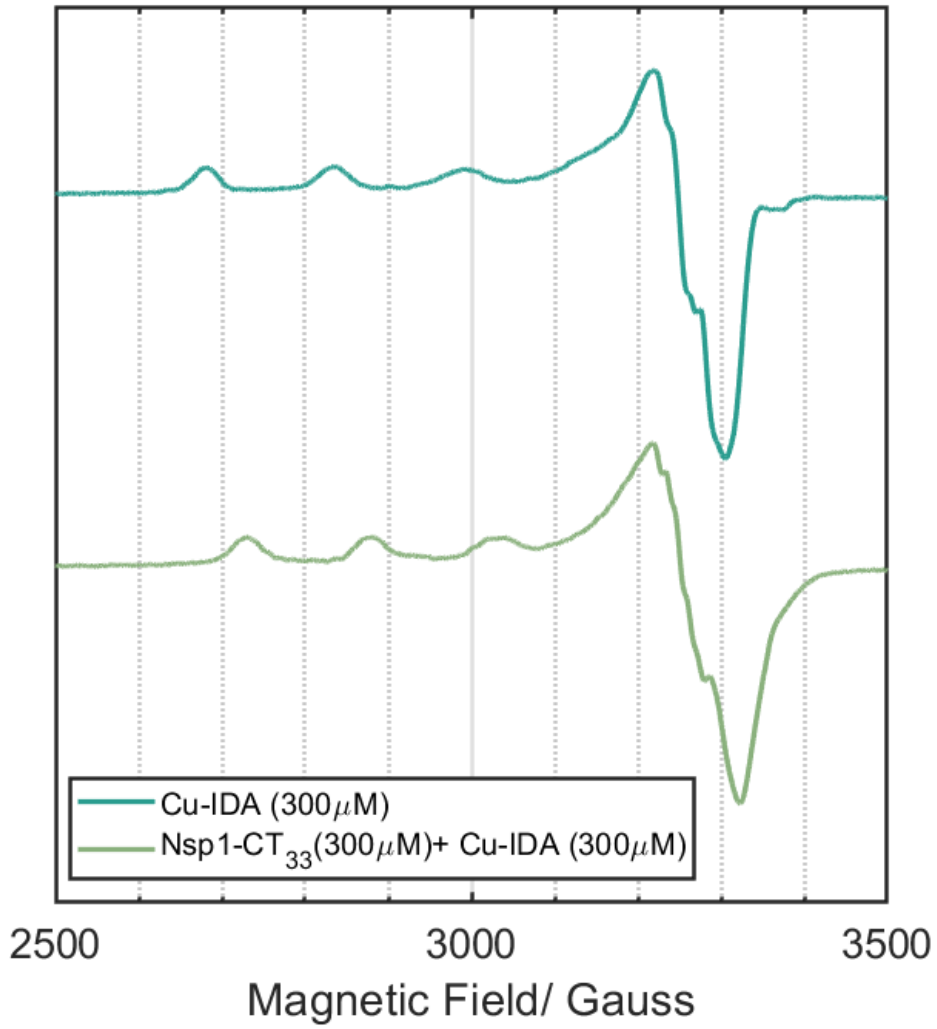

Figure 3.15 EPR spectrum of Cu-IDA and Nsp1-CT_{33} with Cu-IDA. Samples were made at 300uM concentration in MOPS buffer (20mM pH7.5) with 30% glycerol. Measurements were taken at 77K.

Several notable changes were observed in the EPR spectrum upon the addition of Nsp1-CT_{33} to the Cu-IDA complex. In the absence of peptide, the Cu-IDA complex exhibits parameters of $g_1 = g_2 = 2.06$, $g_3 = 2.31$, $A_1 = 12$ MHz, $A_2 = 55$ MHz, and $A_3 = 489$ MHz. Upon addition of one equivalent of Nsp1-CT33, the spectrum shifts to $g_1 = g_2 = 2.06$, $g_3 = 2.26$, $A_1 = -14$ MHz, $A_2 = 74$ MHz, and $A_3 = 500$ MHz. These shifts include a decrease in g_3 and an increase in A_3, along with broadening of the perpendicular (g_1/g_2) features, consistent with a strengthening of the equatorial ligand field around the copper(II) center.

These spectral changes suggest direct coordination of donor atoms from the peptide, likely involving imidazole nitrogens, backbone amide groups, or carboxylates, which displace solvent molecules in the coordination sphere. The resulting inner-sphere complex introduces enhanced equatorial bonding interactions and a slight perturbation of the axial symmetry. Together, the EPR data supports a model in which the peptide significantly alters the local geometry of the Cu(II) center through direct coordination. In chapter 5, we further explore this compound and test if it can inhibit Nsp1.

The second complex investigated was copper(II) histidinate, a compound currently used in the treatment of Menkes disease, a genetic disorder caused by mutations in the ATP7A copper transport gene, resulting in systemic copper deficiency.[37] Given its established clinical safety profile, copper(II) histidinate was selected to evaluate its potential for coordinating with Nsp1. For these studies, the Nsp1-CT_{10} peptide was used, and tryptophan fluorescence quenching was monitored across increasing concentrations of copper(II) histidinate (Figure 3.16). The measured dissociation constant K_d=30 μM at pH 7.5 , indicating significantly weaker binding compared to aquo copper(II), which exhibited a K_d=5 μM at pH 7.5. Despite its lower binding affinity, copper(II) histidinate was retained for further evaluation as a potential Nsp1 inhibitor due to its clinical relevance; these studies are discussed in Chapter 5.

These results highlight contrasting behaviors between the two copper(II) complexes: Cu-IDA demonstrated enhanced binding affinity relative to aquo copper(II), while copper(II) histidinate showed reduced affinity. This comparison demonstrates how ligand environment affects copper's interaction with Nsp1-derived peptides and provides a foundation for selecting metal-based candidates for functional inhibition studies.

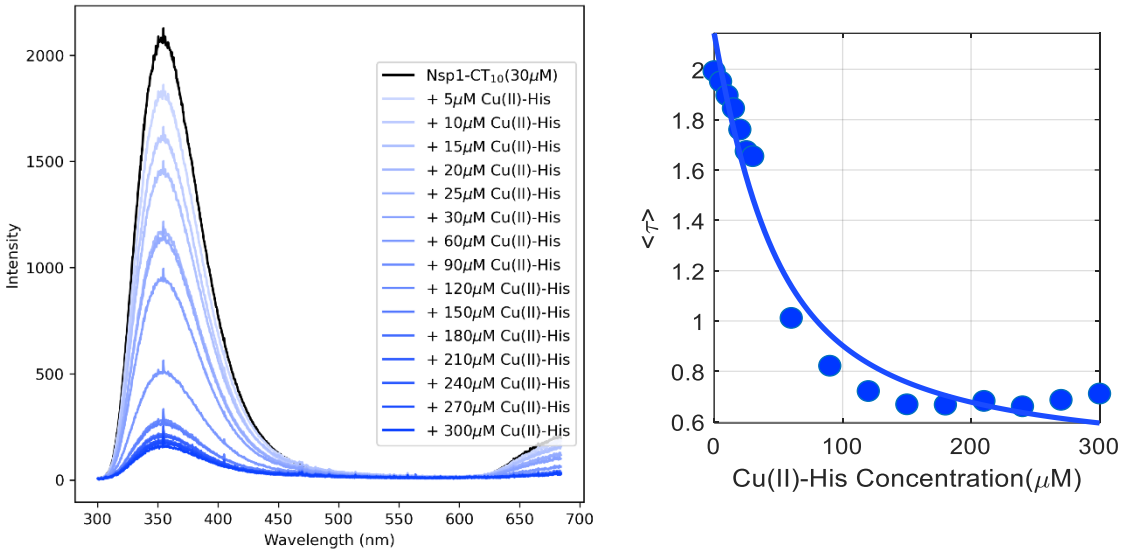

Figure 3.16 On the left is the steady state tryptophan fluorescence quenching of Nsp1-CT_{10} upon addition of Copper(II)Histidinate (Cu(II)-His) and on the right is the change in the average lifetime as a function of concentration of Cu(II)-His. Measurements were done in MOPS buffer (20mM, pH 7.5).

Summary and Outlook

These studies demonstrate that Cu(II) coordinates to the C-terminal region of Nsp1, specifically targeting H165. The coordination environment is pH-dependent, shifting from a 3O1N coordination at lower pH to a 1O3N coordination at higher pH. At pH ≥ 7.5, both experimental and computational analyses suggest that backbone amide chelation further stabilizes the complex.

In addition to aquo copper(II), investigations into copper(II) complexes revealed that ligand pre-coordination significantly influences binding affinity toward Nsp1 peptides. The Cu-IDA complex exhibited enhanced binding compared to aquo Cu(II), while copper(II) histidinate showed weaker interaction, despite its clinical relevance. These results highlight the importance of ligand design in modulating metal–protein interactions and suggest that copper(II) complexes could improve specificity and stability in targeting Nsp1.

Overall, these findings provide a foundation for the rational development of metal-based drug candidates with optimized binding properties for the C- terminal of Nsp1. By leveraging both the flexibility of intrinsically disordered regions and the tunable coordination chemistry of

copper complexes, this work opens avenues for novel therapeutic strategies aimed at disrupting Nsp1 function in SARS-CoV-2.

Supplementary Information

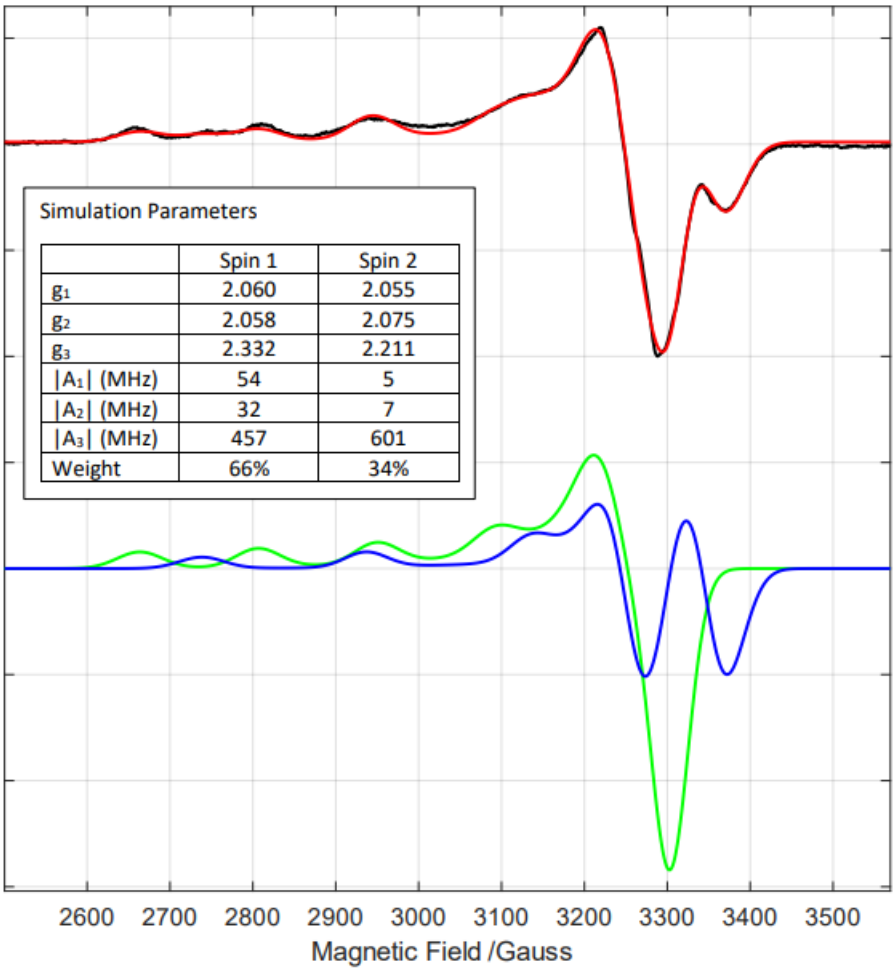

Figure S3.1 Cu(II):Nsp1-CT_{33} ([Cu] = [Nsp1-CT_{33}] = 100 μM, MOPS 20 mM, pH 6.5, 30% glycerol) X-band EPR spectrum (black) and simulation (red). Individual simulation components are shown in green (Spin 1) and blue (Spin 2). Acquisition parameters: MW frequency = 9.391-9.394 GHz, MW power = 2.2 mW, modulation amplitude = 8 Gauss, conversion time = 10.72 ms.

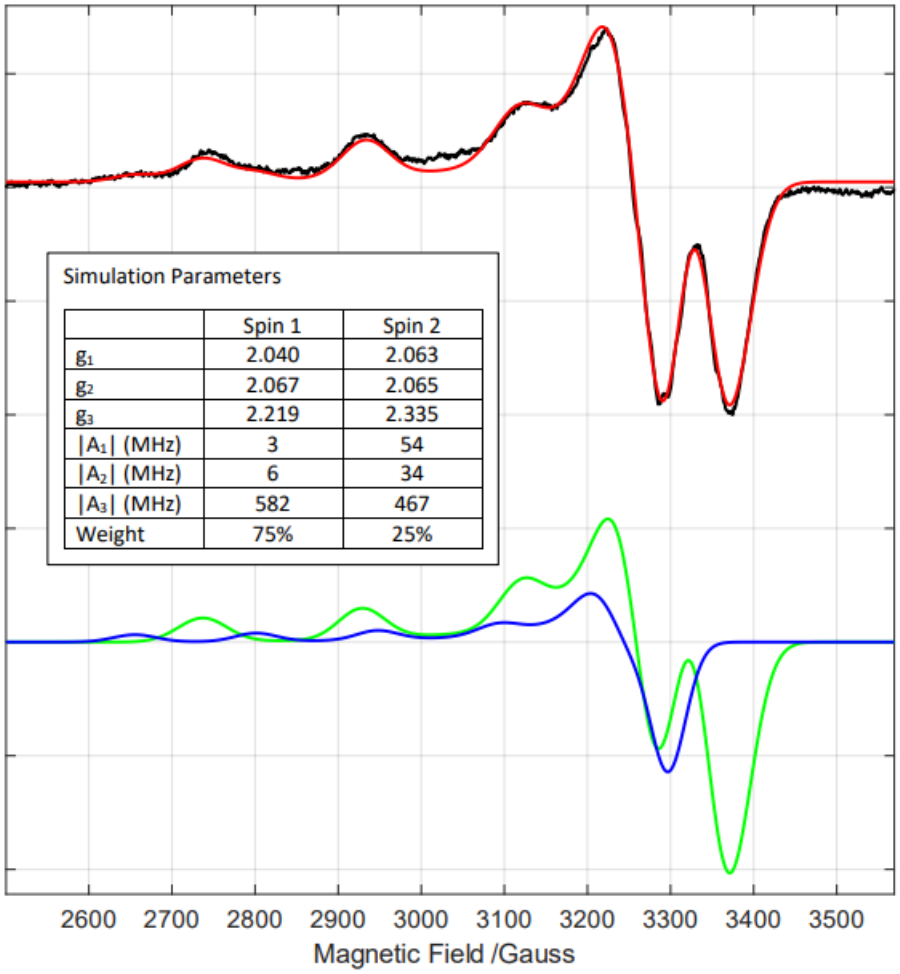

Figure S3.2 Cu(II):Nsp1-CT_{33} ([Cu] = [Nsp1-CT_{33}] = 100 μM, MOPS 20 mM, pH 7.5, 30% glycerol) X-band EPR spectrum (black) and simulation (red). Individual simulation components are shown in green (Spin 1) and blue (Spin 2). Acquisition parameters: MW frequency = 9.391-9.394 GHz, MW power = 2.2 mW, modulation amplitude = 8 Gauss, conversion time = 10.72 ms.

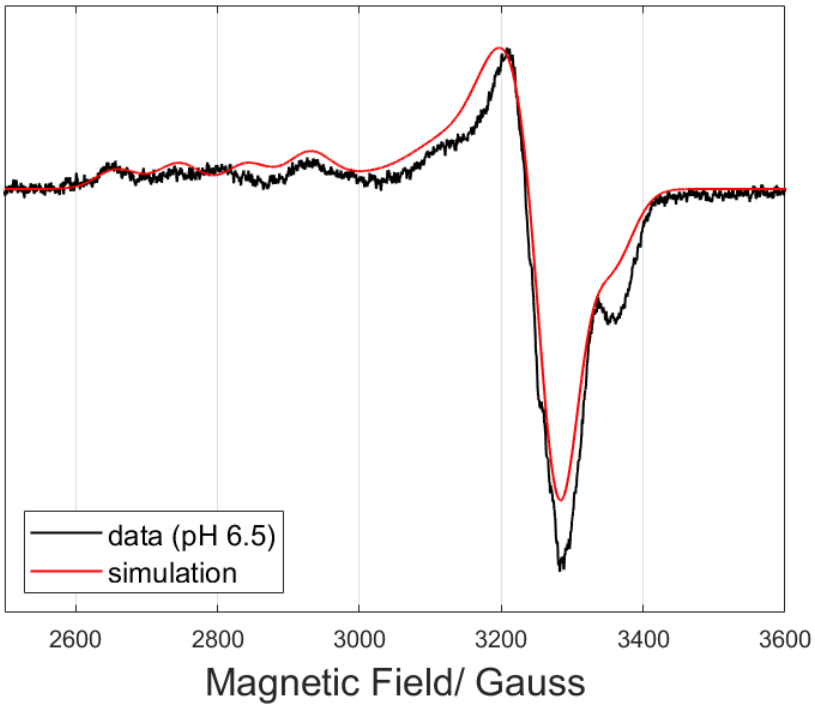

Figure S3.3 EasySpin simulation of the pH 6.5 Cu(II):Nsp1-CT_{10} EPR spectrum.

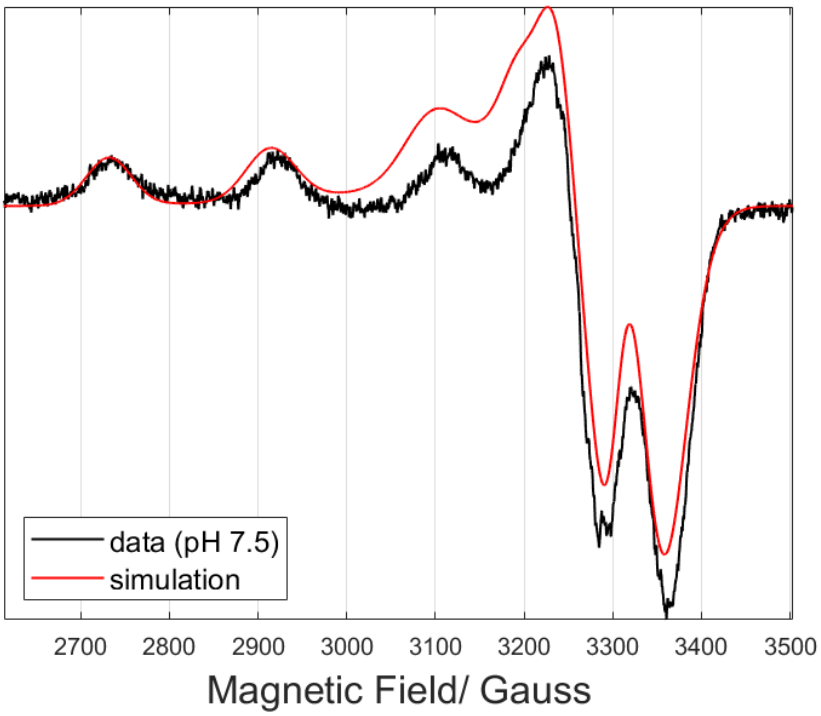

Figure S3.4 EasySpin simulation of the pH 7.5 Cu(II):Nsp1-CT_{10} EPR spectrum.

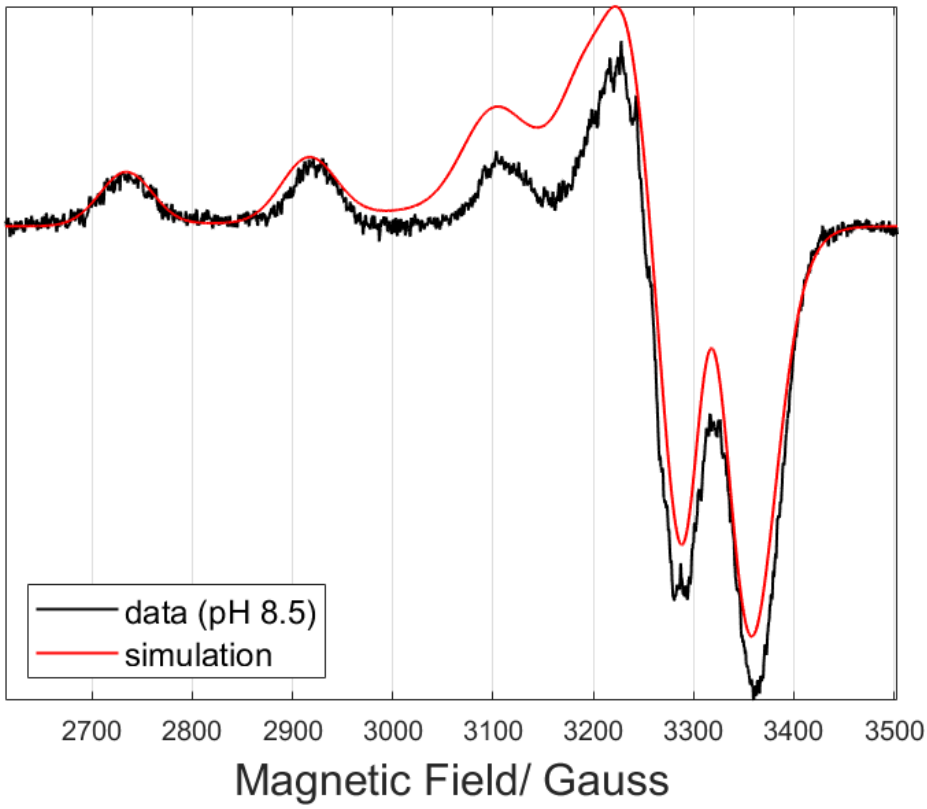

Figure S3.5 EasySpin simulation of the pH 8.5 Cu(II):Nsp1-CT_{10} EPR spectrum.

Table S3.1 Cu(II):Nsp1-CT_{10} EasySpin EPR fitting parameters.

pH	*6.5*		*7.5*	*8.5*
Spin	Spin 1	Spin 2	Spin 1	Spin 1
Population (%)	66	33	100	100
g_1	2.044	2.054	2.075	2.075
g_2	2.080	2.062	2.043	2.043
g_3	2.401	2.231	2.234	2.230
Linewidth (mT)	6	6	3	4
A_1 *(MHz)*	26	-7	86	85
A_2 *(MHz)*	46	-7	-5	4
A_3 *(MHz)*	303	581	554	553
g_1*-strain*	0.007	0.004	0	0
g_2*-strain*	0.005	0.012	0	0
g_3*-strain*	0.006	0.046	0.046	0.042
A_1*-strain*			191	217
A_2*-strain*			0	0
A_3*-strain*			37	23

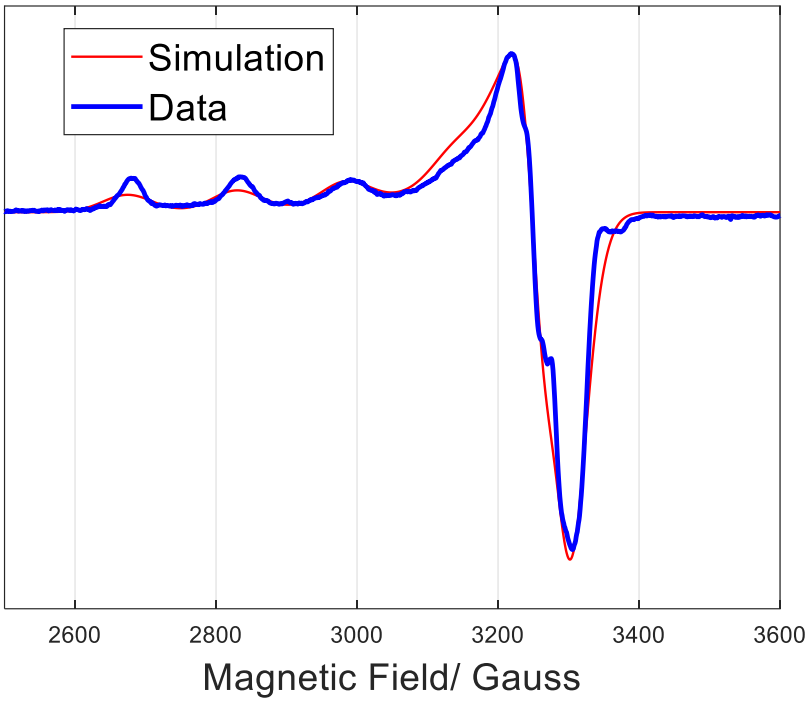

Figure S3.6 EasySpin simulation of the pH 7.5 Cu(II)IDA EPR spectrum.

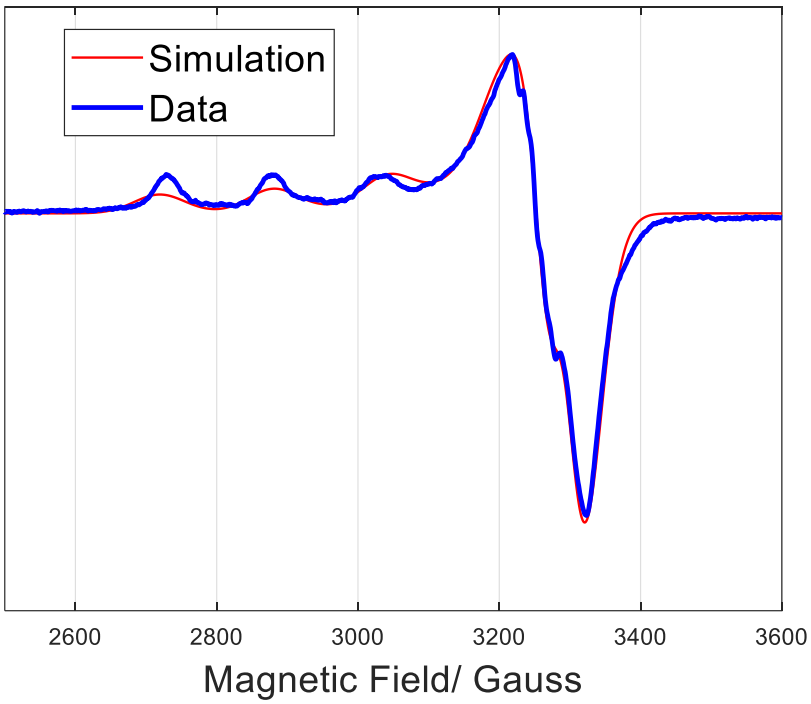

Figure S3.7 EasySpin simulation of the pH 7.5 Cu(II)IDA:Nsp1-CT_{33} EPR spectrum.

Table S3.2 Cu(II)IDA:Nsp1-CT_{33} EasySpin EPR fitting parameters for experiments done at pH 7.5.

	Cu(II)IDA	*Nsp1-CT_{33}-Cu(II)IDA*
g_1	2.063	2.061
g_2	2.062	2.057
g_3	2.309	2.267
A_1	12.005	-14.222
A_2	55.156	74.236
A_3	488.971	500.328

References

(1) Tokuriki, N.; Oldfield, C. J.; Uversky, V. N.; Berezovsky, I. N.; Tawfik, D. S. Do Viral Proteins Possess Unique Biophysical Features? *Trends Biochem Sci* **2009**, *34* (2), 53–59. https://doi.org/10.1016/j.tibs.2008.10.009.

(2) Solomon, E. I.; Heppner, D. E.; Johnston, E. M.; Ginsbach, J. W.; Cirera, J.; Qayyum, M.; Kieber-Emmons, M. T.; Kjaergaard, C. H.; Hadt, R. G.; Tian, L. Copper Active Sites in Biology. *Chem Rev* **2014**, *114* (7), 3659–3853. https://doi.org/10.1021/cr400327t.

(3) Festa, R. A.; Thiele, D. J. Copper: An Essential Metal in Biology. *Curr Biol* **2011**, *21* (21), R877-883. https://doi.org/10.1016/j.cub.2011.09.040.

(4) Irving, H.; Williams, R. J. P. 637. The Stability of Transition-Metal Complexes. *J Chem Soc* **1953**, 3192. https://doi.org/10.1039/jr9530003192.

(5) Prohaska, J. R. Role of Copper Transporters in Copper Homeostasis. *Am J Clin Nutr* **2008**, *88* (3), 826S-9S. https://doi.org/10.1093/ajcn/88.3.826S.

(6) Ala, A.; Walker, A. P.; Ashkan, K.; Dooley, J. S.; Schilsky, M. L. Wilson's Disease. *The Lancet* **2007**, *369* (9559), 397–408. https://doi.org/10.1016/S0140-6736(07)60196-2.

(7) Al-Chalabi, M.; Fathy, A.; Kelley, A.; Selim, L. A.-M.; Ramadan, A.; Noor, M.; Lakhani, S.; Mahfooz, N. Menkes Disease Treatment with Copper Chloride: Case Report. *Med Rep* **2023**, *1*, 100001. https://doi.org/10.1016/j.hmedic.2023.100001.

(8) Husain, N.; Mahmood, R. Copper(II) Generates ROS and RNS, Impairs Antioxidant System and Damages Membrane and DNA in Human Blood Cells. *Environ Sci Pollut Res Int* **2019**, *26* (20), 20654–20668. https://doi.org/10.1007/s11356-019-05345-1.

(9) Cervantes-Cervantes, M. P.; Calderón-Salinas, J. V.; Albores, A.; Muñoz-Sánchez, J. L. Copper Increases the Damage to DNA and Proteins Caused by Reactive Oxygen Species. *Biol Trace Elem Res* **2005**, *103* (3), 229–248. https://doi.org/10.1385/BTER:103:3:229.

(10) Djoko, K. Y.; Ong, C. Y.; Walker, M. J.; McEwan, A. G. The Role of Copper and Zinc Toxicity in Innate Immune Defense against Bacterial Pathogens. *J Biol Chem* **2015**, *290* (31), 18954–18961. https://doi.org/10.1074/jbc.R115.647099.

(11) De Romaña, D. L.; Olivares, M.; Uauy, R.; Araya, M. Risks and Benefits of Copper in Light of New Insights of Copper Homeostasis. *J Trace Elem Med Biol* **2011**, *25* (1), 3–13. https://doi.org/10.1016/j.jtemb.2010.11.004.

(12) Dollwet, H. H. A.; Sorenson, J. R. J. Hisotric Uses of Copper Compounds in Medicine. *J Trace Elem Med Biol 2*, 80–87.

(13) Walusinski, O. The Scientific Illusion of Victor Burq (1822–1884). *Eur Neurol* **2018**, *79* (3–4), 135–149. https://doi.org/10.1159/000487667.

(14) Noyce, J. O.; Michels, H.; Keevil, C. W. Inactivation of Influenza A Virus on Copper versus Stainless Steel Surfaces. *Appl Environ Microbiol* **2007**, *73* (8), 2748–2750. https://doi.org/10.1128/AEM.01139-06.

(15) Poggio, C.; Colombo, M.; Arciola, C. R.; Greggi, T.; Scribante, A.; Dagna, A. Copper-Alloy Surfaces and Cleaning Regimens against the Spread of SARS-CoV-2 in Dentistry and Orthopedics. From Fomites to Anti-Infective Nanocoatings. *Materials* **2020**, *13* (15), 3244. https://doi.org/10.3390/ma13153244.

(16) Weder, J. E.; Dillon, C. T.; Hambley, T. W.; Kennedy, B. J.; Lay, P. A.; Biffin, J. R.; Regtop, H. L.; Davies, N. M. Copper Complexes of Non-Steroidal Anti-Inflammatory Drugs: An Opportunity yet to Be Realized. *Coord Chem Rev* **2002**, *232* (1–2), 95–126. https://doi.org/10.1016/S0010-8545(02)00086-3.

(17) Tisato, F.; Marzano, C.; Porchia, M.; Pellei, M.; Santini, C. Copper in Diseases and Treatments, and Copper-based Anticancer Strategies. *Med Res Rev* **2010**, *30* (4), 708–749. https://doi.org/10.1002/med.20174.

(18) Shiraki, K.; Nishikawa, K.; Goto, Y. Trifluoroethanol-Induced Stabilization of the α-Helical Structure of β-Lactoglobulin: Implication for Non-Hierarchical Protein Folding. *J Mol Biol* **1995**, *245* (2), 180–194. https://doi.org/10.1006/jmbi.1994.0015.

(19) Pan, C.-P.; Muiño, P. L.; Barkley, M. D.; Callis, P. R. Correlation of Tryptophan Fluorescence Spectral Shifts and Lifetimes Arising Directly from Heterogeneous Environment. *J Phys Chem B* **2011**, *115* (12), 3245–3253. https://doi.org/10.1021/jp111925w.

(20) Lee, J. C.; Gray, H. B.; Winkler, J. R. Copper(II) Binding to α-Synuclein, the Parkinson's Protein. *J. Am. Chem. Soc.* **2008**, *130* (22), 6898–6899. https://doi.org/10.1021/ja711415b.

(21) Lee, J. C.; Langen, R.; Hummel, P. A.; Gray, H. B.; Winkler, J. R. α-Synuclein Structures from Fluorescence Energy-Transfer Kinetics: Implications for the Role of the Protein in Parkinson's Disease. *Proc Natl Acad Sci U.S.A.* **2004**, *101* (47), 16466–16471. https://doi.org/10.1073/pnas.0407307101.

(22) Schubert, K.; Karousis, E. D.; Jomaa, A.; Scaiola, A.; Echeverria, B.; Gurzeler, L.-A.; Leibundgut, M.; Thiel, V.; Mühlemann, O.; Ban, N. SARS-CoV-2 Nsp1 Binds the Ribosomal mRNA Channel to Inhibit Translation. *Nat Struct Mol Biol* **2020**, *27* (10), 959–966. https://doi.org/10.1038/s41594-020-0511-8.

(23) Winkler, J. R.; Gray, H. B. Long-Range Electron Tunneling. *J Am Chem Soc* **2014**, *136* (8), 2930–2939. https://doi.org/10.1021/ja500215j.

(24) Thoms, M.; Buschauer, R.; Ameismeier, M.; Koepke, L.; Denk, T.; Hirschenberger, M.; Kratzat, H.; Hayn, M.; Mackens-Kiani, T.; Cheng, J.; Straub, J. H.; Stürzel, C. M.; Fröhlich, T.; Berninghausen, O.; Becker, T.; Kirchhoff, F.; Sparrer, K. M. J.; Beckmann, R. Structural Basis for Translational Shutdown and Immune Evasion by the Nsp1 Protein of SARS-CoV-2. *Science* **2020**, *369* (6508), 1249–1255. https://doi.org/10.1126/science.abc8665.

(25) Yuan, S.; Peng, L.; Park, J. J.; Hu, Y.; Devarkar, S. C.; Dong, M. B.; Shen, Q.; Wu, S.; Chen, S.; Lomakin, I. B.; Xiong, Y. Nonstructural Protein 1 of SARS-CoV-2 Is a Potent Pathogenicity Factor Redirecting Host Protein Synthesis Machinery toward Viral RNA. *Mol Cell* **2020**, *80* (6), 1055-1066.e6. https://doi.org/10.1016/j.molcel.2020.10.034.

(26) Chang, I.-J.; Lee, J. C.; Winkler, J. R.; Gray, H. B. The Protein-Folding Speed Limit: Intrachain Diffusion Times Set by Electron-Transfer Rates in Denatured Ru(NH3)5(His-33)-Zn-Cytochrome c. *Proc Natl Acad Sci U.S.A.* **2003**, *100* (7), 3838–3840. https://doi.org/10.1073/pnas.0637283100.

(27) Hagen, S. J.; Hofrichter, J.; Eaton, W. A. Rate of Intrachain Diffusion of Unfolded Cytochrome *c*. *J Phys Chem B* **1997**, *101* (13), 2352–2365. https://doi.org/10.1021/jp9622997.

(28) Szabo, A.; Schulten, K.; Schulten, Z. First Passage Time Approach to Diffusion Controlled Reactions. *J Chem Phys* **1980**, *72* (8), 4350–4357. https://doi.org/10.1063/1.439715.

(29) Thirumalai, D. Time Scales for the Formation of the Most Probable Tertiary Contacts in Proteins with Applications to Cytochrome *c*. *J Phys Chem B* **1999**, *103* (4), 608–610. https://doi.org/10.1021/jp982362n.

(30) Garribba, E.; Micera, G. The Determination of the Geometry of Cu(II) Complexes: An EPR Spectroscopy Experiment. *J Chem Educ* **2006**, *83* (8), 1229. https://doi.org/10.1021/ed083p1229.

(31) Peisach, J.; Blumberg, W. E. Structural Implications Derived from the Analysis of Electron Paramagnetic Resonance Spectra of Natural and Artificial Copper Proteins. *Arch Biochem Biophys* **1974**, *165* (2), 691–708. https://doi.org/10.1016/0003-9861(74)90298-7.

(32) Van Camp, H. L.; Wei, Y. H.; Scholes, C. P.; King, T. E. Electron Nuclear Double Resonance of Cytochrome Oxidase: Nitrogen and Proton Endor from the 'Copper' EPR Signal. *BBA Proteins and Proteomics* **1978**, *537* (2), 238–246. https://doi.org/10.1016/0005-2795(78)90507-X.

(33) Scholl, H. J.; Huettermann, J. ESR and ENDOR of Copper(II) Complexes with Nitrogen Donors: Probing Parameters for Prosthetic Group Modeling of Superoxide Dismutase. *J Phys Chem* **1992**, *96* (24), 9684–9691. https://doi.org/10.1021/j100203a023.

(34) Ritterskamp, N.; Sharples, K.; Richards, E.; Folli, A.; Chiesa, M.; Platts, J. A.; Murphy, D. M. Understanding the Coordination Modes of [$Cu(Acac)_2(Imidazole)_{n=1,2}$] Adducts by EPR, ENDOR, HYSCORE, and DFT Analysis. *Inorg Chem* **2017**, *56* (19), 11862–11875. https://doi.org/10.1021/acs.inorgchem.7b01874.

(35) Van Doorslaer, S.; Vinck, E. The Strength of EPR and ENDOR Techniques in Revealing Structure–Function Relationships in Metalloproteins. *Phys Chem Chem Phys* **2007**, *9* (33), 4620. https://doi.org/10.1039/b701568b.

(36) De Andrade, J. C. D.; Silva, L. A. T.; Lima-Junior, C. G.; Chojnacki, J.; Vasconcellos, M. L. A. D. A.; Da Silva, R. B.; Alves Júnior, S.; Da Silva, F. F. Copper and Copper-Manganese 1D Coordination Polymers: Synthesis Optimization, Crystal Structure and Preliminary Studies as Catalysts for Baylis–Hillman Reactions. *Inorganica Chimica Acta* **2021**, *514*, 119985. https://doi.org/10.1016/j.ica.2020.119985.

(37) Kaler, S.; Munim, S.; Chen, M.; Niecestro, R.; Yam, L. eP195: Safety and Efficacy of Copper Histidinate (CUTX-101) Treatment for Menkes Disease Caused by Severe Loss-of-Function Variants in ATP7A. *Genet Med* **2022**, *24* (3), S121. https://doi.org/10.1016/j.gim.2022.01.231.

Chapter 4

COBALT BINDING TO NSP1 STUDIES

[THIS CHAPTER IS TEMPORARILY EMBARGOED.]

Chapter 5

FULL LENGTH NSP1 STUDIES

[THIS CHAPTER IS TEMPORARILY EMBARGOED.]

I can do all things through Christ who strengthens me.

Philippians 4:13